

Copyright

by

Michael Ryan McCann

2019

**The Thesis Committee for Michael Ryan McCann
Certifies that this is the approved version of the following Thesis:**

Low-Frequency Attenuation Measurements of Fluids

**APPROVED BY
SUPERVISING COMMITTEE:**

Kyle T. Spikes, Supervisor

Nicola Tisato, Co-Supervisor

Mrinal K. Sen

Low-Frequency Attenuation Measurements of Fluids

by

Michael Ryan McCann

Thesis

Presented to the Faculty of the Graduate School of

The University of Texas at Austin

in Partial Fulfillment

of the Requirements

for the Degree of

Master of Science in Geological Sciences

The University of Texas at Austin

May 2019

Dedication

I dedicate this thesis to my parents. I would not be where I am today without their support and everything they have provided. I also dedicate this thesis to Anne whose encouragement has kept me motivated throughout my time as a graduate student.

Acknowledgements

I would like to thank Nicola Tisato for his help with designing and setting up the machine used for this work. I also would like to thank my advisor Kyle Spikes for his support. I also want to extend my gratitude to Seismos and the rest of the EDGER Forum for their generous support of our research.

Abstract

Low-Frequency Attenuation Measurements of Fluids

Michael Ryan McCann, M.S.GEO.SCI

The University of Texas at Austin, 2019

Supervisors: Kyle Spikes and Nicola Tisato

Pore fluids significantly affect the elastic responses of rocks. Rock-physics models can be used to predict how pore fluids affect the elastic responses of fully or partially saturated rocks. Thus, to identify fluids in the subsurface, knowing the anelastic properties of such fluids, such as attenuation, is useful. In addition, new technologies to assess and monitor hydrocarbon exploration rely on the precise determination of the anelastic properties of hydraulic fracturing fluids. Moreover, the anelastic properties of fluids depend on the frequency of the wave propagating through the fluid. Methodologies to measure high-frequency anelastic properties of fluids have been widely reported. What have not been established are methodologies to measure the low-frequency anelastic properties and attenuation of fluids in a laboratory setting, aside from shear viscosity. Using the low-frequency properties and attenuation, rather than the already known high-frequency properties of pore fluids, will provide more accurate estimates for rock physics models and seismic data. To address this situation, a laboratory machine has been designed, built, and calibrated to measure the low-frequency attenuation and bulk

modulus of fluids at frequencies from 0.1 to 10 Hz. Deionized water and aqueous guar gum solutions have been tested. Results for measurements of attenuation and bulk modulus of water agree with the literature. Measurements of guar gum solutions show that attenuation is greater than 0.01 with higher concentration samples having higher attenuation. This might be explained by energy being lost during the breakup of weak and strong bonds in the guar gum polymer chains. A higher concentration provides more bonds to break up which leads to more energy being lost which increases attenuation. The present study will help improve seismic methods and rock physics models by incorporating low-frequency attenuation values of fluids.

Table of Contents

List of Tables	xi
List of Figures	xii
Chapter 1: Introduction	1
1.1 Introduction To Attenuation	1
1.2 Motivation.....	4
1.3 Objective.....	6
1.4 Outline Of Thesis.....	6
Chapter 2: Background of Attenuation and Bulk Modulus of Materials.....	8
2.1 Attenuation and How It Is Defined.....	8
2.1.1 Types of Attenuation.....	8
2.1.2 Definition of Attenuation.....	8
2.1.3 Values of Attenuation	13
2.2 Attenuation Factors.....	16
2.2.1 Frequency.....	16
2.2.2 Strain Amplitude.....	17
2.2.3 Fluid Saturation and Type.....	18
2.2.4 Temperature	19
2.3 Attenuation Mechanisms	20
2.3.1 Rocks.....	20
2.3.2 Fluids.....	22
2.4 Attenuation Measurement Methods.....	24

2.4.1 Ultrasonic	24
2.4.2 Resonance	24
2.4.3 Forced Oscillation	25
2.5 Bulk Modulus	25
2.5.1 Bulk Modulus Measurement Methods	26
Chapter 3: Methodology	28
3.1 Overview of Experiment.....	28
3.2 Fluid Flow Considerations.....	29
3.3 Description of Fluids Tested.....	35
3.4 Description of the Machine.....	39
3.5 Description of Electronic Parts	46
3.5.1 Piezoelectric Motor	47
3.5.2 Pressure Sensor	48
3.5.3 Shortening Sensor	48
3.5.4 A/D and D/A converter	48
3.5.5 PCB Boards.....	49
3.6 Description of Air Evacuation Parts and Schematic.....	49
3.7 Calibration of Sensors.....	52
3.8 Experimental Setup Procedure.....	53
3.9 Description of Codes	56
3.10 Tests On Solids	59
3.11 Limitations of the Machine.....	61
3.12 Experimental Operation Procedure.....	63

3.13 Typical Strain Values.....	64
3.14 Effect of Transient Fluid Pressure	65
Chapter 4: Results and Discussion.....	71
4.1 Water Results.....	71
4.2 Water Discussion	73
4.3 Guar Gum Results.....	74
4.4 Guar Gum Discussion.....	76
Chapter 5: Conclusions and Future Work.....	78
5.1 Conclusions.....	78
5.2 Future Work.....	79
Appendix A: Part Drawings	80
References.....	95

List of Tables

Table 2.1:	Reference values of Q for several nonporous materials. Data is compiled from Johnston (1981).....	14
Table 2.2:	Reference values of Q for several rocks. Data is compiled from Knopoff (1964).....	15
Table 3.1:	Parameters used in the numerical model.	69
Table 4.1:	Measured values of bulk modulus of water and reported values of bulk modulus of water from the National Institute of Standard's and Technology's (NIST) database of thermophysical properties of fluid systems at various pressures. Results from our experiments agree with those reported by NIST.....	72

List of Figures

- Figure 1.1: Stress-strain relations for elastic and inelastic materials. The amount of energy dissipated as heat for the inelastic material is proportional to the area between the loading and unloading paths.2
- Figure 1.2: Experimental setup used to infer hydraulic fracture conductivity from Dunham et al. (2017). A source is located at the surface which generates tube waves in the borehole. The waves travel down and reflect off a set of fractures and a packer and return to the surface where they are recorded using a hydrophone. Several sets of wave multiples are recorded. A model that includes the attenuation of the fracking fluid is used to fit to the recorded data.5
- Figure 2.1: The stress applied to a non-elastic material and resulting strain as a function of time. The strain lags behind the stress because the material is not perfectly elastic. ϕ is the phase delay between the stress and the strain curves and is shown in the figure. $1/Q$ is calculated from ϕ12
- Figure 2.2: Q as a function of porosity for igneous and metamorphic rocks (triangles), limestones (squares), and sandstones (circles). Q is generally inversely proportional to porosity. The data in this plot do not distinguish between frequency nor degrees of saturation. Data for this plot comes from Bradley and Fort (1966) and was reproduced by Johnston et al. (1979).16

Figure 3.1: Demonstration of how the material at the top of a block moves further than the material at the bottom when the block is compressed. This shows how fluid flow in the pressure vessel is not constant with depth and the Reynolds number will also vary with depth.....31

Figure 3.2: Reynolds number in the vessel at various depths for an experiment with a vessel length of 10 cm, fluid viscosity of 0.001 Pa*s, fluid density of 1000 kg/m³, fluid compression of 30 micrometers, and frequency of compression of 20 Hz. The compression and frequency are on the high side of the parameters used during testing. Therefore, actual Reynolds numbers would be lower. This figure shows the Reynolds number only in the pressure vessel. The pipe has a smaller radius so the Reynolds number would be smaller. Reynolds number changes with depth because the fluid at the bottom of the vessel does not move as far as the fluid on top. Flows with Reynolds numbers of less than 2300 for a cylindrical pipe are laminar.....32

Figure 3.3: The development of a fluid flow moving from left to right. The velocity profile of the flow is shown at several points throughout the flow. The velocity profile is constant throughout the flow and eventually makes a parabolic shape when it is fully developed. The figure also shows the boundary layer and how it increases as the flow develops. The velocity profile is constant while in the boundary layer. Figure from Yunus and Cimballa (2006).34

Figure 3.4: Chemical structure of guar gum. Galactose units are linked to a principle backbone chain of mannose units. Figure from Mudgil et al. (2014)......36

Figure 3.5: Viscosity of 10 ppt guar gum solution as a function of the amount of time it had been mixed. The viscosity rapidly increases during the first thirty minutes and then starts to reach a steady value. Samples of guar gum were mixed for at least an hour before they were tested to make sure that each sample made with the same concentration had the same viscosity.38

Figure 3.6: Schematic and section view of the machine used to measure the low-frequency attenuation of fluids. The major components are labeled. The fluid sits inside the pressure vessel (#3) and is brought up to the desired pressure using a fluid pump. A voltage will be applied to the piezoelectric motor (#1) which will cause the motor to expand which will then move the piston (#4) downward and compress the fluid. A pressure sensor (#5) will measure the pressure of the fluid during the experiment and a displacement sensor (#2) will be attached to the piston to measure the shortening of the fluid sample.39

Figure 3.7: Schematic of the machine and a bill of materials showing the name and quantity of each part.....40

Figure 3.8: Section view of the bottom half of the machine. The pipe (#1) is used to bring fluid into and out of the pressure vessel. The pipe is welded into the vessel cover (#4). The pressure sensor (#2) screws into the vessel cover. The pressure vessel (#3) is screwed into the vessel cap (#5) to secure the vessel cover. The vessel cap sits on the vessel base (#6) with the pipe sticking out of the slot of vessel base.42

Figure 3.9: Detail view of machine showing displacement sensor and lip pieces.44

Figure 3.10: Schematic of the electronics used in the experiment. A power supplier is connected to the amplifiers (L and P for load cell and pressure sensor) which power the load cell and pressure sensor. The signal generated from the load cell and pressure sensor is amplified and sent to the A/D converter (NI USB-6281). A computer is connected to the A/D converter to record the measurements. An analog output is sent to an amplifier which is then sent to the piezoelectric motor to make the motor expand and contract for the experiment.47

Figure 3.11: Schematic of the setup used to evacuate the pressure vessel of air and to fill it with the fluid to be tested. First the valve connecting to the vacuum is opened, and the air is removed using the vacuum. The valve is then closed and the valve connecting to the fluid container is opened. The fluid pump is then used to pump the fluid from the container into the pressure vessel. Once the pressure vessel is filled, the valve to the fluid container is closed.....50

Figure 3.12: Phase delay between the amplifiers used to power the sensors in the experiment. Results show a phase delay of 0 so any phase delay measured during the experiment can confidently be attributed to material that is being tested.....53

Figure 3.13 Picture of the machine and all the components used during the experiment. All parts are labelled. The fluid pump is connected to a three-way valve that is connected to the bottom of the machine. A vacuum pump is connected to the same valve. The vacuum pump is used to draw out any air in the system before the fluid pump is used to fill the and pressurize the pressure vessel in the machine. The electronics board contains the power supplier, two amplifiers used with the sensors, and the multifunction board. Another amplifier powers the piezoelectric motor in the machine. On the right side is the computer that is used to run the experiment and save the data that is recorded.56

Figure 3.14: Flow chart showing how the MATLAB script that is used to run the experiment works. The script first reads and sets the test parameters. The highest frequency is first selected. The sinusoidal signal is generated and the pressure and shortening signals are recorded, stacked, and smoothed. Attenuation is then calculated from these signals. The next lowest frequency is then tested. Once the lowest frequency is tested the highest frequency is tested next until the number of desired repetitions is achieved.58

Figure 3.15: Experimental setup of tests done on solid samples. This image shows a test of an aluminum rod. The aluminum rod sits on the bottom of the frame and a stainless-steel bar sits on top of it. The stainless-steel bar has the displacement sensor attached to it. Above the stainless-steel bar is the piezoelectric motor. Above the motor is a compression load cell that is used to measure the strain of the sample.60

Figure 3.16: Measured I/Q values of a rod of acrylic and a rod of aluminum. Results for aluminum show very low attenuation values, and results for acrylic show a maximum attenuation of $Q^{-1} \approx 0.07$61

Figure 3.17: Results of a test on water from 0.1 to 20 Hz. Results show that the machine is unreliable at frequencies above 5 Hz.....62

Figure 3.18: Volumetric strain of fluid during the experiment with typical values of fluid compression and fluid volume. The volumetric strain is typically on the order of 10^{-4}65

Figure 3.19: Schematic of the vessel and pipe setup used in the numerical simulation. The radius and length of the vessel and pipe shown in the figure are proportional to their actual sizes. The permeability of each is also given.68

Figure 3.20: Results from the numerical simulation. The top plot shows the initial pressure wave that was forced on the end of the vessel. The bottom plot shows the pressure difference between the end of the vessel and the end of the pipe. The pressure diffuses throughout the system to 10^5 Pa in less than 0.002 seconds which is much smaller than any period that the machine operates at. Attenuation caused by wave induced fluid flow is therefore negligible.70

Figure 4.1: Results of attenuation measurements of water at 10, 20, 30, and 40 MPa. Results below 5 Hz generally show the attenuation coefficient is less than 0.01. The machine starts to produce unreliable results at 40 MPa.....71

Figure 4.2: Results of measured bulk modulus of water with error bars that represent one standard deviation as plotted against pressure. Also shown are the results from the NIST’s database for water. Measured results slightly underpredict the true value but are within the bounds of the error bars.73

Figure 4.3: Results of $1/Q$ measurements of aqueous guar gum solutions. Results were obtained at 10 MPa for concentrations of 10, 20, and 40 ppt. Attenuation is higher than water and increases with concentration.....75

Figure 4.4: Bulk modulus of guar gum as a function of pressure and concentration. Error bars represent one standard deviation. The bulk modulus of water is also shown. Bulk modulus of guar gum increases with pressure and concentration.....76

Chapter 1: Introduction

1.1 INTRODUCTION TO ATTENUATION

As seismic waves propagate through a material, they lose energy and amplitude as a function of distance. This phenomenon is known as seismic attenuation ($1/Q$). The quality factor of a material, denoted as Q , and the attenuation coefficient, α , are quantities used to describe how rapidly the energy of a propagating seismic wave is dissipated in a material. Waves propagating through a material with a high Q value will lose energy more slowly than they would through a material with a lower Q value.

During seismic wave propagation, the molecules of the medium are distorted. A perfectly elastic material is said to be a material that when deformed the distortion of bonds is stored as elastic energy. All the elastic energy can then be used to restore the bonds of the material completely when the stress is removed. In other words, an elastic response is said to be a reversible process. An anelastic response is irreversible, and part of the energy stored in the deformed bonds is lost as heat (Cooper (2002); Orban (2011)). The loss of energy also causes a delay in the anelastic response (Lakes, 2009).

A stress-strain diagram of the application and removal of a load on a material can illustrate one of the differences between elastic and anelastic materials (Figure 1.1). In the case of the elastic material, the stress-strain curve is a line because an elastic material deforms the moment a stress is applied to it and returns to its original state when the stress is removed. The loading and unloading curves follow the same path. In the case of an anelastic material the loading and unloading curves separate. The amount of energy lost per stress-strain cycle is proportional to the area between the loading and unloading curves (Lakes (2009); Orban (2011)).

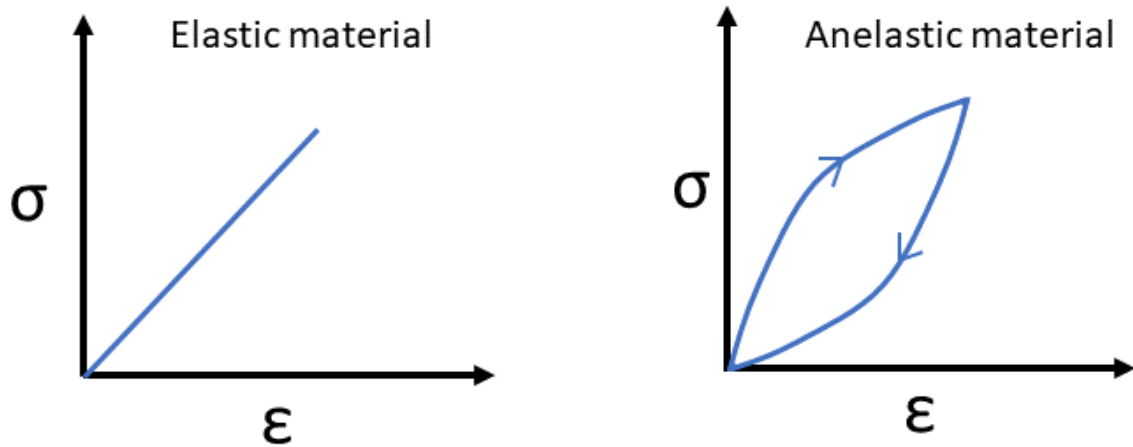


Figure 1.1: Stress-strain relations for elastic and inelastic materials. The amount of energy dissipated as heat for the inelastic material is proportional to the area between the loading and unloading paths.

Energy is lost in each cycle of the seismic wave in the form of heat if the material is not perfectly elastic. No perfectly elastic material exists. Seismic waves attenuate at different rates in different materials, and the quality factor of a material describes how quickly energy is lost during wave propagation. The quality factor of rocks depends on many factors including, but not limited to, microstructure, pore fluids, confining pressure, seismic wave frequency, and fluid type. A more formal definition of attenuation and discussion of attenuation factors and mechanisms is presented in Chapter 2.

The attenuation value of a viscoelastic material is related to its modulus. More specifically, its related to the change in the value of the modulus as a function of frequency or modulus dispersion. The Kramers-Kronig relation states that if the dispersion of a material is completely characterized for all frequencies then attenuation is known for all frequencies and vice versa (Mavko et al., 2009). In other words, a large attenuation value is always associated with a large modulus dispersion. This relation can

be used to infer the behavior of either the attenuation or modulus when one of them is known. Attenuation is therefore a frequency dependent property and the high-frequency attenuation values are not necessarily similar to the low-frequency attenuation values in a material.

Attempts have been made to relate the viscosity of liquids to the attenuation of liquids. For instance, Stokes (1901) was the first to suggest and work out how the attenuation of surface waves in a liquid could be used to determine the liquids' shear viscosity. Behroozi et al. (2010) developed an experimental method to test this relation which was successful.

The Navier-Stokes equation is an equation that describes the motion of a viscous fluid. For a compressible Newtonian liquid, the equation can be written as

$$\rho \left[\frac{\partial v}{\partial t} + (v \nabla) v \right] = -\nabla P + \eta \Delta v + \left(\eta^b + \frac{4}{3} \eta \right) \nabla (\nabla \cdot v) \quad (1.1)$$

where ρ is density, t is time, v is velocity, P is pressure, η is shear viscosity, and η^b is bulk viscosity (Landau and Lifshitz, 1959). The type of viscosity that was used by Stokes and Behroozi et al. (2010) was shear viscosity. The second type of viscosity, bulk viscosity, is a relatively obscure quantity and is only used when it is important to consider the compressibility of the fluid. Otherwise $\nabla \cdot v = 0$ and the last term of the right-hand side is zero and the equation reduces to a more familiar form which is the non-compressible fluid form of the Navier-Stokes equation. Since shear viscosity is related to attenuation, it is not unreasonable to assume that bulk viscosity is also related to attenuation. Dukhin and Goetz (2009) discuss techniques of measuring the bulk viscosity of fluids and also show how ultrasonic bulk viscosity can be calculated from ultrasonic

attenuation. Low-frequency bulk viscosity measurements could therefore be used to estimate low-frequency attenuation values. As will be discussed in detail later, the measurements that were taken in this work are in fact bulk viscosity measurements and from those we can get the attenuation of the fluid.

1.2 MOTIVATION

Knowledge of how fluids attenuate seismic waves has useful applications in exploration geophysics. Attenuation, like other viscoelastic properties, is dependent on the frequency of the seismic wave propagating through the material (Mason et al., 1970; Barton, 2007). For seismic exploration, seismic waves that have a frequency below 100 Hz are used. Seismic experiments measure the low-frequency (<100 Hz) response of rocks because high frequencies attenuate rapidly in the subsurface.

One example of a seismic experiment is borehole monitoring which is accomplished using seismic acquisition. For instance, Dunham et al. (2017) monitored the conductivity of fractures prior to hydrocarbon production with an active seismic source. Figure 1.2 shows a setup of their active source experiment. The source is located at the well head, and a pulse travels down the borehole and back up and the multiples of the tube wave are recorded. Their model, which is used to predict the conductivity of hydraulic fractures, requires the intrinsic attenuation of the fracking fluid used during production. Because their source is low-frequency, it would be ideal to use the low-frequency attenuation values of the fracking fluid. This would result in more accurate results of fracture conductivity compared to using the high-frequency attenuation values of the fracking fluid. Likewise, low-frequency attenuation values of fluids would be more useful in all rock physics models where seismic data is used because the values between the two could be drastically different.

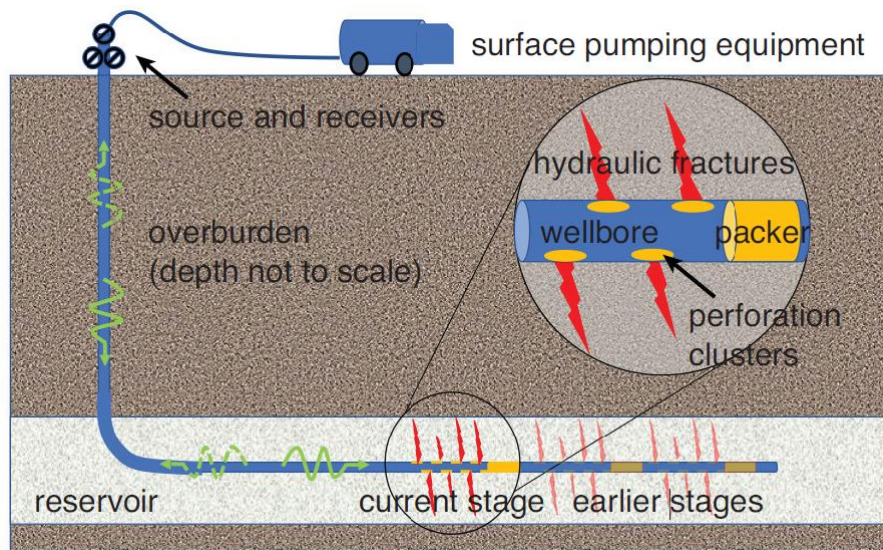


Figure 1.2: Experimental setup used to infer hydraulic fracture conductivity from Dunham et al. (2017). A source is located at the surface which generates tube waves in the borehole. The waves travel down and reflect off a set of fractures and a packer and return to the surface where they are recorded using a hydrophone. Several sets of wave multiples are recorded. A model that includes the attenuation of the fracking fluid is used to fit to the recorded data.

Another application where the low-frequency attenuation values of fluids would be useful is during the modeling of seismic waves in gas-charged magma. This is critical for the understanding of seismic resonance effects in conduits, dykes, and cracks (Collier et al., 2006) which leads to better predictions of the behavior of volcanic systems. Likewise, Tisato et al. (2015) show how bubbles in pore fluids attenuate seismic waves in rocks. This has significant implications in monitoring areas of bubbly fluid systems such as carbon dioxide sequestration reservoirs.

Exploration geophysics relies heavily on seismic methods to image and obtain information such as the structure and composition of the subsurface. Amplitude and frequency attributes from seismic data are used primarily for this (Subramanian et al., 2014). Attenuation can be seen in seismic data and has the potential to be used as an

attribute to infer rock and pore-fluid properties (Chapman et al., 2006). Seismic data is inherently low-frequency (<100 Hz), so the low-frequency attenuation of pore fluids alone would be needed to use attenuation as a seismic attribute.

1.3 OBJECTIVE

The goal of this work is to design and build an apparatus that measures the low-frequency attenuation of fluids, and then measure the low-frequency attenuation of fluids at pressures relevant reservoir conditions. Methodologies to measure the high-frequency attenuation of fluids exist and are widely available. Measurements down to 100 Hz (Thorp, 1965) have been conducted in sea water but this was done in the ocean with seismic sources on boats with receivers spaced miles apart. To the best of our knowledge, no laboratory methodology has been established to measure the low-frequency (<100 Hz) attenuation of fluids. The methodology from this work can then be used in outstanding issues in rock physics where the low-frequency attenuation of fluids is more desirable to use than the already known or easily measurable high-frequency attenuation values.

1.4 OUTLINE OF THESIS

Chapter 1 gives a brief introduction to attenuation along with motivation and the objective for the work in this thesis. Chapter 2 gives background information for the thesis, which includes the definition of attenuation, factors that affect attenuation, and how attenuation is measured in laboratory experiments. A discussion of the bulk modulus is also included. Chapter 3 discusses the methodology of the experiment that was conducted to measure the attenuation of fluids at low frequencies. An in-depth description of parts that were used and the setup including assembly and operation procedures is given. Chapter 4 shows the measured results of the attenuation and bulk

modulus of the experiment for the fluids that were tested. Chapter 5 includes conclusions drawn from the experiment and gives recommendations for future work and improvements for the experiment. Appendix A gives detailed drawings for each custom-made part that was used in the machine of the experiment and a schematic of the printed circuit boards that were used.

Chapter 2: Background of Attenuation and Bulk Modulus of Materials

2.1 ATTENUATION AND HOW IT IS DEFINED

2.1.1 Types of Attenuation

Attenuation can be categorized into two broad types. The first type is called extrinsic attenuation. Extrinsic attenuation is caused by geometric spreading of a seismic wave (Klimentos, 1991). Seismic waves are generated by a burst of energy at a single point when there is a source such as an explosion or hammer strike. The wavefield then spreads out in a spherical shape as the wave propagates. As the seismic wave move outward from the source, the wavefield expands, and the amplitude of the wave decreases because the energy of the wavefield is distributed over a larger surface area. This type of attenuation is well known and can be corrected for in seismic processing with a geometric spreading factor (Kearey et al., 2013).

The second type of attenuation is called intrinsic attenuation and is often referred to just as attenuation (Subramaniyan et al., 2014). Intrinsic attenuation is controlled by the characteristics of the material and the pore fluids of the material through which the seismic wave is propagating. The exact mechanisms by which seismic waves lose energy through intrinsic attenuation are not yet fully understood. An in-depth discussion about the mechanisms associated with attenuation are given later in this chapter.

2.1.2 Definition of Attenuation

Attenuation is the process by which seismic waves lose energy as they propagate with distance. It is important to have a precise definition of attenuation to avoid confusion between different measures of attenuation. The most commonly used measures

of attenuation are the attenuation coefficient α , the quality factor Q , and the logarithmic decrement δ . These quantities are related by

$$\frac{1}{Q} = \frac{\alpha v}{\pi f} = \frac{\delta}{\pi} \quad (2.1)$$

where v is velocity of the seismic wave and f is frequency (Toksoz and Johnston, 1981). Both velocity and attenuation are associated with particular vibrational modes of wave propagation (e.g., extensional, torsional, and shear) that, in general, are not equal amongst each other (Toksoz and Johnston, 1981). Born (1941) expressed the attenuation coefficient as a ratio of the amplitude of a seismic wave after it has propagated through a material by some distance, x , to the initial amplitude of the seismic wave as in equation 2.2

$$A_x = A_0 e^{-\alpha x} \quad (2.2)$$

where A_x is the amplitude of the seismic wave after some distance x , A_0 is the initial amplitude of the seismic wave, α is the attenuation coefficient of the material. This equation states that for each unit of distance traveled, the seismic waves experience the same percent reduction in amplitude. The attenuation coefficient, therefore, has units of inverse length. In general, for any distances x_1 and x_2 ($x_1 < x_2$), the attenuation coefficient can be expressed as

$$\alpha = \frac{1}{x_2 - x_1} \ln \frac{A(x_1)}{A(x_2)}. \quad (2.3)$$

The definition of the logarithmic decrement δ is related to α by

$$\delta = \ln \frac{A_1}{A_2} = \alpha \lambda = \frac{\alpha v}{f} \quad (2.4)$$

where A_1 and A_2 are consecutive cycles of damped free oscillating system, v is the velocity, and f is frequency. δ is also equal to π/Q .

The most commonly used measures of attenuation are the quality factor Q and its inverse Q^{-1} which are dimensionless. Energy is lost more quickly in materials with lower Q values than those with higher Q values. Q is an intrinsic property of all materials and has two commonly used definitions for small-dissipation ($Q > 10$) materials. Knopoff (1964) used a definition of Q that is related to a familiar electrical circuit theory for energy loss given by

$$\frac{2\pi}{Q} = \frac{\Delta E}{E} \quad (2.5)$$

where ΔE is the amount of energy dissipated per cycle of a harmonic excitation in a certain volume, and E is the peak elastic energy in the system in the same volume.

O'Connell and Budiansky (1978) define attenuation as the ratio of the real to the imaginary parts of the complex modulus of a material. When a sinusoidally varying stress is applied to a linear-time invariant material, the strain response is also sinusoidal. All anelastic materials exhibit a delay between the applied stress and the resulting strain. The elastic moduli of anelastic materials are thus described by a complex number to account for the phase between the stress and the strain. The degree of non-elasticity is determined from the imaginary part of the modulus. Materials with smaller imaginary parts of the complex modulus are less anelastic and have a smaller delay between the stress and

strain. Materials with larger imaginary parts of the complex modulus are more anelastic and have a larger phase delay between the stress and strain. From O'Connell and Budiansky's (1978) definition of attenuation, attenuation can be calculated from the phase delay between the applied stress on a material and the resulting strain of the material. Equations 2.6-2.8 give the attenuation of a material and the real and imaginary parts of the modulus of a material where M is the modulus being measured, σ is the applied stress, ε is the resulting strain, and ϕ is the phase delay between the stress and the strain

$$\frac{1}{Q} = \tan \phi \quad (2.6)$$

$$Re(M) = \frac{\sigma}{\varepsilon} \cos \phi \quad (2.7)$$

$$Im(M) = \frac{\sigma}{\varepsilon} \sin \phi \quad (2.8)$$

Figure 2.1 shows the hypothetical curves of an applied stress and resulting strain of a non-elastic material and the phase delay between the two.

Stress and strain of a non-elastic material

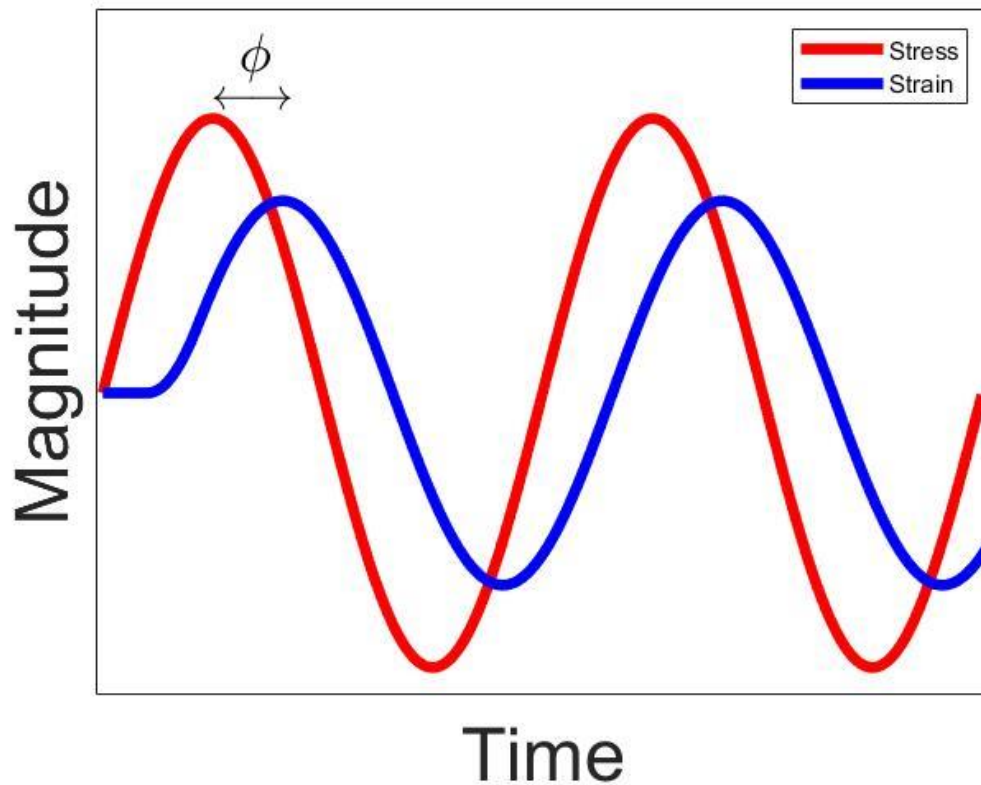


Figure 2.1: The stress applied to a non-elastic material and resulting strain as a function of time. The strain lags behind the stress because the material is not perfectly elastic. ϕ is the phase delay between the stress and the strain curves and is shown in the figure. $1/Q$ is calculated from ϕ .

Here, Q is related to the attenuation coefficient for small-dissipation materials by

$$\frac{1}{Q} = \frac{\alpha v}{\pi f}. \quad (2.9)$$

For large dissipation materials ($Q < 10$) a second-order term must be included to relate Q to the attenuation coefficient. Hamilton (1972) showed that for large-dissipation materials

$$\frac{1}{Q} = \frac{\alpha v}{\pi f - \frac{\alpha^2 v^2}{4\pi f}}. \quad (2.10)$$

Q can also be defined in terms of a resonance-peak bandwidth

$$Q = \frac{f_r}{\Delta f}, \quad (2.11)$$

where Δf is the frequency width of 3 dB in amplitude about a resonance peak f_r on a power-frequency plot. This definition of Q is valid for small dissipative materials (Toksoz and Johnston, 1981). The methods used to measure Q mentioned in this section are discussed further later in this chapter.

2.1.3 Values of Attenuation

Q values for various non-porous materials and some fluids have been measured at various frequency ranges and modes. Table 2.1 shows values Q for several nonporous materials from Johnston (1981).

Material	Q	Mode	Frequency range
Aluminum	200,000	Longitudinal resonance	1 to 200 kHz
Brass	655	Flexural resonance	-
Annealed Copper	5,930	P-wave pulse	25 to 75 kHz
Lead	36	Longitudinal resonance	1.6 to 15 kHz
Magnesium	965	P-wave pulse	7 to 76 MHz
Nickle	980	Flexural resonance	12 to 33 Hz
Steel	1,850	Flexural resonance	2 to 8 Hz
Glass	490	Flexural resonance	12 to 27 Hz
Lucite	23	Longitudinal resonance	1 kHz
Dry Air	562	Resonance	100 Hz
Fresh Water	210,000	Resonance	100 kHz
Salt Water	63,000	Resonance	150 kHz

Table 2.1: Reference values of Q for several nonporous materials. Data is compiled from Johnston (1981).

The attenuation value of a rock depends on many factors. These factors include, but are not limited to, the amount of microcracking, pressure, pore fluids, lamination and jointing at larger scales (Tisato and Madonna, 2012; Tisato and Quintal, 2013; Tisato et al., 2015). The mechanism by which energy attenuates in rocks depends on the structure of the rock, the frequency of the wavelet, and the composition and degree of saturation of pore fluids. Table 2.2 shows values of Q for several rock samples from Knopoff (1964).

Material	Q	Mode	Frequency Range
Diabase Glass	3,500	-	50 to 90 kHz
Silica	1,250	-	1 to 10 Hz
Quincy Granite	100	Longitudinal resonance	140 to 1,600 Hz
Quincy Granite	150 – 200	Torsional	140 to 1,600 Hz
Amherst Sandstone	52	Longitudinal resonance	930 to 12,800 Hz
Hunton Limestone	65	Longitudinal resonance	2.8 to 10.6 kHz
Sylvan Shale	73	Longitudinal resonance	3.4 to 12.8 kHz
Sandstone	21	Flexural excitation	50 to 120 Hz
Oolitic limestone	45	Flexural excitation	50 to 120 Hz
Shelly Limestone	63	Flexural excitation	50 to 120 Hz
Granite	57	Flexural excitation	50 to 120 Hz
Dolorite	90	Flexural excitation	50 to 120 Hz
Diorite	125	Flexural excitation	50 to 120 Hz
Westerly Granite	79	Rayleigh wave pulses	50 to 400 kHz
Solenhofen Limestone	110	Compressional pulses	3 to 15 MHz
Solenhofen Limestone	190	Shear pulses	3 to 9 MHz

Table 2.2: Reference values of Q for several rocks. Data is compiled from Knopoff (1964).

A graphical compilation of Q values as a function of porosity for various types of rocks from data provided by Bradley and Fort (1966) and reproduced by Johnston et al. (1979) is given in figure 2.2. This plot does not show the distinction between different frequencies and degrees of saturation amongst the samples. Rock types are shown by different shapes and are circled together. The plot shows generally that the quality factor is inversely proportional to porosity, and sedimentary rocks have lower Q values than igneous and metamorphic rocks.

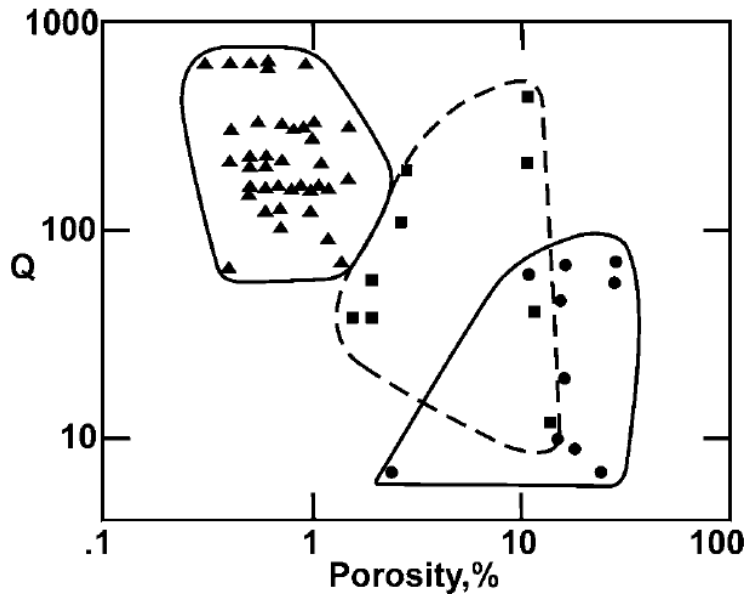


Figure 2.2: Q as a function of porosity for igneous and metamorphic rocks (triangles), limestones (squares), and sandstones (circles). Q is generally inversely proportional to porosity. The data in this plot do not distinguish between frequency nor degrees of saturation. Data for this plot comes from Bradley and Fort (1966) and was reproduced by Johnston et al. (1979).

2.2 ATTENUATION FACTORS

2.2.1 Frequency

For homogenous solids and dry rocks, at least for limited bandwidths, Q can be approximated to be independent of frequency. One of the earliest studies looking into the frequency dependence of attenuation was performed by Birch and Bancroft (1938). They studied a cylindrical piece of Quincy granite and found that that attenuation was constant over the measurement frequencies. Further publications showing similar results were published by Bruckshaw and Mahanta (1961) who measured attenuation in sedimentary and igneous rocks, Knopoff (1964) who provides a review of attenuation in a variety of materials, Pandit and Savage (1973) who measured attenuation of sandstone samples, and Madonna and Tisato (2013) who measured attenuation of Barea sandstone. In all these

studies the materials that were being tested were dry and homogenous, and all results showed that attenuation was constant over the frequencies at which they measured attenuation.

Studies were also conducted on rocks that were saturated. Born (1941) found that attenuation increased with frequency when samples of Amherst sandstone contained water in their pore space. He also found that attenuation was constant when the same samples of Amherst sandstone were dry. Winkler and Nur (1982) tested dry and saturated samples of Berea sandstone at various frequencies and found similar results. These discoveries suggested that pore fluids play a major role in causing attenuation in rocks.

It is now well known that the attenuation coefficient of a material is frequency dependent (Barton, 2007) for all (both dry and saturated) non-elastic materials when considering a large range of frequencies. This is also true for liquids such as water (Pinkerton, 1947). The dependence of frequency on attenuation in rocks is complex and depends on the amount of saturation but generally at low frequencies, attenuation increases with increasing frequency for rocks that are not completely saturated. At some frequency, though, attenuation reaches a maximum and then starts to decrease with increasing frequency for partially saturated rocks as well (Winkler and Nur, 1982; Murphy, 1982).

2.2.2 Strain Amplitude

When elastic waves propagate through a material, the molecules of the material are deformed. Seismic waves typically impose strain amplitudes on the order of 10^{-6} to materials (Karato and Spetzler, 1990).

Attenuation looks independent of strain amplitude on rocks for strains less than 10^{-6} (Gordon and Davis, 1968). Winkler et al. (1979) found that materials containing no

microcracks such as Lucite, Vycor, and aluminum exhibited no strain amplitude dependence of attenuation.

At higher strains, however, strain amplitude dependence on attenuation begins to occur. Winkler et al. (1979) measured the attenuation of Massillon sandstone and Berea sandstone using a resonance bar technique at various strain amplitudes. They found that attenuation rapidly increases at strains above 10^{-6} for both samples. Tisato and Quintal (2014) also found that attenuation increased with strain in samples of Berea sandstone at low frequencies. Tutuncu et al. (1998) made measurements of sandstones at even higher strain amplitudes and frequencies, 10^{-5} to 10^{-3} , and found that attenuation continued to rapidly increase with strain amplitude.

2.2.3 Fluid Saturation and Type

Fluids that are contained in the pore spaces of rocks are called pore fluids. When the pores of a rock are completely filled with fluids, the rock is said to be completely or fully saturated. If the pore space is only partially filled with pore fluids, the rock is said to be partially saturated. It is important to note that it is difficult to remove all pore fluids and have a completely dry rock. A single layer of pore fluid molecules will remain in small cracks and coating the grains of the rock. The amount of pore fluid that cannot be removed in the pore space is called the irreducible water saturation of the rock.

The degree of saturation of a rock influences its attenuation. Attenuation increases with increasing fluid saturation at surface conditions. Various studies on this topic have been reported in Murphy et al. (1986), Yin et al. (1992), and Batzle et al. (2006). In these studies, water was the pore fluid that was used to saturate the rocks. Their results show that attenuation rapidly increases below 20 percent saturation and then slowly increases

until the rock is almost completely saturated. At complete saturation, however, attenuation decreases (Batzle et al., 2006).

2.2.4 Temperature

Temperature varies with depth in the Earth's subsurface and increases with depth. The geothermal gradient, the rate at which temperature increases with depth, of the Earth's crust is about 25-30 °C/km (Fridleifsson et al., 2008). This temperature change is caused by the convection of heat that is generated from the decay of natural radioactive isotopes in the mantle and core. Hydrocarbon exploration takes place in a wide variety of depths and thus temperatures too. For this reason, it would be useful to know if temperature has any effect on the attenuation of rocks and fluids.

Although temperature does not have much of an effect on the attenuation of dry rocks at upper crustal temperatures, it does influence saturated rocks. As discussed previously the viscosity of the pore fluid significantly affects the attenuation of a rock. The viscosity of a fluid changes with temperature. This is a well-known phenomenon and has been closely investigated for various fluids (Kestin et al., 1978; Seeton, 2006). Batzle and Wang (1992) also showed how the viscosity of hydrocarbon gases, oil, and brine are affected by temperature. Generally, the viscosity of a fluid decreases with increasing temperature, which increases the attenuation of the rock. This effect can be modeled by the unified Biot and Squirt model (Dvorkin and Nur, 1993). At lower viscosities, pore fluids can more easily move which gives rise to more viscous friction loss and squirt-flow which leads to more attenuation.

At temperatures in the shallow subsurface most of the effect temperature has on attenuation is due to the altering the viscosity of the pore fluid. The effect of temperature on the matrix and structure of the rock is negligible. This conclusion is found in Jones

and Nur (1983) where they measured the attenuation of a water-saturated sandstone at various temperatures and found that the change in attenuation is caused by change in pore fluid viscosity and not by the alteration of the grains and matrix with temperature.

2.3 ATTENUATION MECHANISMS

A complete description of how energy from seismic waves attenuates in all materials has not fully been proposed. Working theories to explain attenuation rely on the combination of separate individual attenuation mechanisms to model the total attenuation of a material.

2.3.1 Rocks

Every material attenuates waves that propagate through it. Zener (1938) established a theory explaining the intrinsic attenuation of some materials. His theory states that attenuation arises from microscopic stress inhomogeneities. These inhomogeneities are caused by imperfections such as cavities, from the results of cold working, and from microcrystalline anisotropy. This gives rise to local temperature fluctuations in vibrating material and local heat flow. These heat currents increase the entropy of the vibrating solid and are a source of internal friction. This theory though could only be used to explain only some of the internal friction. Zener (1940) found another mechanism for crystalline materials, such as metals, involving energy loss when dislocations occur in the crystal lattice during wave propagation. Read (1940) investigated this mechanism and confirmed its validity.

For rocks, which are a collection of minerals grains with different shapes and pore fluids, a complete description of how energy attenuates is complex. There are several attenuation mechanisms contributing to energy dissipation.

In the matrix of a rock, attenuation can be caused by both the intrinsic anelasticity of the minerals in the matrix and by frictional dissipation due to relative motions at grain boundaries and cracks. The quality factor, Q , of individual mineral crystals is generally high with values in the thousands, whereas Q values of rocks are much lower with values in the hundreds. Therefore, attenuation in the matrix due to the intrinsic anelasticity of the minerals is negligible (Johnston et al., 1979). This leaves frictional dissipation as the main mechanism to explain how seismic waves attenuate in the rock matrix.

When two surfaces are in contact and are moving against each other, energy is lost in the form of heat. As a seismic wave propagates through a rock, the grains deform anelastically causing part of the seismic wave to lose energy in the form of heat. The same happens across cracks. This theory is supported by experimental evidence that attenuation increases in saturated rocks (Clark et al., 1980). If the grains in a rock are dry, then the coefficient of static friction between grains is high, which would prevent many grains from sliding past each other resulting in little energy loss, so attenuation would be small. With wet grains, however, the grains essentially become lubricated, and the coefficient of static friction would decrease and allow more grains to slide, which would increase attenuation. Walsh (1966) provided a formulation to calculate the friction mechanism from contacts between the surfaces of thin ellipsoidal cracks. This mechanism cannot fully account for all attenuation though as Walsh (1966) pointed out that rocks that have been subjected to pressures that close all cracks still have non-zero attenuation.

Winkler and Nur (1982) made the observation, though, that attenuation is independent of strain amplitude below amplitudes of 10^{-6} and at confining pressures typical of those in the shallow crust. They concluded that frictional sliding is not a significant source of attenuation of seismic waves in the shallow crust. Savage (1969)

also pointed out a problem with the frictional attenuation mechanism. He showed that for typical strain amplitudes of seismic waves and for typical microcrack dimensions in rocks that the computed slip across grain boundaries would be on the order of 10^{-12} meters, which is less than the distance of interatomic spacing between atoms. This suggests that other mechanisms are needed to describe attenuation in rocks.

Rocks containing pore fluids generally exhibit greater attenuation values than do dry rocks (Wyllie et al., 1962; Gardner et al., 1964; Murphy et al., 1986). One proposed mechanism, aside from grain boundary friction, is pore fluid flow relative to the rock matrix (Biot, 1956 a,b). As summarized by Winkler and Nur (1982), when the rock frame is accelerated by an acoustic wave, shear stresses are generated within the pore fluid. These stresses decay exponentially away from the pore wall with a viscous skin depth that decreases with increasing frequency. Thus, this mechanism is only significant at ultrasonic frequencies.

Another mechanism caused by fluid flow is intercrack fluid flow (Mavko and Nur, 1975; O'Connell and Budiansky, 1977). This fluid flow is sometimes regarded as "squirt flow". This mechanism occurs as cracks are compressed by various amounts depending on their shape and orientation with respect to the seismic wave. The compression causes pore fluids to flow between cracks.

2.3.2 Fluids

Several mechanisms of attenuation in fluids have been observed. For fluids containing gas bubbles a mechanism called wave-induced-gas-exsolution-dissolution (WIGED) has recently been observed (Holocher et al., 2003; Tisato et al., 2015). In the situation of a seismic wave propagating through a bubbly liquid, the size of the gas bubbles will change as the wave passes by. Most of the energy is lost because of the time

delay between the shape of the bubble and the pressure change. Part of the energy is lost due to friction in the form of heat when the dissolved gas moves with respect to the fluid. When the pressure increases in the bubble the gas will dissolve into the liquid and the bubble will shrink. Near the bubble, the concentration of dissolved gas is high compared to the concentration far away from the bubble. The dissolved gas will in response diffuse and try to equilibrate. When the seismic wave decreases the pressure in the bubble the dissolved gas exsolves back into the bubble and the bubble will grow. The movement of the dissolved gas again causes energy to be lost.

For fluids containing entanglements such as polymers dissolved in a fluid, there are several attenuation mechanisms. One of which is known as the reptation model. This mechanism involves the diffusion of the chains of the solute along their contours. This mechanism has been modeled by Doi and Edwards (1988).

In solutions in which concentration of solutes is high, there is a critical concentration called the gel concentration in which an attenuation mechanism can take place. Above the gel concentration the solution consists of large clusters of entangled solutes that are singularly connected to each other via what are termed “critical bonds” (Wientjes et al., 2000). When a critical bond is broken a cluster is released from the entangled network and relaxes in a Rouse-like manner. Semenov and Rubinstein (1998) present a model to explain this.

Another attenuation mechanism in polymer solutions is called hindered reptation and was modeled by Leibler et al. (1998). This mechanism involves the diffusion of stress along an entangled polymer chain. When stress is applied to the chain, some of the bonds will break temporarily. During this time of breakup, the chains will rotate, and the bonds will be restored. This results in chains with random orientations which is the main source of energy loss.

2.4 ATTENUATION MEASUREMENT METHODS

Methods to measure the attenuation of fluids can be separated into three categories. The three methods are ultrasonic, resonance, and forced oscillation.

2.4.1 Ultrasonic

The first method is the ultrasonic method. This method measures the attenuation at high frequencies (kHz to MHz range). This method works by placing transducers on opposite sides of a sample. One of the transducers works as the source and the other one works as the receiver. Attenuation is then calculated by measuring the decrease in amplitude of wave multiples (Peselnick and Zietz, 1959) or by the spectral ratio method (Toksoz et al., 1979). This method can only measure attenuation at high frequencies because the wavelet that is produced from the transducer is inherently high frequency. Eggers and Kaatze (1996) reviewed the ultrasonic method for liquids. Another method that was performed by Strohm and Kolios (2011) used photoacoustic techniques. This method measures attenuation in the MHz range.

2.4.2 Resonance

The second method is the resonance method. This method measures the attenuation at frequencies between about 100 to 50,000 Hz. This method works by first vibrating a sample of the material that is being tested up to its resonant frequency. The attenuation is then measured in one of two ways. For small values of attenuation ($Q > 10$) attenuation is measured from the width of the resonance peak (Gardner et al., 1964). Otherwise attenuation can be measured from the resonance decay (Winkler and Nur, 1982). The frequency at which attenuation of the material is being tested is purely determined by the resonance frequency of the shape of the material. Although it is theoretically possible to measure the attenuation of the material at low frequencies, it is

not practical because very long samples would be needed to achieve resonance frequencies that are comparable to seismic frequencies. Fisher and Simmons (1977) used the resonant bar method on a sphere of sea water to measure attenuation in the kHz region.

2.4.3 Forced Oscillation

The third method is the forced oscillation method. This method can measure attenuation at frequencies below 1000 Hz. This method is ideal for measuring attenuation at seismic frequencies. This method works by applying a sinusoidal stress to a material and measuring the resulting strain. The phase delay between the stress and the strain is then calculated. The attenuation of the material at the frequency at which the stress was applied is calculated from the phase delay using equation 2.6. There is a lack of measurements of the attenuation of fluids at seismic frequencies using the forced oscillation method. The forced oscillation method has been applied to rocks (Tisato and Quintal, 2015; Madonna and Tisato, 2013).

2.5 BULK MODULUS

The amount an object strains when a stress is applied varies among materials. An elastic modulus is a quantity that measures the objects resistance to being deformed. It is defined as the ratio of the applied stress to the resulting strain. A material that requires more stress to deform is considered stiffer and has a higher elastic modulus compared to a material that is more easily deformable. In the case of volumetric deformation, the bulk modulus is the elastic modulus that is used to describe resistance to a change in volume. The bulk modulus, K , of an object can be defined by

$$K = -V \frac{dP}{dV} \quad (2.12)$$

where P is pressure and V is volume. The bulk modulus is related to the speed at which a seismic wave propagates through a fluid by

$$K = \rho c^2 \quad (2.13)$$

where ρ is the density of the material and c is the speed a seismic wave propagates through the material. The speed at which seismic waves propagate through a material is called the speed of sound in that material.

2.5.1 Bulk Modulus Measurement Methods

The bulk modulus is commonly measured in two ways. The first method involves measuring the speed of sound of the material and then calculating the bulk modulus from that value. Smith et al. (1960) reviewed three main methods of measuring the speed of sound of a material. These methods measure ultrasonic frequencies, and it is not straightforward to extend them to lower seismic frequencies. The other commonly used method involves compression tests. In this method a material is subjected to an external pressure, and the change in volume of the material is measured. The bulk modulus can then be calculated from these two quantities. Dymond et al. (1985) used this method to measure the bulk modulus of various oils. These static compressibility tests effectively measure the approximate zero-frequency bulk modulus of the material.

The properties of a liquid are substantially affected by air or other gasses. Gholizadeh et al. (2011) reviewed this topic along with methods of measuring the bulk modulus of fluids. It is therefore very important to make sure air is removed from the

liquid and container before its properties are measured. Air can exist in liquids in three ways. The first is free air. This most often occurs when a container is filled with a liquid and sealed. A small layer of air will always remain at the top of container. If the bulk modulus of a liquid with a small layer of air were measured it would actually be the effective bulk modulus of the combination of the liquid and air. It has been found that dissolved air does not significantly affect the bulk modulus of liquids (Golizadeh et al., 2011).

To show how much entrained air affects the bulk modulus of a fluid, a calculation with water is given below. At atmospheric pressure the bulk modulus of water is 2.2 GPa and the bulk modulus of air is 142 kPa. The air bubble and the water in a container will experience iso-stress conditions when the container is pressurized. A first order approximation is the Reuss average to calculate effective bulk modulus. Using the Reuss average it can be shown that when air is present in only 6 parts per million the bulk modulus of the water decreases to 2 GPa or decreases by 10 percent.

$$\frac{1}{K} = \frac{f1}{K_{water}} + \frac{f2}{K_{air}} \quad (2.14)$$

$$\frac{1}{K} = \frac{0.999994}{2.2 \text{ GPa}} + \frac{0.000006}{0.000142 \text{ GPa}} \quad (2.15)$$

Chapter 3: Methodology

3.1 OVERVIEW OF EXPERIMENT

To measure the low-frequency attenuation of liquids, low-frequency dynamic compressibility tests were performed on various liquids by means of the sub-resonances method described by O'Connell and Budiansky (1978). A sinusoidal pressure was applied to the test fluid, and the phase delay, ϕ , between the fluid pressure and resulting strain was measured. Equation 2.6 gives the Q value of the material at the frequency at which the sinusoidal pressure was applied. The real part of the bulk modulus is given by equation 2.7, and the imaginary part of the bulk modulus is given by equation 2.8.

Several parameters can be modified in the experiment to reproduce a variety of reservoir conditions relevant for hydrocarbon production. These parameters include controlling the frequency and strain at which the fluid is compressed and relaxed, the fluid type and viscosity, and the absolute pressure experienced by the fluid. A description of how these parameters are controlled is given later in this chapter.

The experiment starts by placing a liquid inside a pressure vessel and setting a piston in the pressure vessel above the fluid so it is in direct contact with the fluid. The piston creates a seal to ensure that the fluid does not leak out of the top of the vessel when it is compressed during the experiment. The bottom of the vessel is also sealed. A piezoelectric motor compresses the fluid. The piezoelectric motor is attached to the piston so when the piezoelectric motor expands the piston moves downward in response and compresses the fluid. The vessel and the motor are placed inside a screw press to hold all the components and isolate them from outside disturbances. The voltage that was applied to the piezoelectric stack was varied so that it generates a sinusoidal pressure to the fluid by expanding and contracting at a controlled frequency. The experiment was run at

frequencies as low as 0.1 Hz and as high as 20 Hz. A displacement sensor is attached to the piston to measure the shortening of the sample. This can be used to estimate the volumetric strain of the fluid during the experiment if it assumed that the sample does not expand horizontally during the experiment. A pressure sensor was fitted to the bottom of the pressure vessel to measure the pressure of the fluid during the experiment. The phase delay between the measured pressure and shortening signals is then calculated, and $1/Q$ can be determined for the frequency at which the piezoelectric motor expanded and contracted.

3.2 FLUID FLOW CONSIDERATIONS

The test fluid is compressed and relaxed in a sinusoidal pattern at a known frequency. Because the fluid is being compressed, the individual fluid molecules will move up and down in the pressure vessel. Thus, the test fluid flows in the vessel during the experiment. It is therefore important to first investigate fluid dynamics.

The first aspect of fluid flow to consider is the Reynolds number. The Reynolds number is a dimensionless quantity that describes flow patterns. It is defined as the ratio of the internal forces to the viscous forces in the fluid (Reynolds, 1883). The Reynolds number of a flow depends on the geometry of the fluid flow among many other factors. For this experiment the fluid is being tested in a cylindrical vessel so the flow can be said to be taking place in a cylindrical pipe. The Reynolds number of the fluid flow in a pipe is given by equation 3.1

$$Re = \frac{\rho u D}{\mu} \quad (3.1)$$

where ρ is the density of the fluid, u is the mean velocity of the fluid, D is the diameter of the pipe, and μ is the dynamic viscosity of the fluid.

Fluid flows that are characterized by low Reynolds numbers are said to be laminar flows. A laminar flow is a type of fluid flow in which the fluid flows in parallel layers. This means there are no eddies or swirls, and the fluid does not mix with itself. Fluid flows that are characterized by high Reynolds numbers are said to be turbulent flows. A turbulent flow is a type of fluid flow where the layers of the fluid mix, and eddies and swirls exist in the flow. Another important distinction between laminar and turbulent flow is that the fluid pressure in laminar flow is constant everywhere while the pressure can vary throughout the flow in turbulent flow.

It is important to know whether the flow in the pressure vessel of this experiment is laminar during the experiment. When taking measurements of fluid properties, it is important that the fluid is a homogenous material. If there are certain areas where the pressure or the velocity of the flow is higher than in other areas, the results of the property measurements that are taken could be affected. The Reynolds number at which a fluid flow begins to change from laminar to turbulent flow is called the critical Reynolds number. The critical Reynolds number is different for every flow geometry and other conditions. For fluid flow in a pipe the critical Reynolds number is about 2,300 (*Yunus and Cimbala, 2006*).

During the compression and release of the fluid during the experiment, the Reynolds number of the flow will vary with the depth of the pressure vessel at every moment. This is a result of compressing the fluid from only one side of the vessel. As the fluid is compressed from the top the fluid molecules closer to the top of the vessel will move further than the fluid at the bottom of the vessel. This is demonstrated in figure 3.1 where the block on the right is compressed to half the length of the block on the left. Points on the left block are mapped to the locations on the compressed block as represented by the arrows. It is clear from the figure that the top of the block moves much

further than the bottom of the block. This means that the velocity of the fluid flow is not constant with depth in the pressure vessel because the molecules of fluid at each depth must move a different distance in the same amount of time. Figure 3.2 shows an example of how the Reynolds number of the flow in the pressure vessel varies with depth at the moment at which the fluid flow is fastest. This is the maximum Reynolds number that the flow will experience during the experiment. A plot similar to this was made for each set of experimental parameters before it was tested to make sure the Reynolds number did not exceed 2,300.

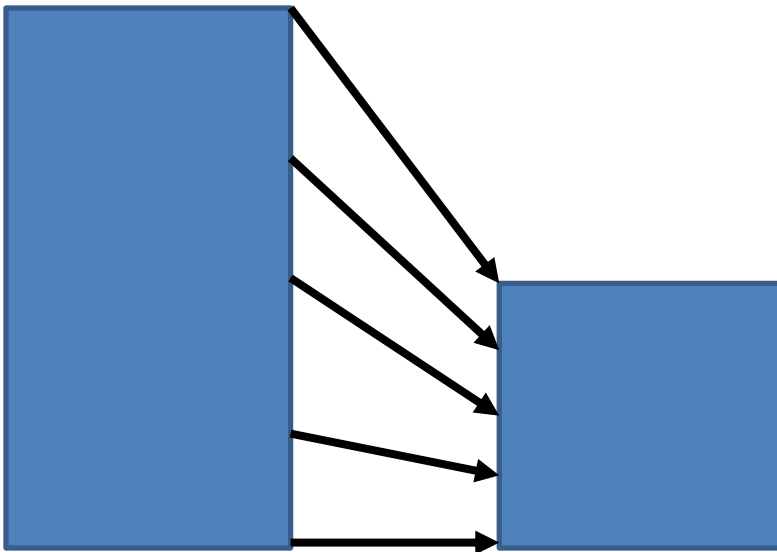


Figure 3.1: Demonstration of how the material at the top of a block moves further than the material at the bottom when the block is compressed. This shows how fluid flow in the pressure vessel is not constant with depth and the Reynolds number will also vary with depth.

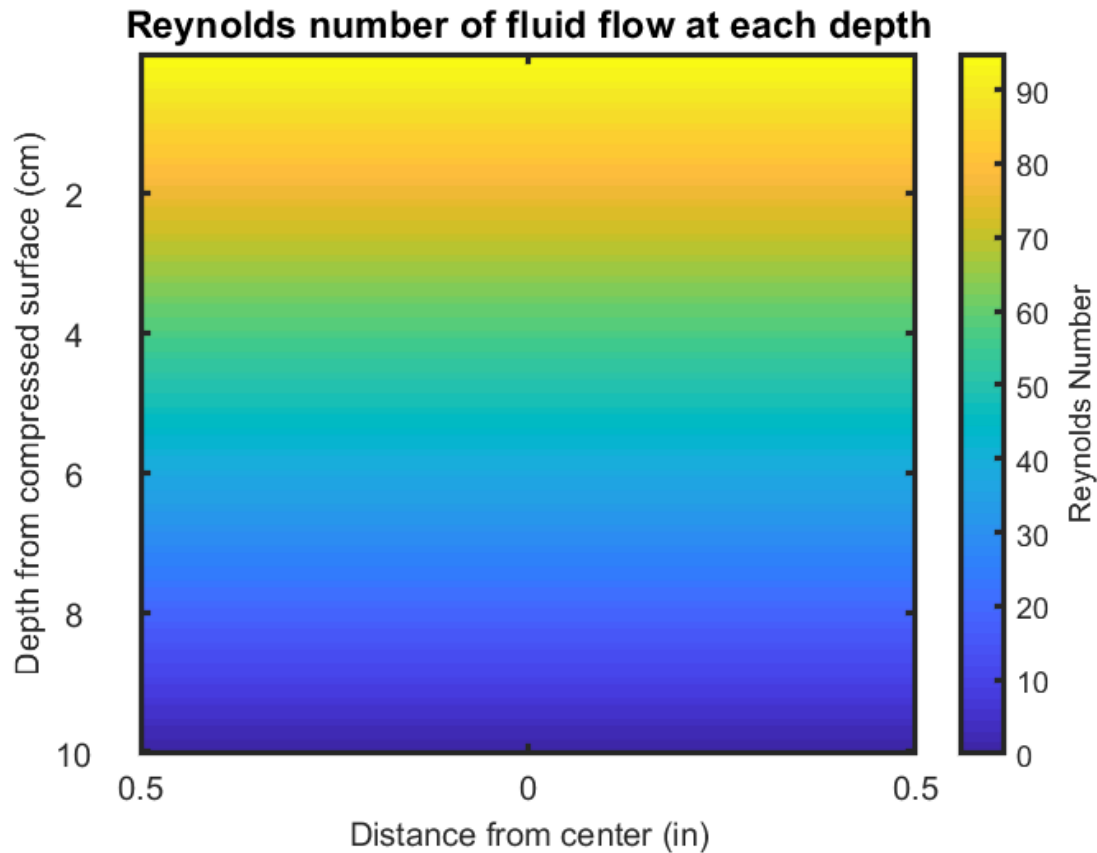


Figure 3.2: Reynolds number in the vessel at various depths for an experiment with a vessel length of 10 cm, fluid viscosity of 0.001 Pa*s, fluid density of 1000 kg/m³, fluid compression of 30 micrometers, and frequency of compression of 20 Hz. The compression and frequency are on the high side of the parameters used during testing. Therefore, actual Reynolds numbers would be lower. This figure shows the Reynolds number only in the pressure vessel. The pipe has a smaller radius so the Reynolds number would be smaller. Reynolds number changes with depth because the fluid at the bottom of the vessel does not move as far as the fluid on top. Flows with Reynolds numbers of less than 2300 for a cylindrical pipe are laminar.

Another issue to consider is the size of the boundary layer of the flow and how developed the flow is. In a fluid flow, the fluid at the solid boundary of a pipe will have zero velocity relative to the boundary. This is known as the no-slip condition (Day, 1990). Fluid flow close to the pipe wall will be slower relative to flow at the center of the

pipe due to friction. Fluid flow in the center of the pipe will be the fastest in order to keep the mass flow rate through the pipe constant (Yunus and Cimbala, 2006). This results in a velocity gradient over the pipe cross section. For laminar flow, the velocity profile of the flow starts out as constant along the pipe and eventually forms a parabolic shape where the flow velocity is zero at the boundary of the pipe and maximum at the center of the pipe. The distance a fluid has to flow in order to achieve a parabolic shape is known as the hydrodynamic entry length. A fluid flow that has passed the hydrodynamic entrance length is called a fully developed flow. A fluid flow that has not passed the hydrodynamic entrance length is called an undeveloped flow (Yunus and Cimbala, 2006). Figure 3.3 shows the development of a fluid flow with velocity profiles of the flow at various points throughout the flow. The flow starts on the left side where the velocity profile is constant throughout the pipe and the flow moves towards the right where it eventually becomes fully developed when the velocity profile is parabolic in shape.

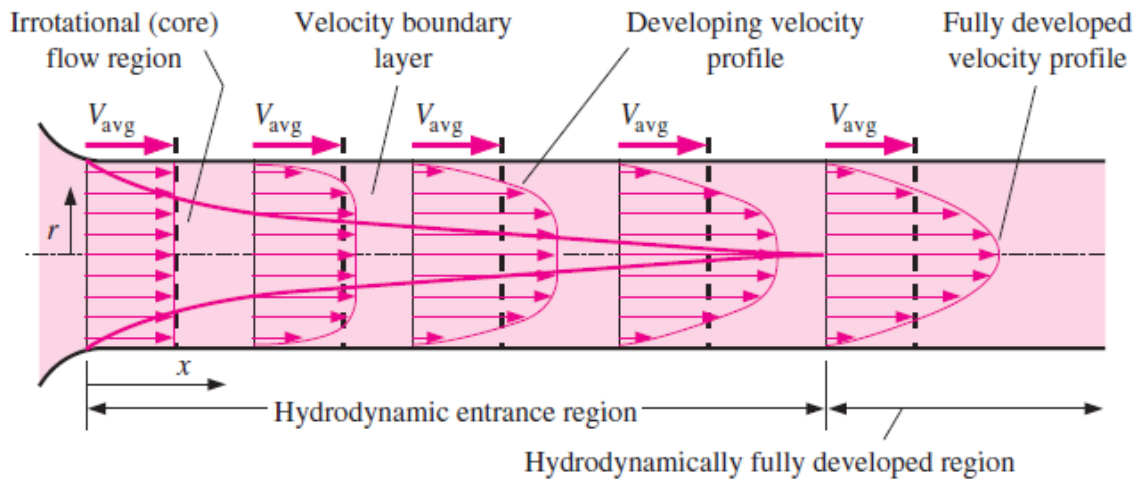


Figure 3.3: The development of a fluid flow moving from left to right. The velocity profile of the flow is shown at several points throughout the flow. The velocity profile is constant throughout the flow and eventually makes a parabolic shape when it is fully developed. The figure also shows the boundary layer and how it increases as the flow develops. The velocity profile is constant while in the boundary layer. Figure from Yunus and Cimbalá (2006).

The boundary layer of a flow is a layer of the fluid in which the effects of the viscous shearing forces caused by fluid viscosity are significant (Yunus and Cimbalá, 2006). In this region the velocity profile is not constant. The region of the flow where frictional effects are negligible is called the irrotational flow region (Incropera et al., 2007). In this region the velocity profile is nearly constant. The boundary layer increases as the flow develops. This is also shown in figure 3.3.

For our experiments it would be best to have the flow be as underdeveloped as possible because fluid-vessel interaction could affect the results. This means that the experiment would work best when the boundary layer is as small as possible, and the flow is as undeveloped as possible. The hydrodynamic entrance length of a flow in a cylindrical pipe can be calculated from equation 3.2 (Kays and Crawford, 1993)

$$L = \frac{d}{20} Re \quad (3.2)$$

where L is the hydrodynamic entrance length, d is the diameter of the pipe, and Re is the Reynolds number of the flow. For this experiment d is 1 inch and the Reynolds number can go up to 2,300. These numbers give an entrance length of about 1 meter. The maximum displacement of the fluid flow in this experiment is equivalent to less than 0.1% of the length to fully developed flow. This means that the flow in the vessel during the experiment is nowhere near fully developed, and it is safe to assume the velocity profile of the flow is constant throughout. The same can be said about flow in the pipe because the diameter is smaller than the diameter of the vessel.

The thickness of the boundary layer for this experiment can be approximated by equation 3.3 (Schlichting and Gersten, 2016)

$$\delta \approx \frac{5x}{\sqrt{Re}} \quad (3.3)$$

where δ is the thickness of the boundary layer, x is the distance from the start of the flow, and Re is the Reynolds number of the flow. Using typical values for this experiment, the boundary layer is found to generally be less than 0.1% of the vessel diameter, so it is safe to assume that the effects of the viscous shearing forces caused by fluid viscosity are not significant.

3.3 DESCRIPTION OF FLUIDS TESTED

The attenuation and bulk modulus at low frequencies of two types of fluids were tested. The first was deionized water, which is water that has had almost all of its mineral ions removed. Water was chosen to test because of its availability and so that results

could be compared to already published Q values. The second type of fluid tested was various concentrations of aqueous guar gum solutions. Guar gum comes in a powder and is added to water in various amounts to control concentration. Guar gum is a galactomannan obtained from the endosperm of the *Cyamopsis tetragonolobus* seed. The guar gum powder is prepared by first breaking the seeds and separating the germ from the endosperm. The endosperms are then polished to remove a fine layer of fibrous material. What results is referred to as guar splits. The splits are then crushed and ground down to a desired particle size and is now considered guar gum powder (Mudgil et al. 2014).

The chemical structure of guar gum consists of a principle backbone chain of mannose units with single galactose units linked to the principal chain. Figure 3.4 shows the chemical structure of guar gum. The galactose side units are not distributed evenly along the backbone chain but instead show a random distribution with a ratio of mannose to galactose units in the range of 1.6:1 to 1.8:1 (McCleary et al., 1985). Water bonds to guar via hydrogen bonding to hydroxyl groups on the chain (Mudgil et al. 2014).

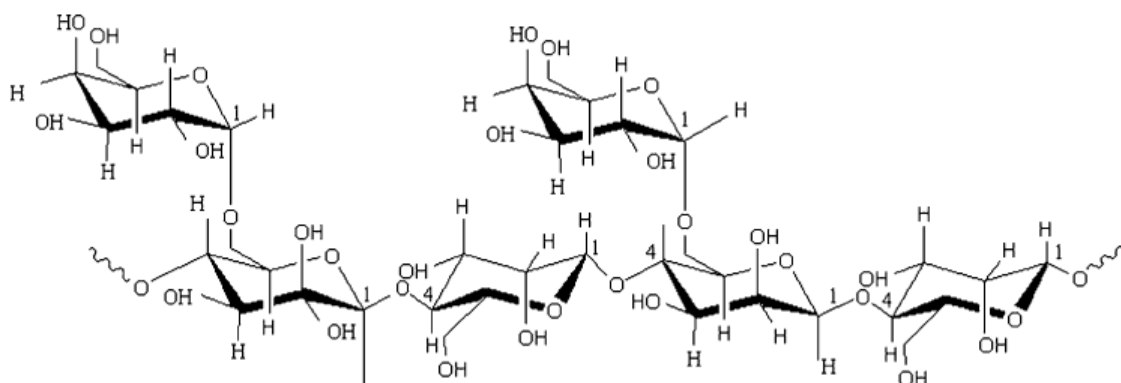


Figure 3.4: Chemical structure of guar gum. Galactose units are linked to a principle backbone chain of mannose units. Figure from Mudgil et al. (2014).

Guar gum has many commercial uses including additives in food, pharmaceuticals, paper, textile, explosives, cosmetics, and the oil and gas industry (Mudgil et al., 2014). Guar gum is used primarily as a thickening agent. Small amounts of powdered guar added to water can drastically change the viscosity of the water. Guar gum also has the property of keeping particles in suspension longer. Guar gum is used in hydraulic fracturing fluid to better transport proppant to fractures during hydraulic fracturing, which is why it is of interest to test at seismic frequencies.

The viscosity of guar gum solutions increases proportionally with guar powder concentration (Robinson et al., 1982). Typical concentrations in commercial uses are less than 1% weight (Mudgil et al., 2014). Viscosity increases with guar gum because of the interaction between the galactose side chain of the guar molecule with the water molecule. An increase in concentration also increases the inter-molecular chain interactions of the guar molecule which causes entanglement which leads to an increase in viscosity (Mudgil et al., 2014).

The guar gum samples that were tested had concentrations of 10, 20, and 40 pounds of guar gum per thousand gallons of water (ppt). Converting to SI units gives concentrations of 1.2, 2.4, and 4.8 g/L respectively. This range of tested concentrations of guar gum is commonly used in hydraulic fracturing operations. ECOPOL-5000 Guar Based Gelling Agent provided by Economy Polymers & Chemicals was used. Samples were prepared by slowly adding guar gum powder to a beaker of water that was being stirred by a stirring plate.

The viscosity of a guar gum solution depends on how long the sample has been mixing because it takes time for all the guar gum molecules to hydrate. To demonstrate this, the viscosity of a 10 ppt sample was measured at several amounts of time stirred and the results are plotted in figure 3.5. From the figure, viscosity increases rapidly for about

the first thirty minutes and then starts to approach a steady value. The viscosities of the sample were measured using a falling ball viscometer. A falling ball viscometer uses the time it takes for a ball of known diameter and density to fall through the fluid in a cylinder of known diameter to calculate viscosity. Each sample was stirred for at least one hour before it was tested to ensure that every sample with the same concentration had the same viscosity.

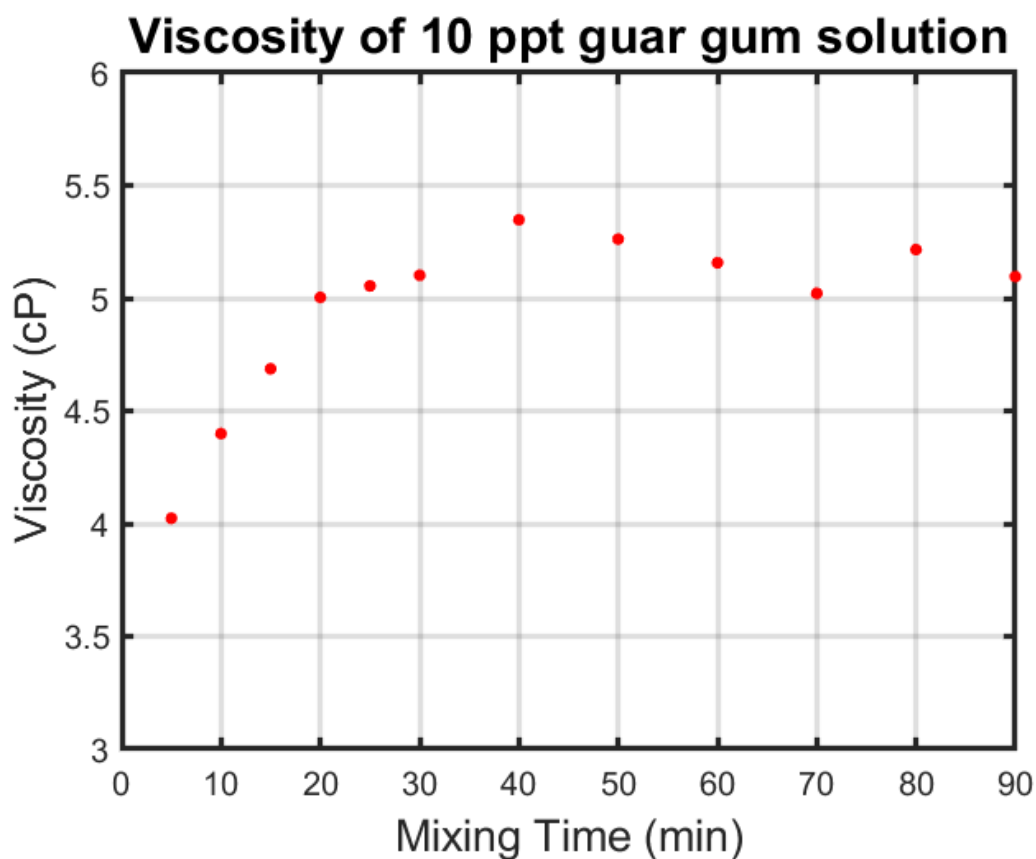


Figure 3.5: Viscosity of 10 ppt guar gum solution as a function of the amount of time it had been mixed. The viscosity rapidly increases during the first thirty minutes and then starts to reach a steady value. Samples of guar gum were mixed for at least an hour before they were tested to make sure that each sample made with the same concentration had the same viscosity.

3.4 DESCRIPTION OF THE MACHINE

A schematic and section view of the experimental design are given in figure 3.6 with the major components labeled. A complete labeled drawing of each part of the machine with a bill of materials is given in figure 3.7. Detailed drawings of each custom-made part are given in the Appendix. This section contains a description of the parts used for the frame of the experiment.

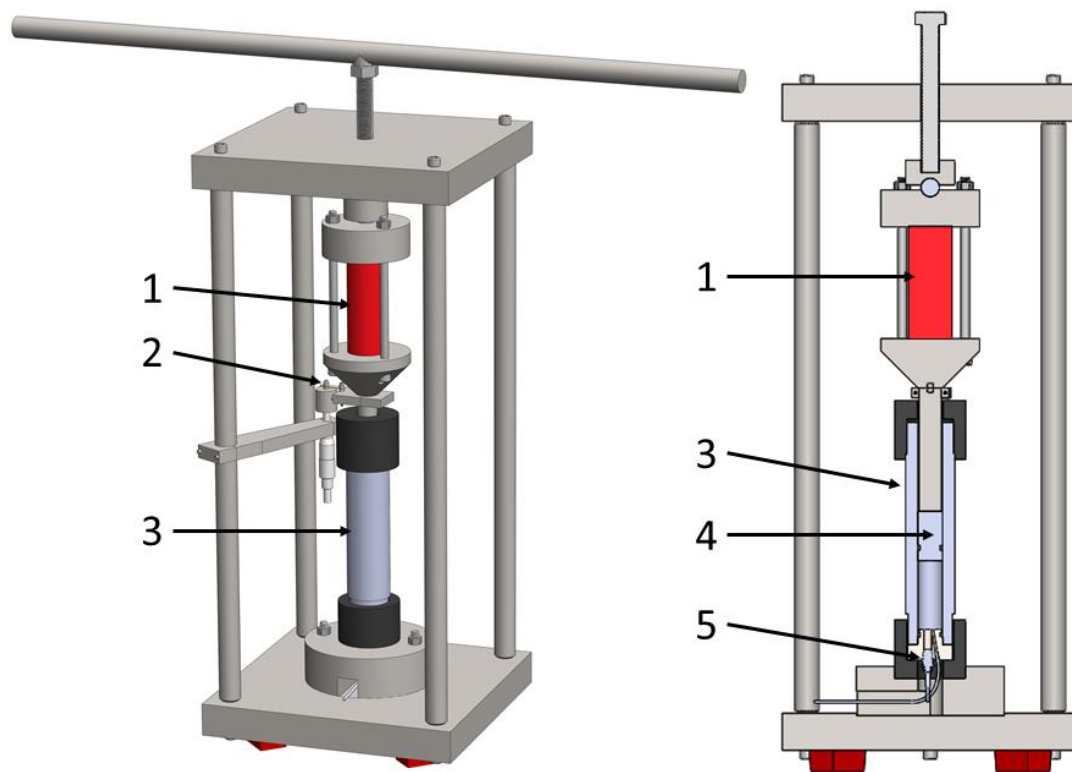
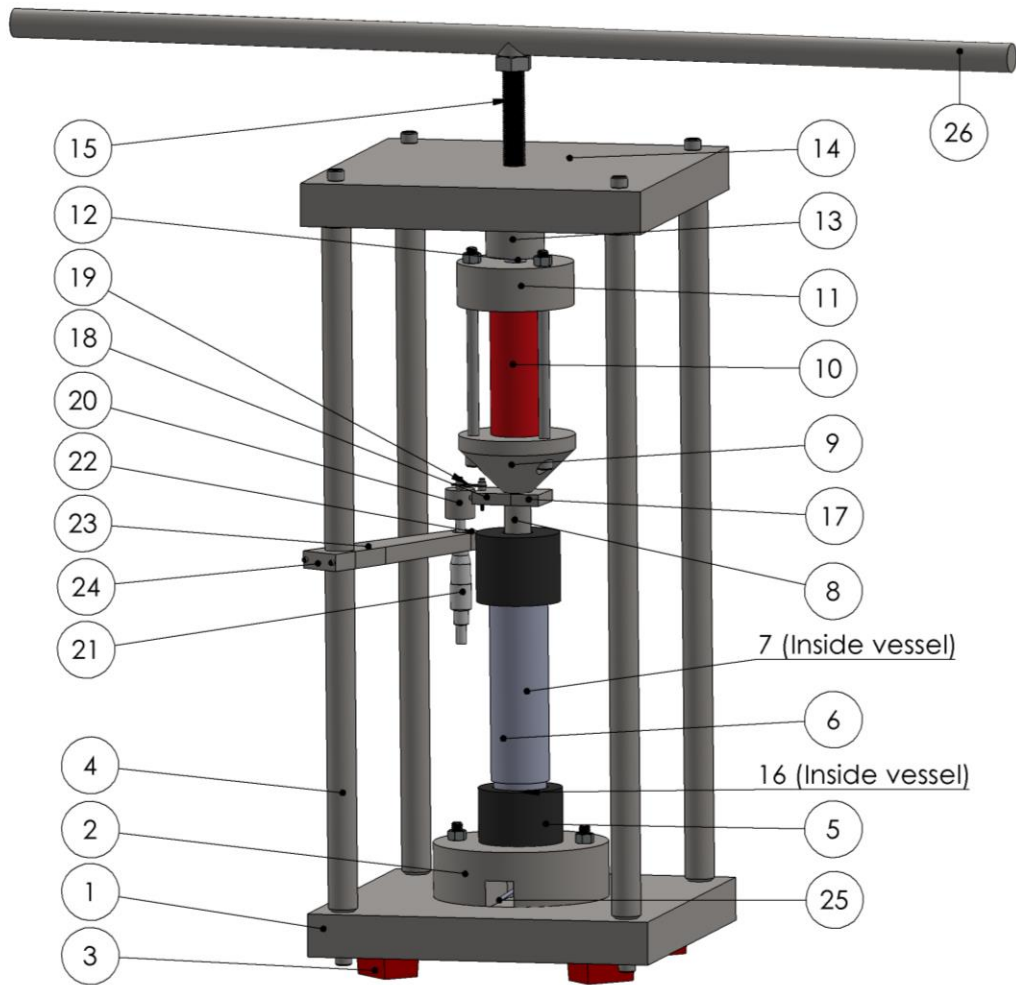


Figure 3.6: Schematic and section view of the machine used to measure the low-frequency attenuation of fluids. The major components are labeled. The fluid sits inside the pressure vessel (#3) and is brought up to the desired pressure using a fluid pump. A voltage will be applied to the piezoelectric motor (#1) which will cause the motor to expand which will then move the piston (#4) downward and compress the fluid. A pressure sensor (#5) will measure the pressure of the fluid during the experiment and a displacement sensor (#2) will be attached to the piston to measure the shortening of the fluid sample.



ITEM NO.	PART	QTY.	ITEM NO.	PART	QTY.
1	Bottom Plate	1	14	Top Plate	1
2	Vessel Base	1	15	Middle Screw	1
3	Bumper	4	16	Vessel Cover	1
4	Support Rod	4	17	Lip 1	1
5	Vessel Cap	2	18	Lip 2	1
6	Pressure Vessel	1	19	Displacement Sensor	1
7	Piston	1	20	Cap	1
8	Middle Piston Rod	1	21	Micrometer	1
9	Piston Top	1	22	Lip 3	1
10	Piezoelectric Motor	1	23	Lip 4	1
11	Swivle Block Bottom	1	24	Lip 5	1
12	Ball	1	25	Pipe	1
13	Swivle Block Top	1	26	Handle	1

Figure 3.7: Schematic of the machine and a bill of materials showing the name and quantity of each part.

All custom-made parts were made of 304 stainless steel except for the “vessel cap” part, which was made of 316 stainless steel. The “bottom plate” is a rectangular block that is 1.5 inches thick. Four holes are drilled through in the corners for the bolts that attach to the support rods. Four more holes are tapped through the bottom side where the bumpers are screwed into. A small circular divot is carved into the top of the plate for the “vessel base” to sit on. The “vessel base” is a cylindrical piece that holds the pressure vessel in place. The “vessel base” also has a square hole cut into the side of it for the pipe and the wiring of the pressure sensor to attach to the vessel. Figure 3.8 shows a closeup section view of the bottom of the machine.

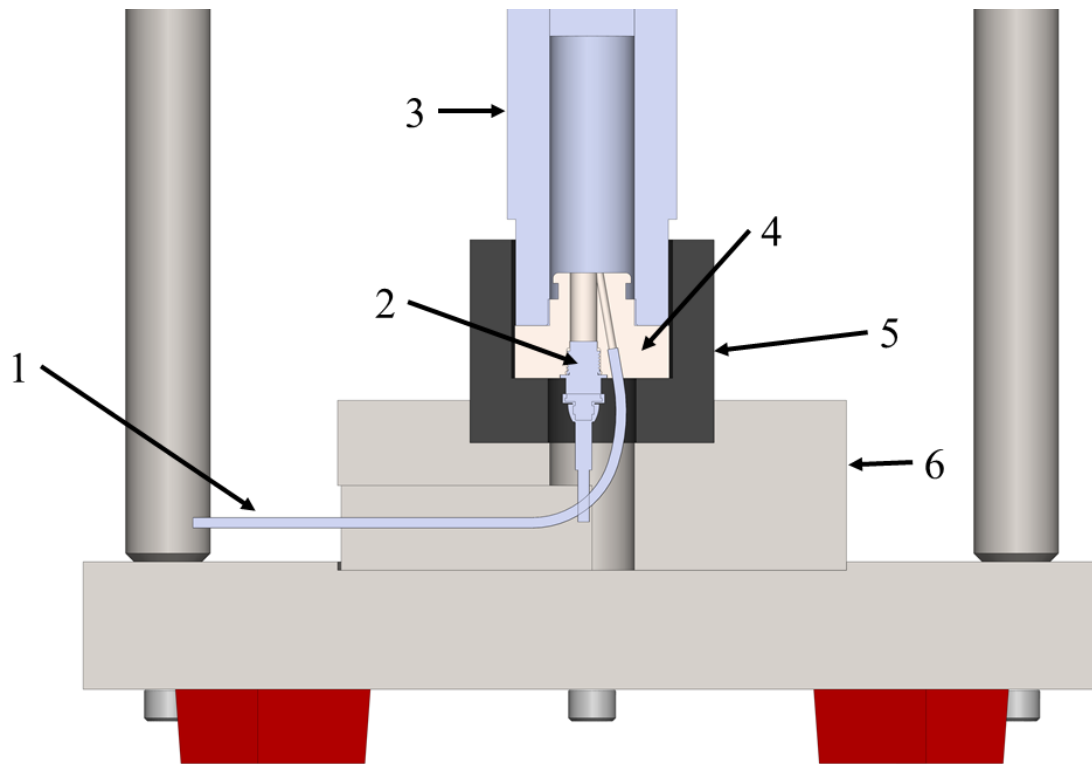
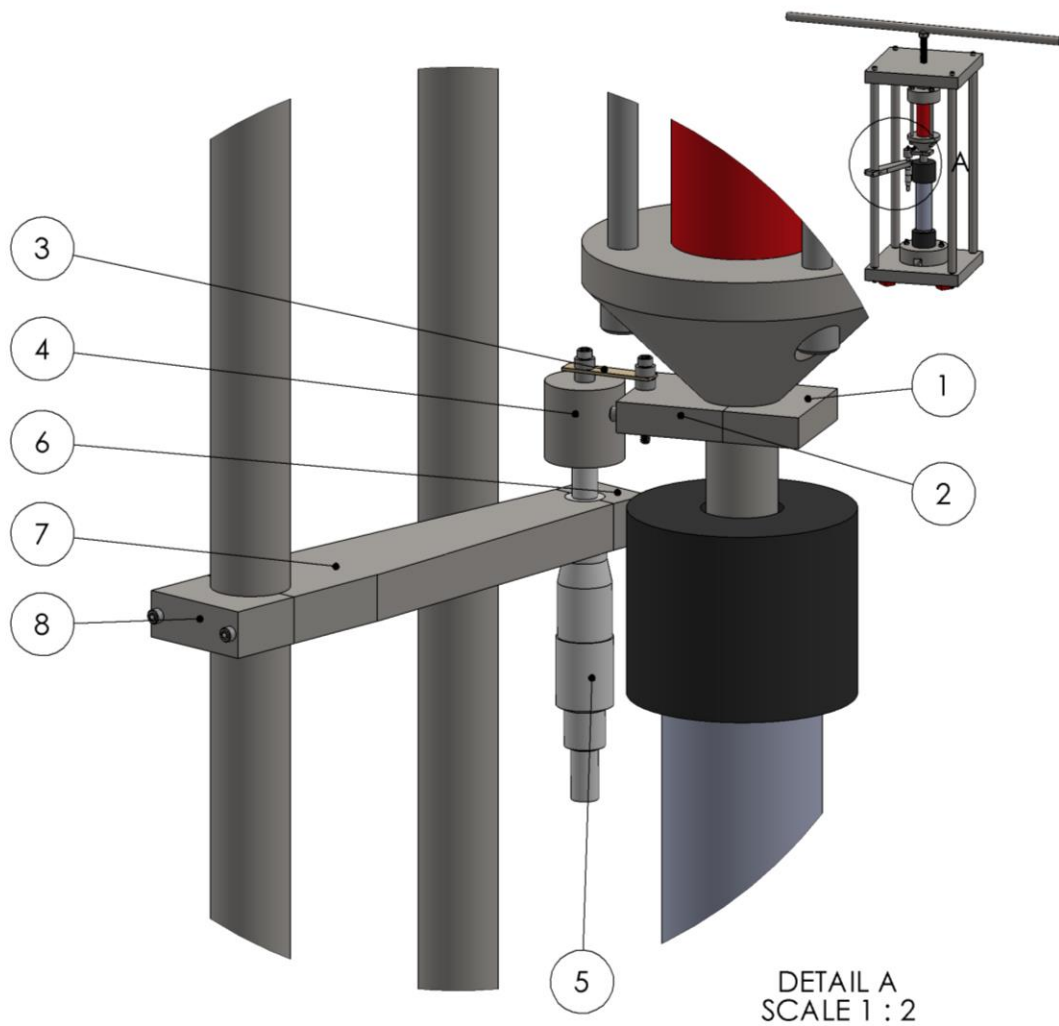


Figure 3.8: Section view of the bottom half of the machine. The pipe (#1) is used to bring fluid into and out of the pressure vessel. The pipe is welded into the vessel cover (#4). The pressure sensor (#2) screws into the vessel cover. The pressure vessel (#3) is screwed into the vessel cap (#5) to secure the vessel cover. The vessel cap sits on the vessel base (#6) with the pipe sticking out of the slot of vessel base.

The “piston rod” is a cylindrical rod that sits in contact with the piston inside the vessel and is attached to the “piston top” via a dowel pin. The bottom side of the “piston rod” has a polished finish to ensure an even contact with the piston. The “piston top” part is used to hold the piezoelectric motor. It has a circular divot where the piezoelectric motor sits. Three holes are drilled into the “piston top” that are used for bolts to hold down the piezoelectric motor in place. The “swivel block bottom” part sits on top of the

piezoelectric motor and has two purposes. The first is to hold the piezoelectric motor in place by being bolted down with the “piston top” part. The second function of this part is to make sure every part is perfectly vertical and aligned. This is achieved via a small ball bearing that sits on the top side of the part. The “swivel block top” part also has a small spherical indent in it to hold the other side of the ball bearing. The other side of the “swivel block top” part holds the middle screw. The “top plate” sits on top of the frame and is a rectangular block that is 1.5 inches thick. The “top plate” has four holes in the corners for the bolts to attach to the other end of the support rods. There is also one threaded hole through middle of the plate, which is where the middle screw goes through.

Five small pieces which are collectively named lips 1 through 5 are made to hold a micrometer and the displacement sensor during the experiment. Lips 1 and 2 are attached to the piston rod, and lip 2 holds one end of the displacement sensor. Lips 4 and 5 attach to one of the support rods. The other end of lip 4 and lip 3 attach to hold a micrometer. The “cap” part sits directly in top of the micrometer and the other end of the displacement sensor attaches to the top of the “cap”. Figure 3.9 gives a close-up view of the displacement sensor setup.



ITEM NO.	PART NUMBER	QTY.
1	Lip 1	1
2	Lip 2	1
3	Displacement Sensor	1
4	Cap	1
5	Micrometer	1
6	Lip 3	1
7	Lip 4	1
8	Lip 5	1

Figure 3.9: Detail view of machine showing displacement sensor and lip pieces.

The middle screw is used to control the amount of fluid in the pressure vessel. A handle is welded to the screw to easily turn the screw. The last custom-made part is the vessel cover, and it sits partially inside the bottom side of the pressure vessel.

Three of the parts we used for the experiment were obtained from McMaster Carr. They are the bumpers, support rods, and the ball bearing. The bumpers screw into the “bottom plate” and are used to elevate the machine off the table. The support rods are used to hold the “top plate” up and to provide the support needed for the compression during the experiment. Four rods were used, one in each corner of the top and bottom plates. Each rod is two feet long and one inch in diameter. The ball bearing is used to enable a swiveling motion of the parts so that they can all be perfectly aligned and vertical. A hardened 440C stainless steel ball was used to make sure it would be able to withstand the forces generated during the experiment.

The pressure vessel used was purchased from “High Pressure Equipment Company”. The pressure vessel is used to hold the test fluid and to provide a high-pressure seal during the experiment. The vessel used was a Tubular Series Reactor with an inner diameter of 1 inch and an outer diameter of 2 inches with a piston included. The pressure vessel is 7.75 inches long and is rated to withstand pressure of up to 10,000 psi. The piston came with the vessel, and it sits inside the vessel and is put in direct contact with the test fluid. Two vessel caps came with the vessel, and these pieces screw onto the ends of the pressure vessel to help create a tight seal. The design of the “vessel cover” part used in the experiment is a modified version of the one that comes with pressure vessel. The “vessel cover” covers one side of the vessel to seal it. The design of the “vessel cover” included a threaded hole for the pressure sensor and a hole for a pipe.

3.5 DESCRIPTION OF ELECTRONIC PARTS

Few electronics parts are used to measure the pressure and the sample strain, condition the signals from the sensors, and generate the sinusoidal pressure. Figure 3.10 shows a complete schematic of all the electronic parts. A pressure transducer was used to measure the pressure of the fluid. A thin-beam load cell was used to measure the strain of the fluid sample. Two printed circuit boards were used to supply the correct voltage to the sensors and to amplify the output signal from the pressure sensor and the displacement sensor. A power supplier was used to power the two printed circuit boards. A multifunction I/O device was used to convert the measured analog signal to a digital signal that was then sent to a computer. The multifunction I/O device was also used to convert the sinusoidal digital signal generated from the computer to an analog signal. This signal was then sent to the amplifier (PI E-481) which controlled the piezoelectric motor. More detail is given about each component below.

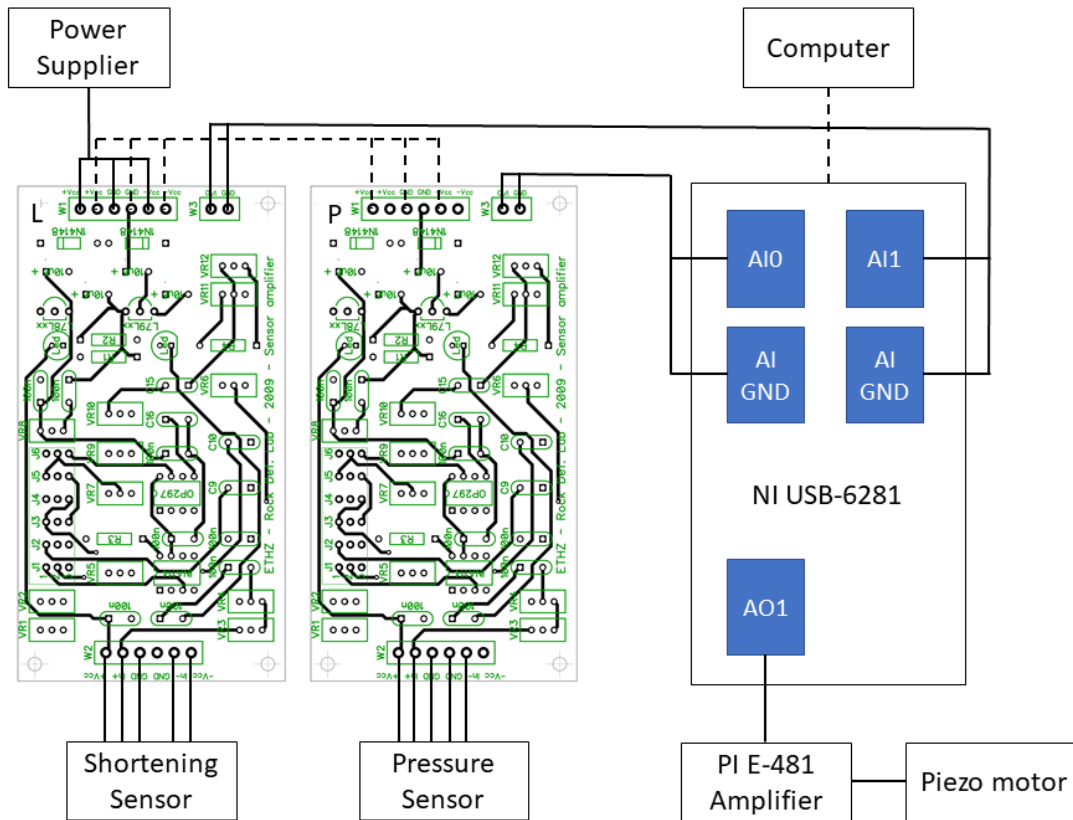


Figure 3.10: Schematic of the electronics used in the experiment. A power supplier is connected to the amplifiers (L and P for load cell and pressure sensor) which power the load cell and pressure sensor. The signal generated from the load cell and pressure sensor is amplified and sent to the A/D converter (NI USB-6281). A computer is connected to the A/D converter to record the measurements. An analog output is sent to an amplifier which is then sent to the piezoelectric motor to make the motor expand and contract for the experiment.

3.5.1 Piezoelectric Motor

A piezoelectric motor was used to create the sinusoidal pressure during the experiment by sinusoidally compressing the fluid. Piezoelectric materials are materials that deform when electrically charged. A piezoelectric motor will expand and contract at a controllable distance when a voltage is applied to it. The motor used was a Physik

Instrumente (PI) P-045.80P PICA Power Piezo Actuator. This actuator has a blocking force of 44,000 N and has a maximum displacement of 120 micrometers. A PI E-481 amplifier powered the motor.

3.5.2 Pressure Sensor

A FUTEK Miniature Pressure Sensor – Flush Mount Diaphragm (model #PFT510) measured the pressure of the fluid during the experiment. This pressure sensor can measure a maximum pressure of 10,000 psi. The sensor attaches to the bottom of the pressure vessel.

3.5.3 Shortening Sensor

To measure the shortening of the sample during the experiment, an Omega Engineering Full Bridge Thin Beam Load Cell was used (model #LCL-227G). The output voltage from the sensor changes when the sensor bends. Thus, the sensor can be calibrated to measure distances. One end attaches to the lip pieces and remains fixed while the other attaches to the piston and moves up and down with the piston. To measure the displacement sensor was properly zeroed and aligned before the experiment began, a micrometer was used to move one end of the displacement sensor up or down.

3.5.4 A/D and D/A converter

A National Instruments (NI) Multifunction I/O Device (USB-6281) was used to digitize the analog signal taken from the pressure and shortening sensor. It was also used to send an analog signal to the piezoelectric motor amplifier. This converter has an analog to digital converter with resolution of 18 bits.

3.5.5 PCB Boards

A printed circuit board (PCB) powers and conditions the signals recorded by each of the sensors. A schematic of the board is given in Appendix A. The boards amplify the low-frequency signals using an operational amplifier (INA 114) and filter the data with a 2-pole Sallen-Key low-pass filter with corner frequency of 10 kHz. The boards are powered by an Apevia ATX-CT520W Captain 520W Power Supplier. The output from sensors is connected from the PCBs to the NI board.

3.6 DESCRIPTION OF AIR EVACUATION PARTS AND SCHEMATIC

The removal of any air in the pressure vessel is critical before filling it with the fluid for testing. This process ensures that when the experiment is conducted, the measurements are for the fluid and not a combination of the fluid and air. Any air in the system would affect the results by showing a smaller bulk modulus and a higher attenuation value. A schematic showing how air is removed from the pressure vessel and how fluid is pumped into the pressure vessel is shown in figure 3.11.

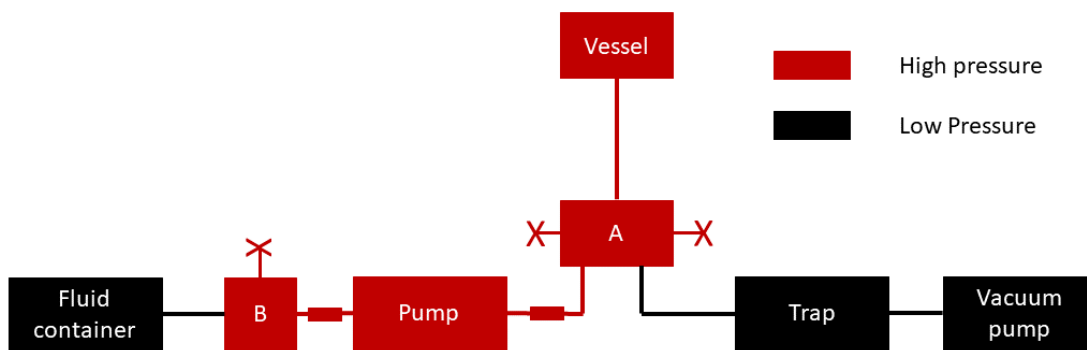


Figure 3.11: Schematic of the setup used to evacuate the pressure vessel of air and to fill it with the fluid to be tested. First the valve connecting to the vacuum is opened, and the air is removed using the vacuum. The valve is then closed and the valve connecting to the fluid container is opened. The fluid pump is then used to pump the fluid from the container into the pressure vessel. Once the pressure vessel is filled, the valve to the fluid container is closed.

To draw the air out of the pressure vessel, a Kozyard TA350 Single Stage Vacuum Pump was used. An Ablaze Mini 3 Quart Vacuum Chamber was used as a vacuum trap to ensure no fluids unintentionally get sucked into the vacuum pump. A Teledyne ISCO D-Series Model 260HP fluid pump was used to pump the test fluid into the pressure vessel. An Autoclave Engineers 3-way/ 2-stem manifold valve, that is rated for 15,000 psi, controlled the flow of air and the fluid. An Autoclave Engineers rupture disc rated to rupture at 11,494 psi prevented the pressure vessel from blowing out. High pressure rated metal tubing was used for the connections where the fluid is under high pressure. A vinyl plastic hose was used for the connections involving the removal of air and unpressurized fluid.

The setup works by connecting the pressure vessel, fluid pump, and a vacuum to the 3-way/ 2-stem manifold valve. Each stem controls a single valve. The fluid pump and vacuum pump are each connected to one of the valves that can be opened and closed. On one of those valves a vinyl plastic tube is connected to the vacuum trap. The vacuum trap

is connected to the vacuum pump. The other valve that can be opened or closed has a high-pressure metal pipe that is connected to the fluid pump. The other end of the pump is connected to a 2-way valve. The other valve on the 2-way valve is connected to a plastic container holding the fluid that is being tested via a vinyl plastic tube. The final valve on the 3-way valve is connected to the pressure vessel.

The operation procedure for evacuating the pressure vessel and filling it with fluid is as follows. First the valve connected to the fluid container is opened. The fluid pump then fills the vinyl hose with fluid up until it reaches the pump. The pump is then stopped, and the valve is closed. The other two valves are then opened. The vacuum pump is then turned on. The fluid pump then pumps out any fluid in it until the pump is empty. This removes the air from the pressure vessel, piping, and the fluid pump. The vacuum trap contains a built-in monometer which can be used to tell when the system has been fully evacuated. Once the system has been fully evacuated, the valve connecting the pressure vessel and the fluid pump is closed. The valve to the fluid container is opened and the fluid pump is filled. This valve is then closed. Next, the vacuum pump is turned off. The valve connecting the fluid pump and pressure vessel is then opened. The fluid pump then pumps fluid into the rest of the system. Once the fluid moves past the last valve, the fluid pump is stopped. The valve connected to the vacuum is closed. The volume reading on the fluid pump is then recorded and is used to estimate how much volume of fluid will go into the pressure vessel during the experiment. The fluid pump is then turned on and continues to pump fluid until the desired pressure is achieved. The fluid pump is then stopped, and the valve connected to the fluid pump is then closed. The volume reading on the fluid pump is recorded again, and the difference between the first reading and the second reading is how much fluid is in the pressure vessel.

3.7 CALIBRATION OF SENSORS

Calibration is necessary to make sure that the output voltage from the sensors is representative of what is being measured. For the calibration process a linear relation between the output voltage and the measured parameter was used. The slope and the intercept of the calibration curve were determined for each sensor and used to convert the output voltages to the physical parameter that was being measured. The slope and intercept for the curves were recorded and saved, and they are used in the MATLAB script which runs the experiment.

The pressure sensor was calibrated to give the same pressure as the output reading of the fluid pump. The fluid pump gives the pressure of the fluid in contact with it. The fluid pump was used to pressurize the fluid and the output voltage of the pressure sensor was recorded along with the pressure reading on the fluid pump. Calibration measurements were taken at pressures from 0 to 60 MPa at 10 MPa intervals.

The displacement sensor is a cantilever style load cell and was calibrated by using a micrometer. One end of the displacement sensor was mounted to the end of a micrometer whereas the other end was attached to the piston in the pressure vessel. The micrometer used has a resolution of 0.001 inches (25.4 micrometers). To calibrate the sensor the output voltage was measured at increments of 0.001 inches according to the micrometer. A least squares line was fit to the cross plot of output voltage and displacement. The intercept of the least squares line was set to zero to ensure that an output reading of 0 volts corresponds to the sensor at rest.

The PCB boards used to amplify the output signal from the pressure sensor and displacement sensor use a Sallen-Key low-pass filter to amplify low frequencies. It is critical to ensure that the filters on each amplifier do not introduce a phase delay because the results from the experiment depend upon the phase between the two measured

signals. To measure the phase between the two amplifiers a digital sinusoidal signal was sent from the computer and converted to an analog signal. The signal was then split into a second signal. This resulted in two identical signals. They were then each sent to a PCB board. The amplified signals were then converted to a digital signal and sent to the computer. The results of the phase between the two signals is shown in figure 3.12. The results show that the phase between the two PCB boards is 0, so any phase delay measured from the experiment can confidently be attributed to something other than the PCB boards.

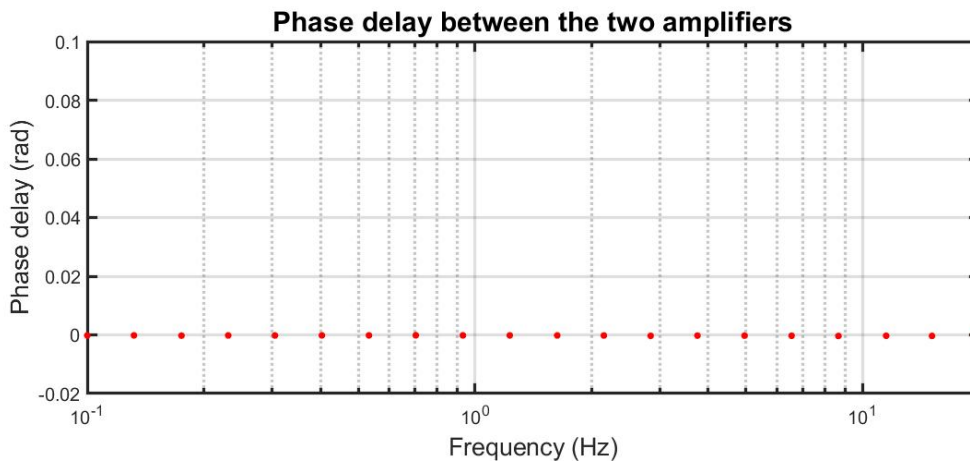


Figure 3.12: Phase delay between the amplifiers used to power the sensors in the experiment. Results show a phase delay of 0 so any phase delay measured during the experiment can confidently be attributed to material that is being tested.

3.8 EXPERIMENTAL SETUP PROCEDURE

The assembly process begins by screwing the bumpers into the bottom plate. Next the support rods and vessel base are screwed into the bottom plate. A level was used to make sure the plate was level. The bumpers can be tightened or loosened to raise or lower

part of the bottom plate. Next the top plate is lifted on top of the support rods and is screwed into the support rods.

The next step is to prepare the vessel. First the vessel cover is placed inside the pressure vessel. The vessel cap is then fed over the pipe sticking out of the vessel cover, and the vessel cap is then screwed onto vessel. Next the pressure sensor is screwed into the vessel cover. This combination of parts is then put into the vessel base such that the pipe from the vessel cover and the wire connected to the pressure sensor are sticking out of the slot on the bottom of the vessel base. The other vessel cap is screwed onto the other side of the vessel.

Next the piezoelectric motor is placed between the piston top and the swivel block bottom parts. The motor is placed so that it fits in the slot on both parts. Three screws are then inserted through the piston top and through the swivel block bottom part and bolted tight to make sure the piezo motor is secure between the two parts.

After the piezoelectric motor is ready, a dowel pin is inserted into the piston to ensure axial alignment between the parts. The piston is then placed into the pressure vessel from the top. Fluid is then pumped into the vessel which raises the piston. The piston rod is then inserted into the pressure vessel and fits on the other side of the dowel pin on the piston. Another dowel pin is inserted on the other end of the middle rod. The slot on the bottom of the piston top is inserted on the dowel pin. A ball bearing is then placed in the groove on top of the swivel block bottom part and the swivel block top part is then placed on the other end of the ball bearing. Next the middle screw is screwed into the top plate such that it goes through the plate and into the swivel block top piece. A screw is then used to fasten the swivel block top piece to the middle screw.

Next the series of lip pieces are connected. First lips 1 and 2 are connected over the piston rod. Lips 4 and 5 are connected over one of the support rods. Lips 3 and 4 are

connected with the micrometer between them. The cap piece is then placed on top of the head of the micrometer. A screw is placed into the side of the cap piece and tightened until the cap piece is secured to the micrometer. The series of lip pieces 3,4, and 5 are then raised and lowered until the top of the cap piece is at about the same height as lip pieces 4 and 5. The lip pieces are also rotated so that lip 2 is close to the cap piece.

Spacers are then put on the threaded hole on the top of the cap piece and on the hole in lip 2. The displacement sensor is then placed to line up with the spacers. Two more spacers are then placed on top of the displacement sensor, and a screw is screwed into the cap piece and lip 2. The micrometer can be turned to raise or lower the cap piece more precisely if needed. This completes the assembly of the frame. Figure 3.13 shows a picture of the all the components of the experiment with labels.

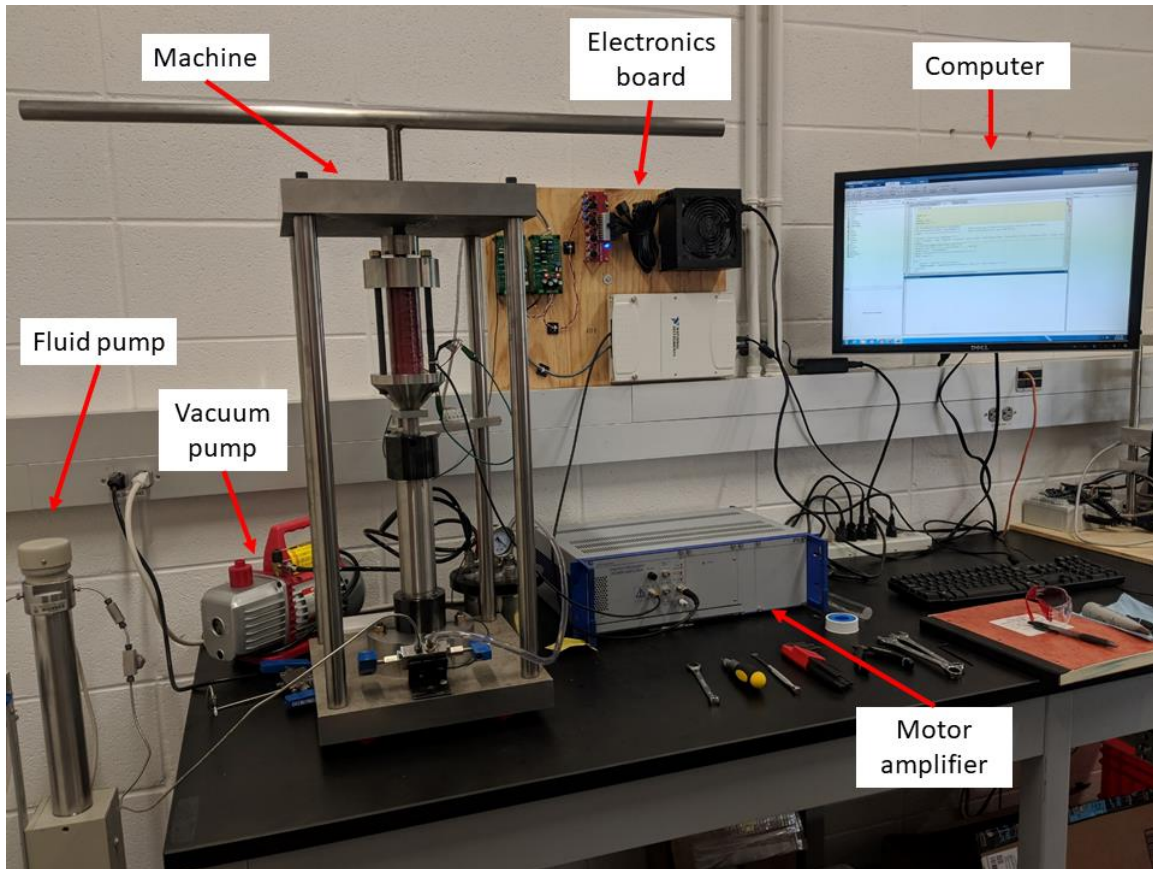


Figure 3.13 Picture of the machine and all the components used during the experiment. All parts are labelled. The fluid pump is connected to a three-way valve that is connected to the bottom of the machine. A vacuum pump is connected to the same valve. The vacuum pump is used to draw out any air in the system before the fluid pump is used to fill the and pressurize the pressure vessel in the machine. The electronics board contains the power supplier, two amplifiers used with the sensors, and the multifunction board. Another amplifier powers the piezoelectric motor in the machine. On the right side is the computer that is used to run the experiment and save the data that is recorded.

3.9 DESCRIPTION OF CODES

The experiment is run by a MATLAB script. The script allows the user to specify the parameters of the sample and the experiment. The sample parameters include the

sample material and the diameter of the sample. The experiment parameters include the range of frequencies tested, the number of frequencies in that range, the voltage sent to the amplifier that is then sent to the motor, the number of cycles for each frequency, the number of stacks at each frequency, the moving average window size that is applied to the measured pressure and displacement signals, and the number of repetitions, which is the amount of times the range of frequencies are repeated.

The code works by first prompting the user for a file containing the test parameters, a file containing the experiment parameters, and the volume of fluid inside the pressure vessel. The script then generates a sinusoidal signal containing a specified number of oscillations at the specified highest frequency. The signal is then sent to the digital to analog converter which is then amplified and sent to the piezoelectric motor.

The signal measured from each sensor is recorded and saved. The script then scales the signals according to the calibration coefficients that were determined during the calibration process. The signals are then cut up into the specified number of groups, and the signals are stacked to reduce noise. The stacked signals are then smoothed by a moving average with a specified window size. Figure 3.14 shows a flow chart of the code used to run the experiment.

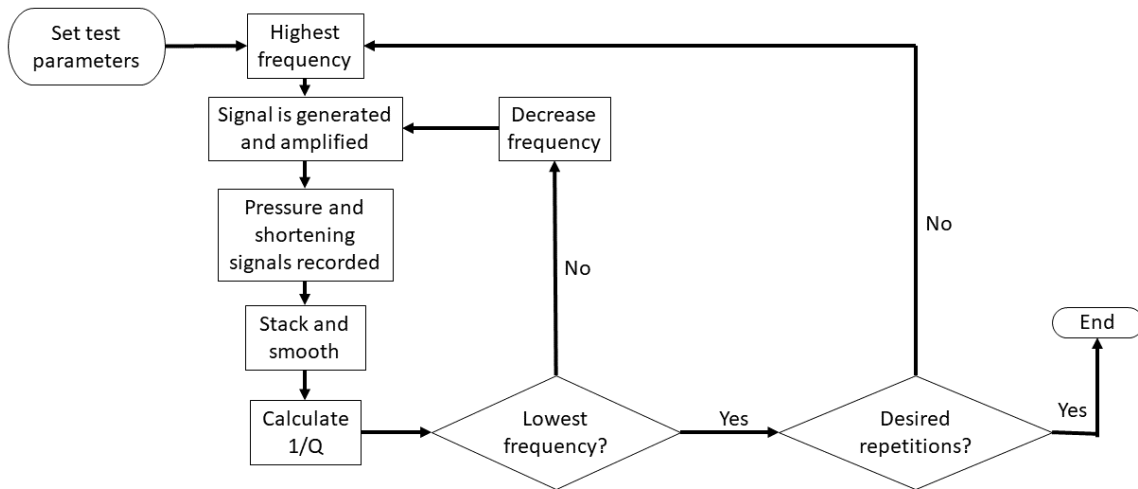


Figure 3.14: Flow chart showing how the MATLAB script that is used to run the experiment works. The script first reads and sets the test parameters. The highest frequency is first selected. The sinusoidal signal is generated and the pressure and shortening signals are recorded, stacked, and smoothed. Attenuation is then calculated from these signals. The next lowest frequency is then tested. Once the lowest frequency is tested the highest frequency is tested next until the number of desired repetitions is achieved.

The bulk modulus is then calculated from the magnitude of pressure variation, the volumetric strain, and the phase delay between pressure and shortening as given in equation 3.4. Volumetric strain is calculated from the initial volume of fluid in the pressure vessel and from an estimate on the compressed volume of fluid. The compressed volume of fluid is estimated by assuming the height of the cylinder of fluid has been compressed by the amount of the measured shortening of the sample and by assuming there is no lateral expansion of the fluid sample.

The $1/Q$ value is calculated in three ways. The first method calculates the area between the loading and unloading path of the sample. The second method uses the discrete Fourier transform. The fast Fourier transform is computed for the pressure signal and the shortening signal. The phase difference between the signals at the frequency that

the sample was measured is then calculated. I/Q is then calculated from equation 2.6. The third method calculated the phase between the two signals using the phase function and calculates I/Q from equation 2.6. The purpose of the other two methods is to ensure the value being measured is reliable by making sure all three methods produce similar I/Q values (Tisato and Madonna, 2012).

The first frequency tested is always the highest frequency. The MATLAB script will calculate I/Q and the bulk modulus at that frequency and save the data. Then the script will move to the next highest frequency and run another test at that frequency. Once complete it moves down to the next highest frequency and so on. After the lowest frequency is tested, the experiment will then go back to the highest frequency and repeat the measurements at each frequency according to the specified number of repetitions. After all repetitions are complete the experiment is over.

3.10 TESTS ON SOLIDS

Before tests were conducted on fluids the machine was used to measure attenuation on solid rods of 6061 aluminum alloy and acrylic. The values of attenuation of these materials are well known and were used to make sure the machine was working properly. Figure 3.15 shows the setup for measuring the attenuation of a solid using the machine.

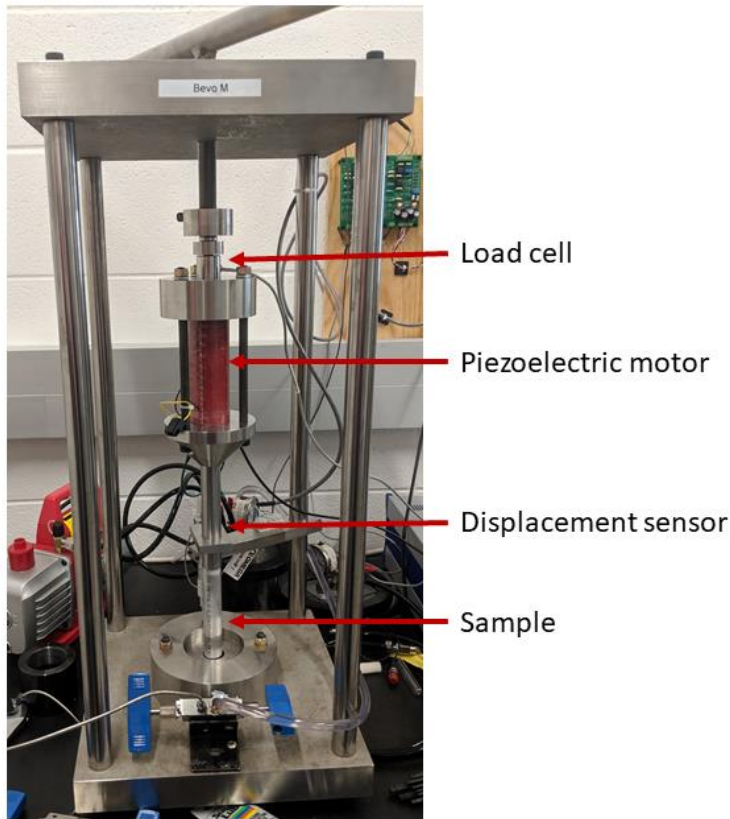


Figure 3.15: Experimental setup of tests done on solid samples. This image shows a test of an aluminum rod. The aluminum rod sits on the bottom of the frame and a stainless-steel bar sits on top of it. The stainless-steel bar has the displacement sensor attached to it. Above the stainless-steel bar is the piezoelectric motor. Above the motor is a compression load cell that is used to measure the strain of the sample.

A compression load cell, instead of the pressure sensor, was used to measure the stress applied to the material during the experiment. The same displacement sensor was used for the tests on solids and fluids. The cylindrical sample sat on the bottom of the frame and the load cell sat on top of the sample. The piston was not used for these measurements. The middle rod was placed on top of the load cell and the piezoelectric

motor was placed on top of the middle rod. The same experimental methodology and MATLAB script was used to for the solid samples.

6000 series aluminum alloys typically have Q values of about 1000 (Tisato and Madonna, 2012) and acrylic typically has a maximum of 0.07 at 3 Hz (Lakes, 2009). Results of the attenuation measurements of 6061 aluminum alloy and acrylic are given in figure 3.16. Measurements were taken 5 times at each frequency to show the repeatability for the measurements. The values from our machine are in good agreement with values cited in the literature. This ensures that the machine is working properly, and our methodology can be used to measure the properties of fluids.

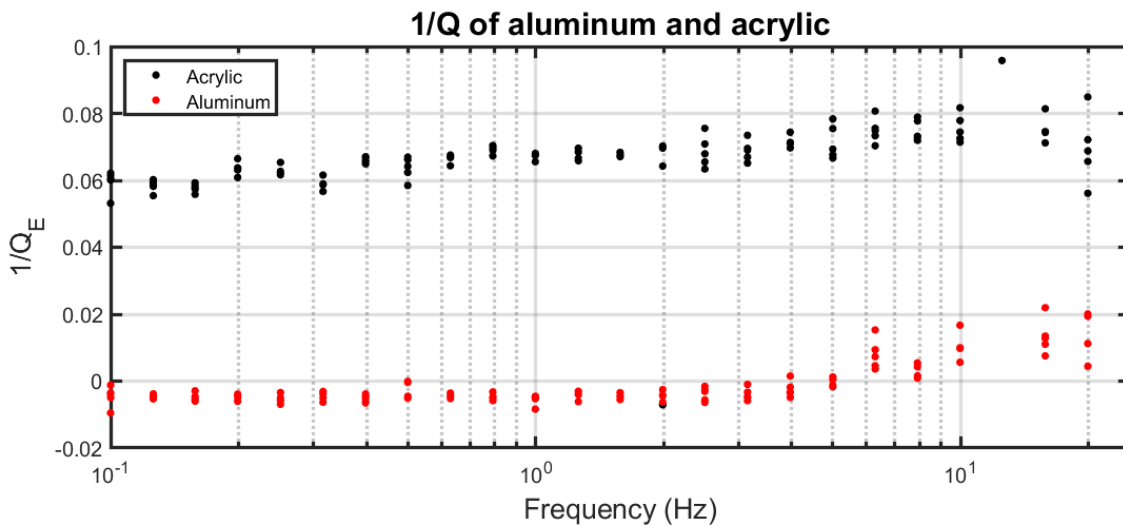


Figure 3.16: Measured $1/Q$ values of a rod of acrylic and a rod of aluminum. Results for aluminum show very low attenuation values, and results for acrylic show a maximum attenuation of $Q^{-1} \approx 0.07$.

3.11 LIMITATIONS OF THE MACHINE

From figure 3.16 it is clear that results above 5 Hz show that $1/Q$ begin to deviate away from the results at lower frequencies. Tests above 5 Hz have been conducted on

water, but the results are unreliable as well at those frequencies. For instance, figure 3.17 shows the results of attenuation measurements on water tested at 40 MPa from 20 to 0.1 Hz. One hundred frequencies were tested in this range to see if any small range of frequencies consistently produce bad results. The results are generally too high at frequencies above 5 Hz. Because of this, tests on fluids were and will be conducted at frequencies below 5 Hz.

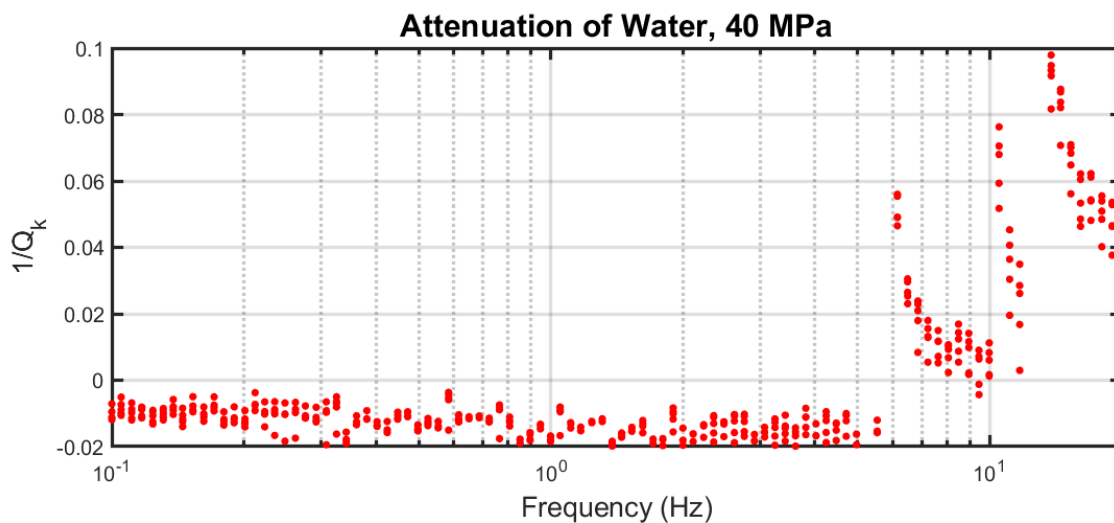


Figure 3.17: Results of a test on water from 0.1 to 20 Hz. Results show that the machine is unreliable at frequencies above 5 Hz.

The bad results are believed to be due to either resonance of the frame of the machine, or from resonance of the fluid in the pipe connected to the pressure vessel. This may be fixed by changing the length of the support rods and using stiffer materials or by changing the length of the pipe connected to the pressure vessel.

The $1/Q$ values measured for 6061 aluminum alloy are scattered around zero and are larger than the values reported in the literature. This is believed to be caused by the machine not being accurate enough to measure $1/Q$ values below 0.005. The accuracy of

the machine could be improved by using stiffer materials in the frame of the machine. This however is not certain since the compressibility of the entire system is dominated by the relatively high compressibility of the sample. The exact I/Q values the machine measures for values less than 0.005 should not be trusted. Values less than 0.005 at different frequencies should also not be compared. Instead they should be interpreted as having a Q value higher than 200. The machine produces results that are more accurate with materials that have higher attenuations ($I/Q > 0.005$) as seen in the results for acrylic.

3.12 EXPERIMENTAL OPERATION PROCEDURE

Once the pressure vessel has been evacuated with air, filled with the fluid to be tested, and the electronics are set up and ready to use, the fluid pump is used to bring the fluid up to the desired initial pressure. The valve connected to the fluid pump is then closed. The machine is now ready to begin an experiment. The MATLAB script is then run. The experiment takes several hours to run depending on the frequencies tested and the number of repetitions desired. The experimental parameters we used for our experiments on fluids took about 9 hours to complete an experiment.

To disassemble the machine after an experiment has completed, the fluid pump is first used to depressurize the fluid. Then the displacement sensor is removed. The fluid pump then fills up and removes the fluid from the pressure vessel. Then the fluid pump will pump the fluid back into the container it was originally in. The pressure vessel and piping were completely disassembled and cleaned after every experiment was completed.

3.13 TYPICAL STRAIN VALUES

The strain of the test fluid can be altered in two ways. The first is to change the amount of fluid that is in the pressure vessel (i.e., the length of the sample). This is done by raising and lowering the middle screw. The second method is to change the amount the piezoelectric motor expands. To do this the voltage supplied to it is altered. A higher voltage sent to the motor will cause the motor to expand more. Figure 3.18 shows the strain on the fluid for a range of typical fluid volumes and piezoelectric motor expansion in micrometers. Typical strains are on the order of 10^{-4} . Higher strains are only possible at low frequencies. This is because at high voltages and high frequencies (i.e., $>3V$ and 50 Hz) the motor amplifier does not produce enough power to expand and contract fully. Lower strains than 10^{-3} are not possible with this setup because the pressure sensor, at low strains, is not sensitive enough to distinguish between increases in pressure from the motor and background noise.

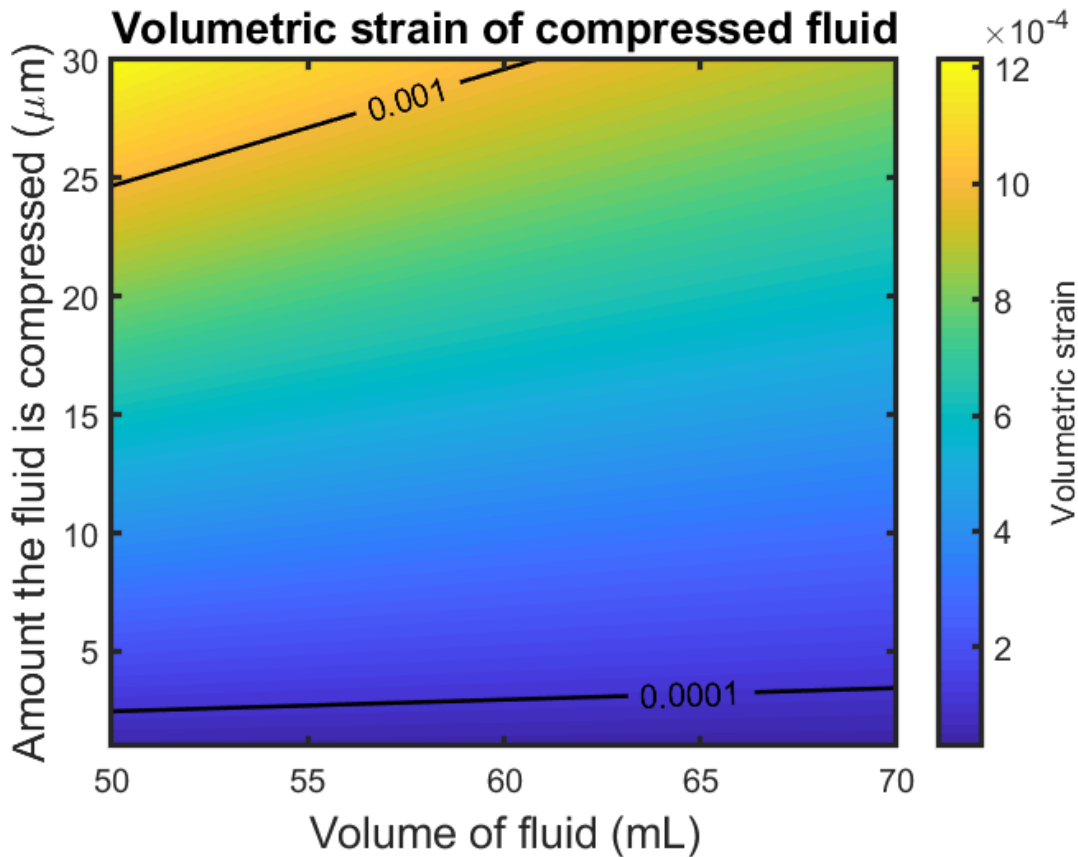


Figure 3.18: Volumetric strain of fluid during the experiment with typical values of fluid compression and fluid volume. The volumetric strain is typically on the order of 10^{-4} .

3.14 EFFECT OF TRANSIENT FLUID PRESSURE

One of the assumptions that must hold during our tests is that quasi-static condition, i.e., pressure is the same throughout the sample. However, during the experiment, the fluid is pressurized from a piston moving downward on one side of the pressure vessel. This creates a pressure gradient throughout the sample at the moment the piston moves downward. For a very short period of time (equilibration time), the pressure is greatest near the piston and decreases with distance away from the piston. This

pressure gradient could be the cause of any attenuation that is observed. This effect was documented by Pimienta et al. (2015) where they measure attenuation in fully saturated sandstones.

As a first approximation, to consider our sample under quasi-static conditions we need to make sure that the equilibration time is much smaller than the inverse of the maximum tested frequency (0.1 Hz). The pressure vessel used has a small pipe connected to it which is necessary in order to bring the fluid into and out of the vessel. Ideally, it would be best to not have a pipe connected to the pressure vessel because the long distance of the pipe only exaggerates the extent of this pressure gradient and could be the cause of any observed attenuation that is measured. This, however, is unavoidable.

To estimate the equilibration time, the diffusion of a fluid pressure impulse in the vessel and pipe was modeled with a 1D numerical simulation. The problem is modeled by combining Darcy's Law with the compressibility of a fluid and assuming an incompressible pipe wall. Darcy's Law states

$$Q_f = \frac{\kappa dP_f}{\eta dx} \quad (3.4)$$

where Q_f is the volumetric flow rate of fluid through a porous media with permeability κ , fluid viscosity η , and fluid pressure gradient $\frac{dP_f}{dx}$. The infinitesimal increase in fluid pressure in a constant volume when an infinitesimally small volume of fluid is pressed into the volume can be calculated from the definition of bulk modulus

$$dP = \frac{KdV}{V} \quad (3.5)$$

where dP is the increase in fluid pressure, K is the effective bulk modulus of the pipe and fluid, dV is the volume variation, and V is the volume of the container. Equations 3.4 and 3.5 can be combined to show

$$\frac{dP}{dt} = \frac{\kappa K}{\eta} \frac{d^2 P_f}{dx^2}. \quad (3.6)$$

This equation shows how pressure in the vessel and pipe changes as a function of time and space. The permeability of a pipe can be estimated by combining Darcy's Law with the Hagen-Poiseuille equation (Ward-Smith, 2012) to obtain

$$\kappa = \frac{r^2}{8} \quad (3.7)$$

where κ is the permeability of the pipe and r is the radius of the pipe.

The model was run to simulate the pressure gradient throughout the pressure vessel and pipe during an experimental test on a guar gum solution. It accomplishes this by perturbing the system from one end with a pressure impulse. This simulates the piston moving down and compressing the fluid from the top end of the pressure vessel. Figure 3.19 shows a schematic of the model used in the simulation. The sizes of the vessel and pipe are proportional to the one shown in the figure.

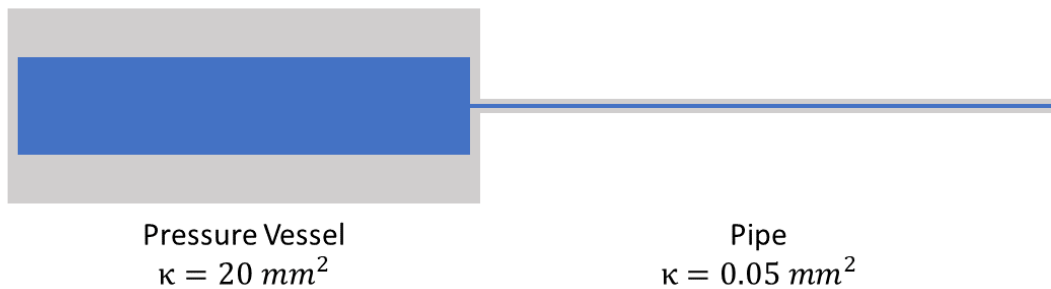


Figure 3.19: Schematic of the vessel and pipe setup used in the numerical simulation. The radius and length of the vessel and pipe shown in the figure are proportional to their actual sizes. The permeability of each is also given.

The parameters used in the numerical model are shown in table 3.1. Results of the model and the initial pressure impulse are shown in figure 3.20. The figure shows the difference in pressure between the end of the pressure vessel and the end of the pipe. The model was run to simulate 0.01 seconds with a time step of one nanosecond.

From the results, the pressure equilibrates throughout the vessel and pipe in an amount of time that is much smaller than the period at which we apply a sinusoidal pressure to the fluid. It can therefore be concluded that any measured attenuation results are not due to wave induced fluid flow but are instead due to the intrinsic attenuation of the test fluid.

Symbol	Value (unit)	Description
κ_v	20 (mm ²)	Permeability of vessel
κ_p	0.05 (mm ²)	Permeability of pipe
K_v	10 ⁹ (Pa)	Bulk modulus of vessel
K_p	10 ⁹ (Pa)	Bulk modulus of pipe
η	0.05 (Pa*s)	Viscosity of guar gum

Table 3.1: Parameters used in the numerical model.

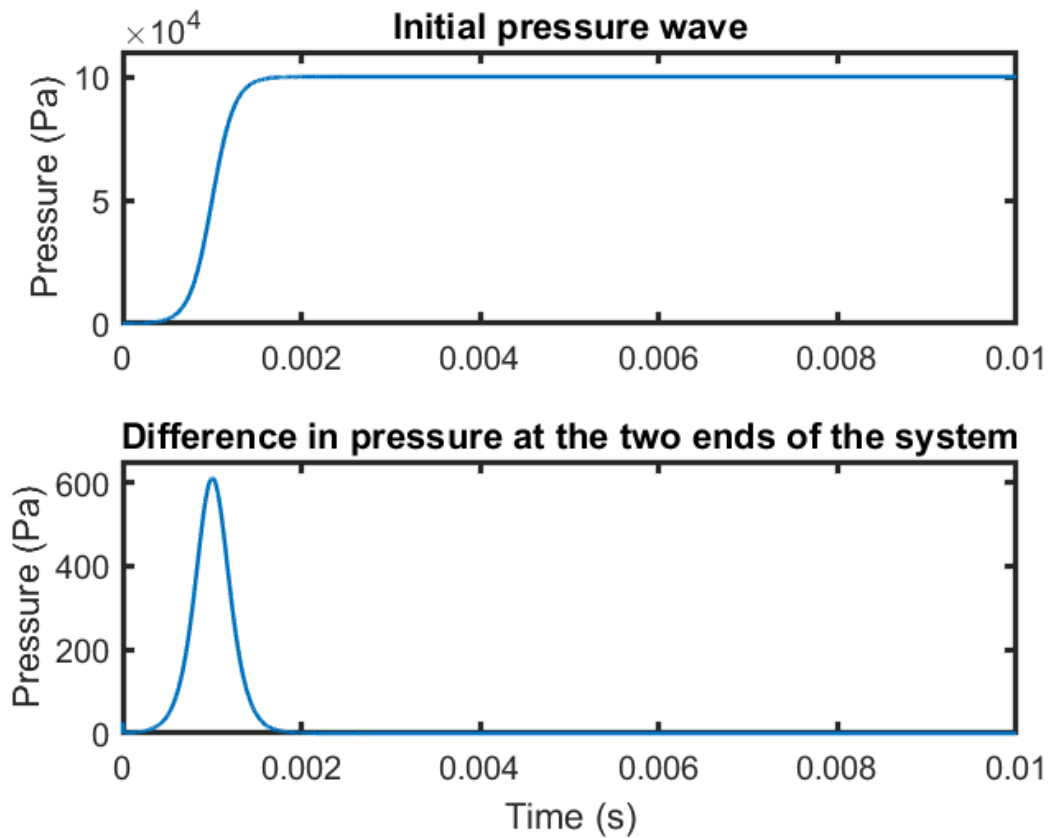


Figure 3.20: Results from the numerical simulation. The top plot shows the initial pressure wave that was forced on the end of the vessel. The bottom plot shows the pressure difference between the end of the vessel and the end of the pipe. The pressure diffuses throughout the system to 10^5 Pa in less than 0.002 seconds which is much smaller than any period that the machine operates at. Attenuation caused by wave induced fluid flow is therefore negligible.

Chapter 4: Results and Discussion

4.1 WATER RESULTS

The attenuation of water was measured at pressures of 10, 20, 30, and 40 MPa. Results are shown in figure 4.1. Results show that $1/Q$ is small and is less than 0.01. A red band is shown on each plot. This red band corresponds to $1/Q$ values of less than 0.005 thus values that fall within this red band have a Q value of greater than 200.

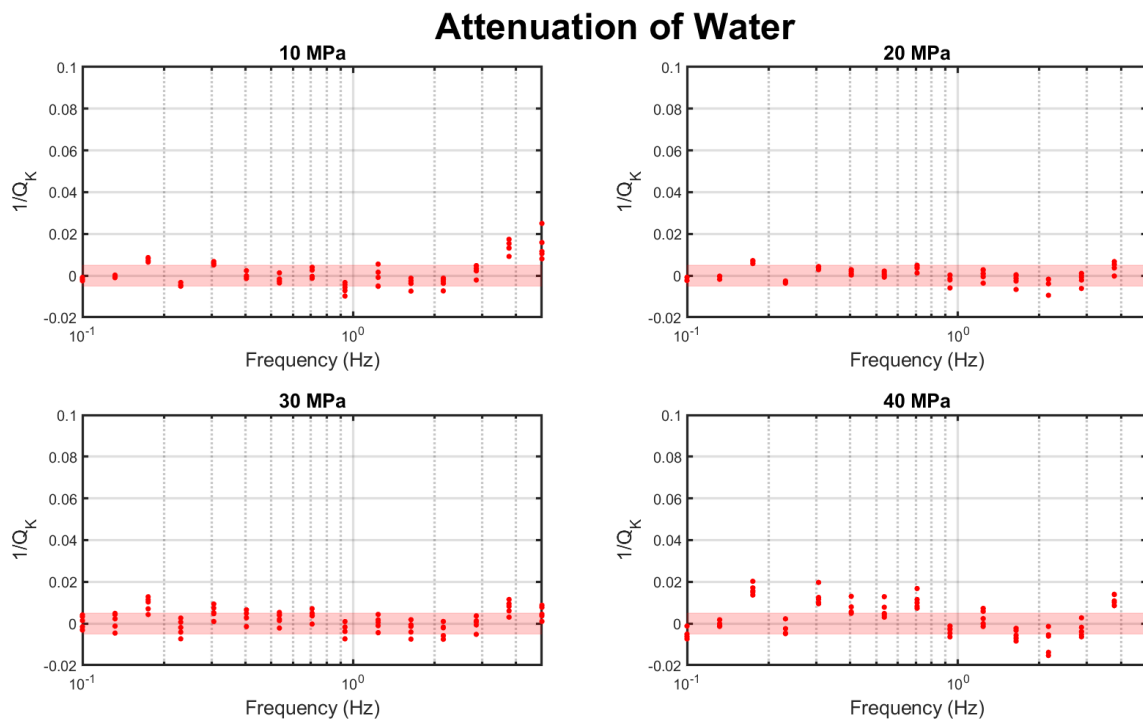


Figure 4.1: Results of attenuation measurements of water at 10, 20, 30, and 40 MPa. Results below 5 Hz generally show the attenuation coefficient is less than 0.01. The machine starts to produce unreliable results at 40 MPa.

Bulk modulus was measured for water at pressures of 5, 10, 20, 30, and 40 MPa. Bulk modulus was measured at each frequency in the range tested at each pressure. The average bulk modulus at each pressure is shown in table 4.1. Also shown are bulk

Pressure (MPa)	Measured bulk modulus (GPa)	NIST bulk modulus (GPa)
5	2.24	2.23
10	2.26	2.26
20	2.32	2.32
30	2.36	2.38
40	2.43	2.44

Table 4.1: Measured values of bulk modulus of water and reported values of bulk modulus of water from the National Institute of Standard's and Technology's (NIST) database of thermophysical properties of fluid systems at various pressures. Results from our experiments agree with those reported by NIST.

modulus values calculated from values of density and the speed of sound of water from the National Institute of Standards and Technology's (NIST) database of thermophysical properties of fluid systems (<https://webbook.nist.gov/chemistry/fluid/>). Figure 4.2 shows the NIST's results and the measured results of the bulk modulus with error bars representing the standard deviation as a function of pressure. Results show that the measured bulk modulus slightly underpredicts the true bulk modulus but is within a few percent.

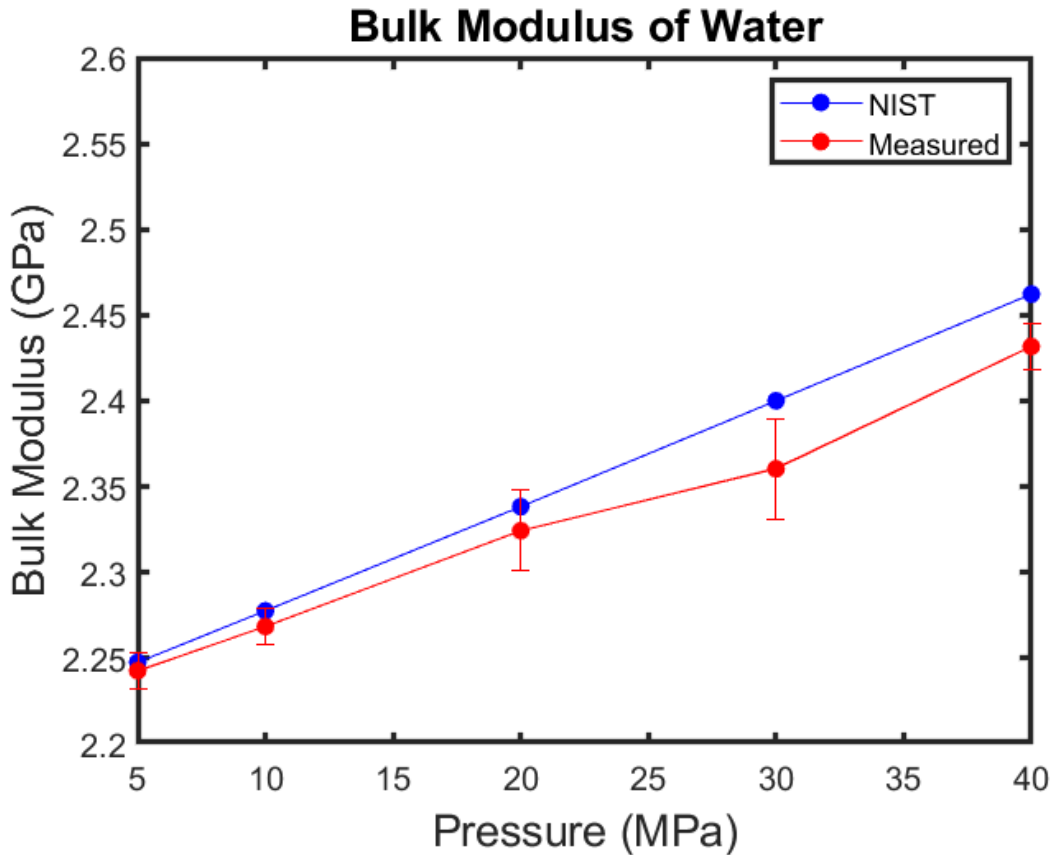


Figure 4.2: Results of measured bulk modulus of water with error bars that represent one standard deviation as plotted against pressure. Also shown are the results from the NIST’s database for water. Measured results slightly underpredict the true value but are within the bounds of the error bars.

4.2 WATER DISCUSSION

Values of I/Q of pure water are reported to be less than 10^{-3} (Liebermann, 1948; Pinkerton, 1947). These values are in the kHz to MHz region. Seismic frequency (20-200 Hz) I/Q of sea water was measured by Sheehy and Halley (1957), and they found that I/Q is on the order of 10^{-5} or less. The I/Q values measured for water are scattered around zero and are larger than the values reported in the literature. Statistically, most of

the values measured for water fall within the red band. It can, therefore, be concluded that results from the machine show that water has a Q value higher than 200.

At higher pressures the machine starts to produce unreliable results. This is seen in the 40 MPa measurements in figure 4.1. The measured I/Q values are generally too high. Further testing will need to be done with various O-ring hardnesses to fix this issue.

Comparing results for water at different pressures shows that I/Q does not change significantly with pressure. Litovitz and Crnevale (1955) show that the attenuation of water decreases with pressure. This is not present in the results because the machine is not accurate enough when measuring materials with small attenuation. The values plotted in the red bands are not exact.

Bulk modulus increases with increasing pressure as expected because the volume of the fluid decreases with increasing pressure. To check the results, the measured bulk modulus was compared to data from the National Institute of Standards and Technology's (NIST) database of thermophysical properties of fluid systems. This database contains several physical properties of many fluids. The density and speed of sound of water at each pressure from the database were used to calculate the bulk modulus of water at each pressure. Results of our measurements are in good agreement with those from NIST. The values from the NIST database are high-frequency data. Water has such a low attenuation that the values measured here in the low-frequency range should be almost identical to the high-frequency range.

4.3 GUAR GUM RESULTS

I/Q was measured for three concentrations of aqueous guar gum solutions at a pressure of 10 MPa. The guar gum samples had concentrations of 10, 20, and 40 ppt (pounds of guar gum per thousand gallons of water). Results are shown in figure 4.3. The

attenuation of guar gum is significantly higher than water and attenuation increases with increasing guar gum concentration. The average Q values for the 10, 20, and 40 ppt samples are 168, 60, and 40 respectively.

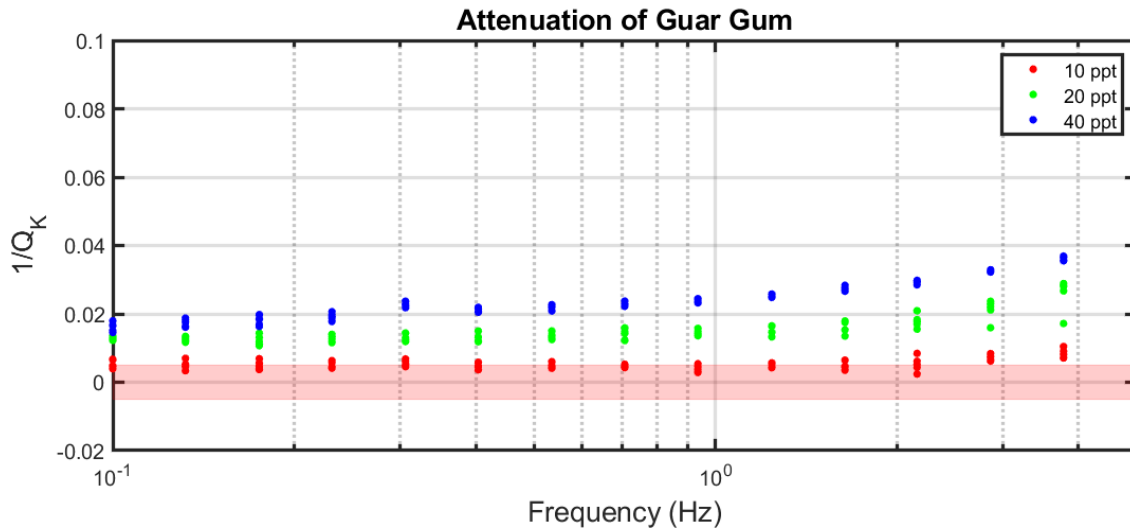


Figure 4.3: Results of $1/Q$ measurements of aqueous guar gum solutions. Results were obtained at 10 MPa for concentrations of 10, 20, and 40 ppt. Attenuation is higher than water and increases with concentration.

The bulk modulus of three concentrations of aqueous guar gum solutions were measured at pressures of 20, 30, and 40 MPa. Results are shown in figure 4.4 with error bars representing one standard deviation included. Also plotted is the bulk modulus of water at each pressure to compare to guar gum. At each concentration of guar gum the bulk modulus increases with pressure. The bulk modulus also increases with concentration at a given pressure.

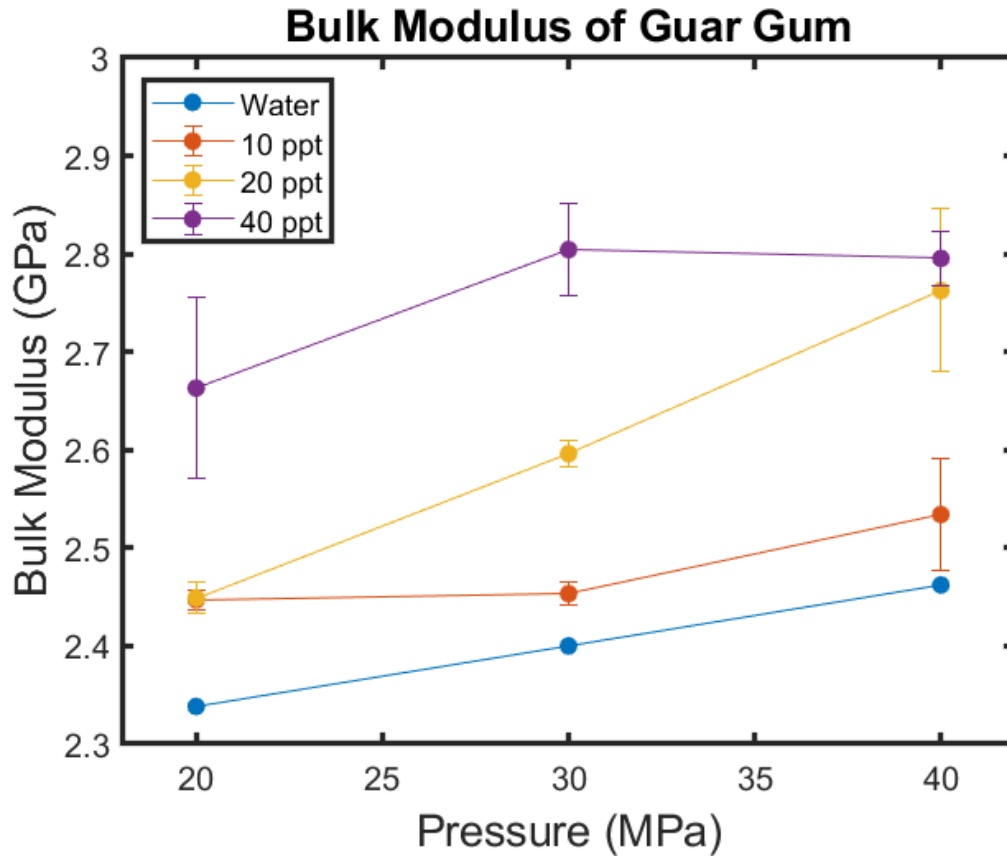


Figure 4.4: Bulk modulus of guar gum as a function of pressure and concentration. Error bars represent one standard deviation. The bulk modulus of water is also shown. Bulk modulus of guar gum increases with pressure and concentration.

4.4 GUAR GUM DISCUSSION

The attenuation of guar gum was found to increase with concentration. This result can be explained by Wientjes et al. (2000) model of low-frequency relaxation mechanisms in guar gum solutions. In their paper, the shear storage and loss moduli are measured at frequencies ranging from 10^{-4} to 10 Hz. At the frequencies in which we tested guar gum (0.1 – 5 Hz) they found a distinct storage modulus plateau. This

corresponds to a frequency range in which there is significant dispersion and attenuation. As mentioned previously, the Navier-Stokes equation states that there are two types of viscosities, namely shear and bulk. If shear attenuation increases in a specific frequency range, it is not unreasonable to assume bulk attenuation would increase as well. This idea supports that data that we measured which shows that at these frequencies there is significant attenuation and dispersion.

The physical model they propose to explain how energy is attenuated in aqueous guar gum solutions at these frequencies states that energy is lost due to the breakup of weak and strong bonds in the guar gum chain. The weak bonds are the bonds between the backbone chain and the side galactose units. The strong bonds are between mannose units along the backbone chain. When a stress is applied to the guar gum molecule chain, pressure is perturbed along the chain. The variation in pressure leads to a breakup of bonds at specific sites in the molecule. It takes energy to break these bonds, so energy is being taken from the seismic wave as it propagates and being used to break these bonds. An increase in concentration means there are more chains and bonds to break up in the sample. This means that more energy would be lost to higher concentrations and thus have a higher attenuation. This model supports the data that we measure which shows that attenuation increases with guar gum concentration. This is a possible explanation of why there is an increase in attenuation with concentration in guar gum.

The bulk modulus of guar gum was found to increase with pressure similar to water because the volume of the fluid decreases with increasing pressure. The bulk modulus was also found to increase with concentration as well. An increase in the bulk modulus of water with concentration of a solvent has been observed before (Slie et al., 1966; Osif, 1988).

Chapter 5: Conclusions and Future Work

5.1 CONCLUSIONS

A machine was designed and built to measure the low-frequency attenuation of fluids. Bulk modulus can also be calculated with the data this recorded during the experiments. The low-frequency attenuation of materials could be significantly different than the high frequency attenuation values. Methodologies to measure the high-frequency attenuation of fluids are well established and are commonly used. High-frequency attenuation values of fluids are widespread in the literature. The low-frequency (<10 Hz) attenuation values of fluids are not reported and no methodology has been previously reported. This work has significant implications in outstanding rock physics issues where the low-frequency intrinsic attenuation of fluids would be ideal to use instead of the high-frequency values.

Attenuation values of water have been previously reported in the seismic frequencies with a Q value of greater than 10,000. The results from our machine give Q of water that are higher than 200. The machine is not accurate enough to measure very high Q values. Modifications will need to be made to make the machine stiffer and able to accurately measure low attenuating fluids.

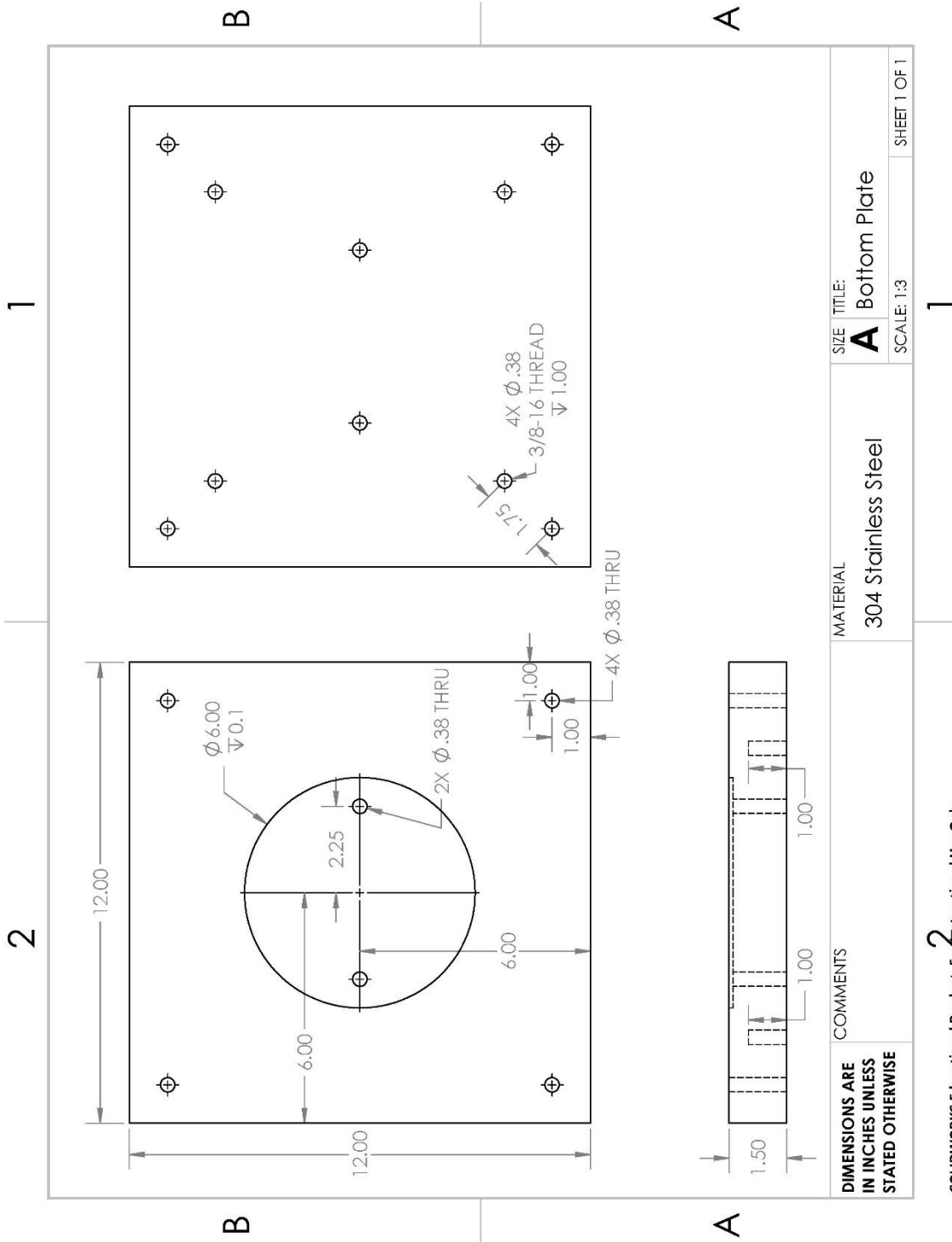
Attenuation values of aqueous guar gum solutions were found to be significantly higher than water. Attenuation also increased with increasing concentration of guar gum. This is explained by energy being lost during the breakup of weak and strong bonds in the guar gum chains. A higher concentration provides more bonds to break up which leads to more energy being lost which increases attenuation.

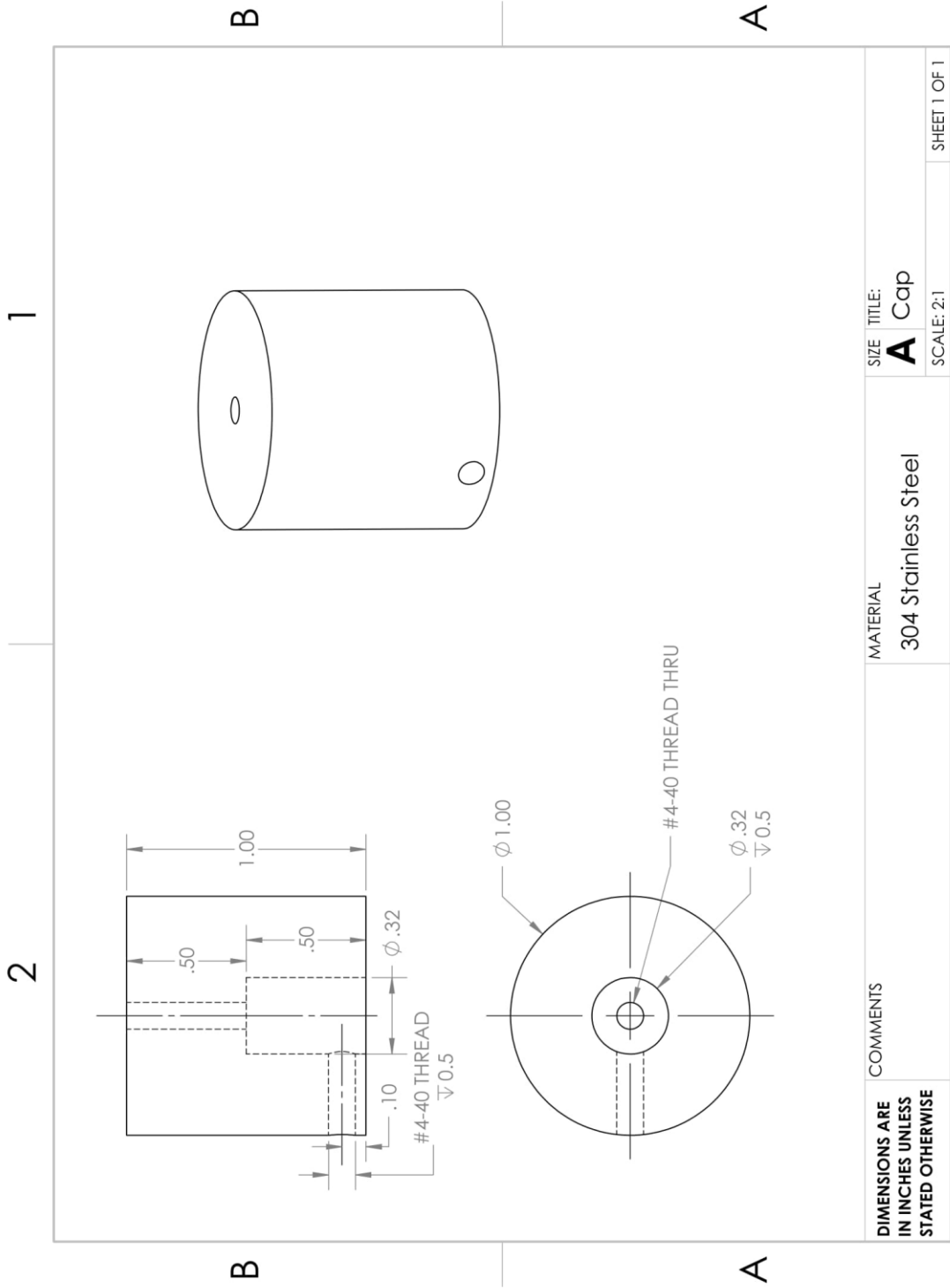
5.2 FUTURE WORK

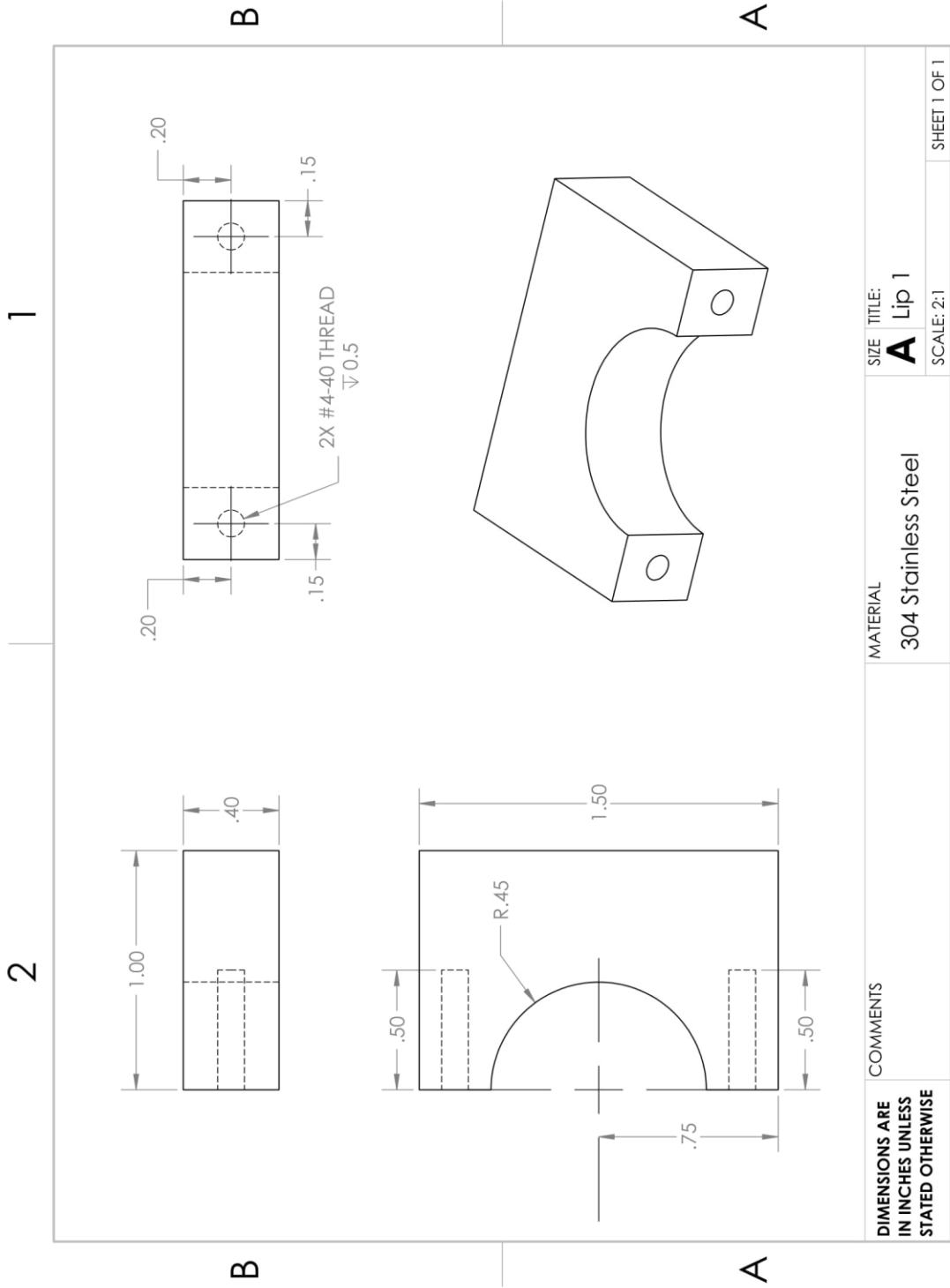
Modifications can be made to the machine to test attenuation under more conditions. For instance, the temperature of the sample in the pressure vessel could be controlled by attaching a heating or cooling element to the pressure vessel. Using a colder temperature could make the guar gum last longer before it begins to rot and decompose so longer tests could be done on guar gum. Testing at higher temperature could be used to simulate conditions in a well during hydrocarbon production.

The machine could also be used to measure the attenuation of fluids with particles in suspension such as fracking fluid with proppant in suspension. A modification would have to be made inside the pressure vessel to incorporate a stirring mechanism. This would prevent the particles in suspensions from eventually settling to the bottom of the vessel during the long duration of the experiment.

Appendix A: Part Drawings

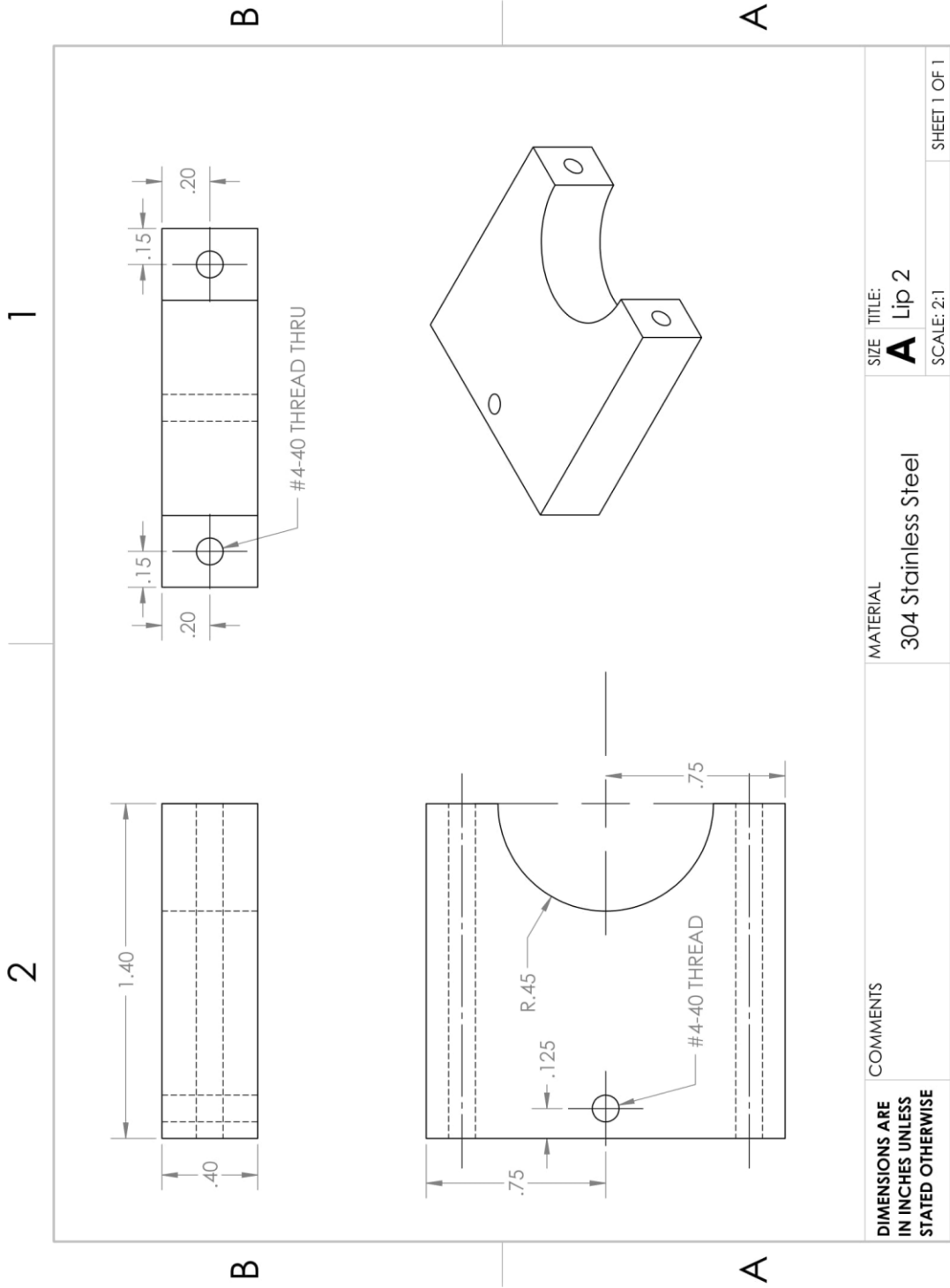




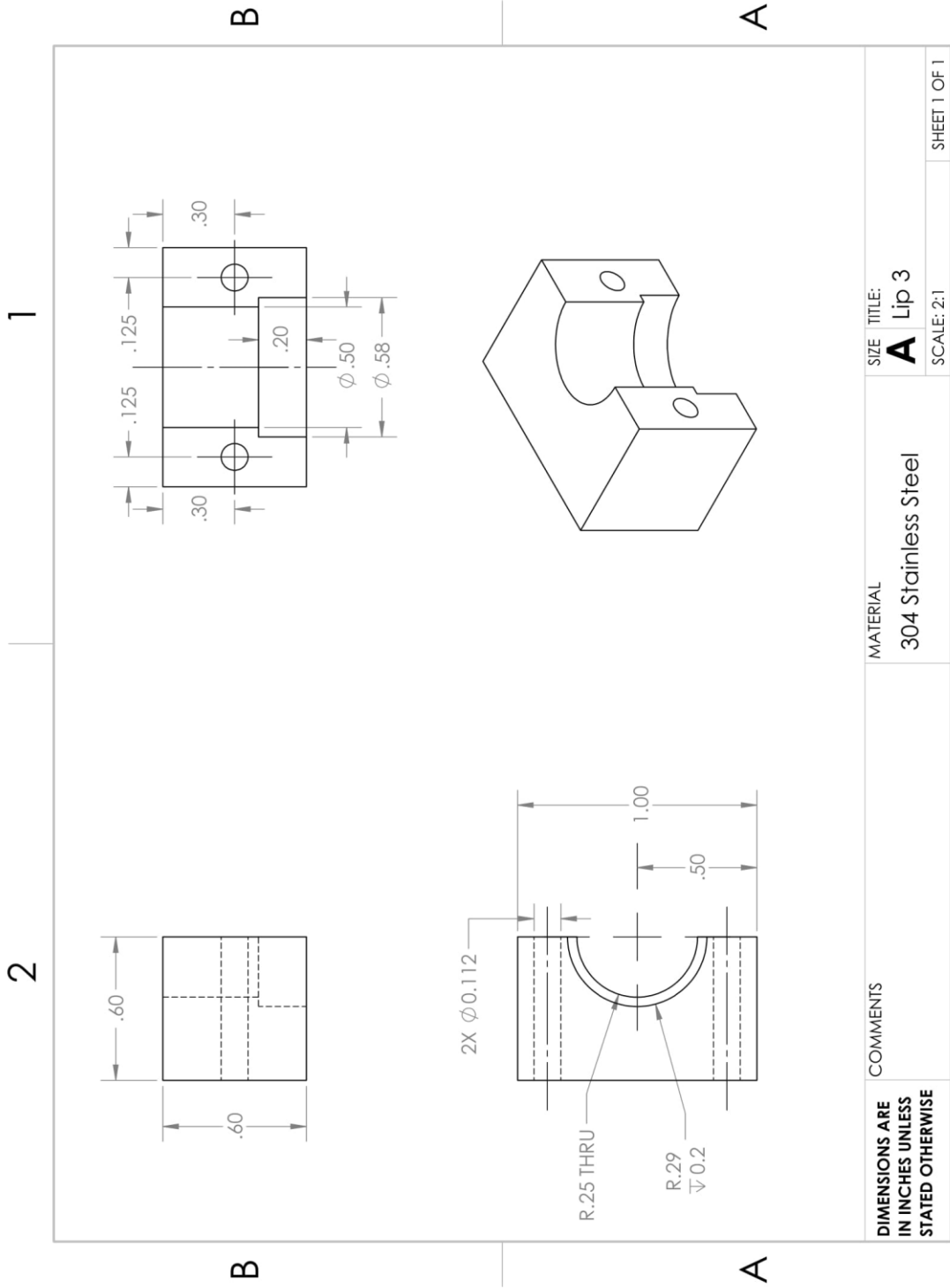


DIMENSIONS ARE IN INCHES UNLESS STATED OTHERWISE	COMMENTS	MATERIAL	SIZE	TITLE:
		304 Stainless Steel	A	Lip 1
		SCALE: 2:1	SHEET 1 OF 1	

SOLIDWORKS Educational Product. For Instructional Use Only.



SOLIDWORKS Educational Product. For Instructional Use Only.

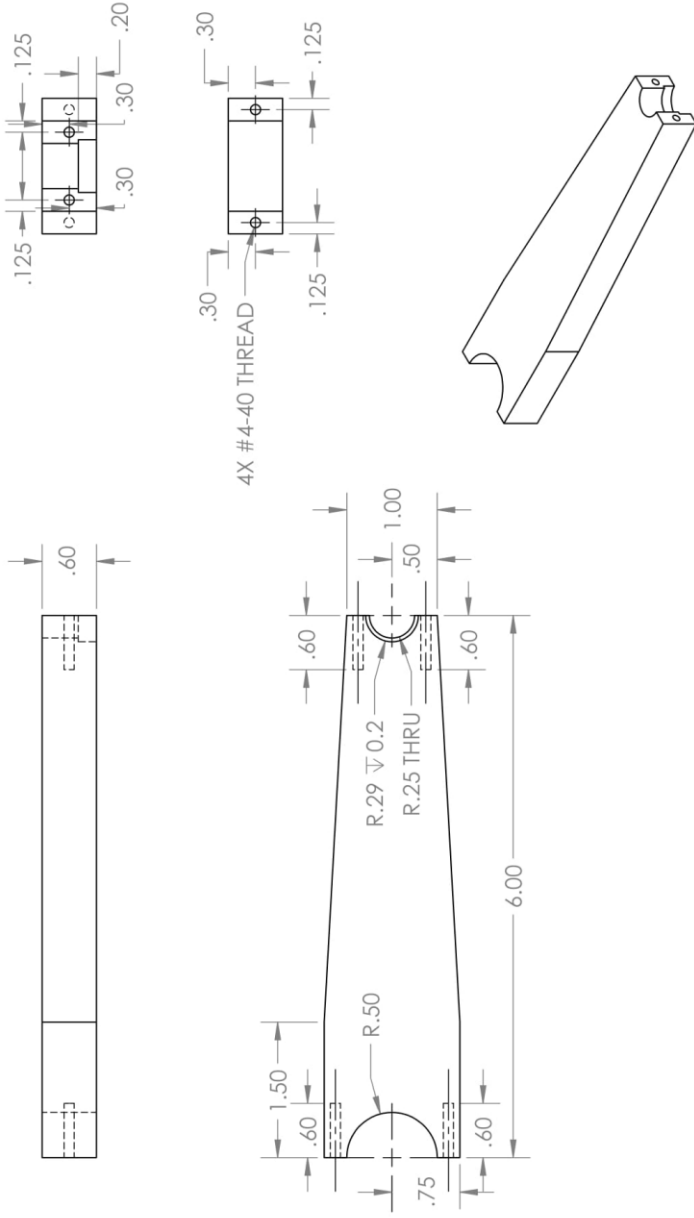


DIMENSIONS ARE IN INCHES UNLESS STATED OTHERWISE	COMMENTS	MATERIAL	SIZE TITLE: A Lip 3 SCALE: 2:1
		304 Stainless Steel	SHEET 1 OF 1

SOLIDWORKS Educational Product. For Instructional Use Only.

2

1



DIMENSIONS ARE IN INCHES UNLESS STATED OTHERWISE

COMMENTS

MATERIAL
304 Stainless Steel

SIZE TITLE:
A Lip 4

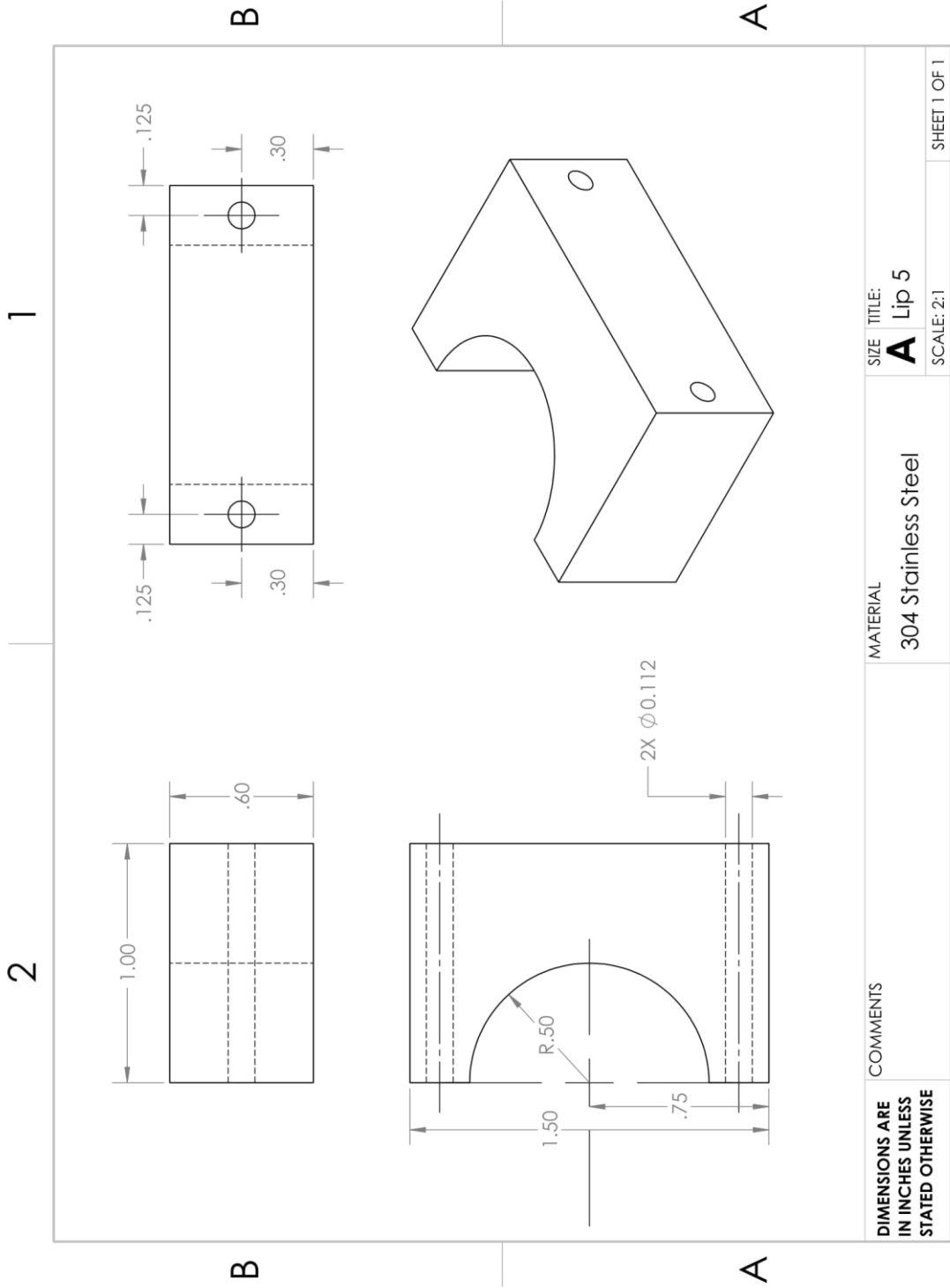
SCALE: 1:2

SHEET 1 OF 1

SOLIDWORKS Educational Product. For Instructional Use Only.

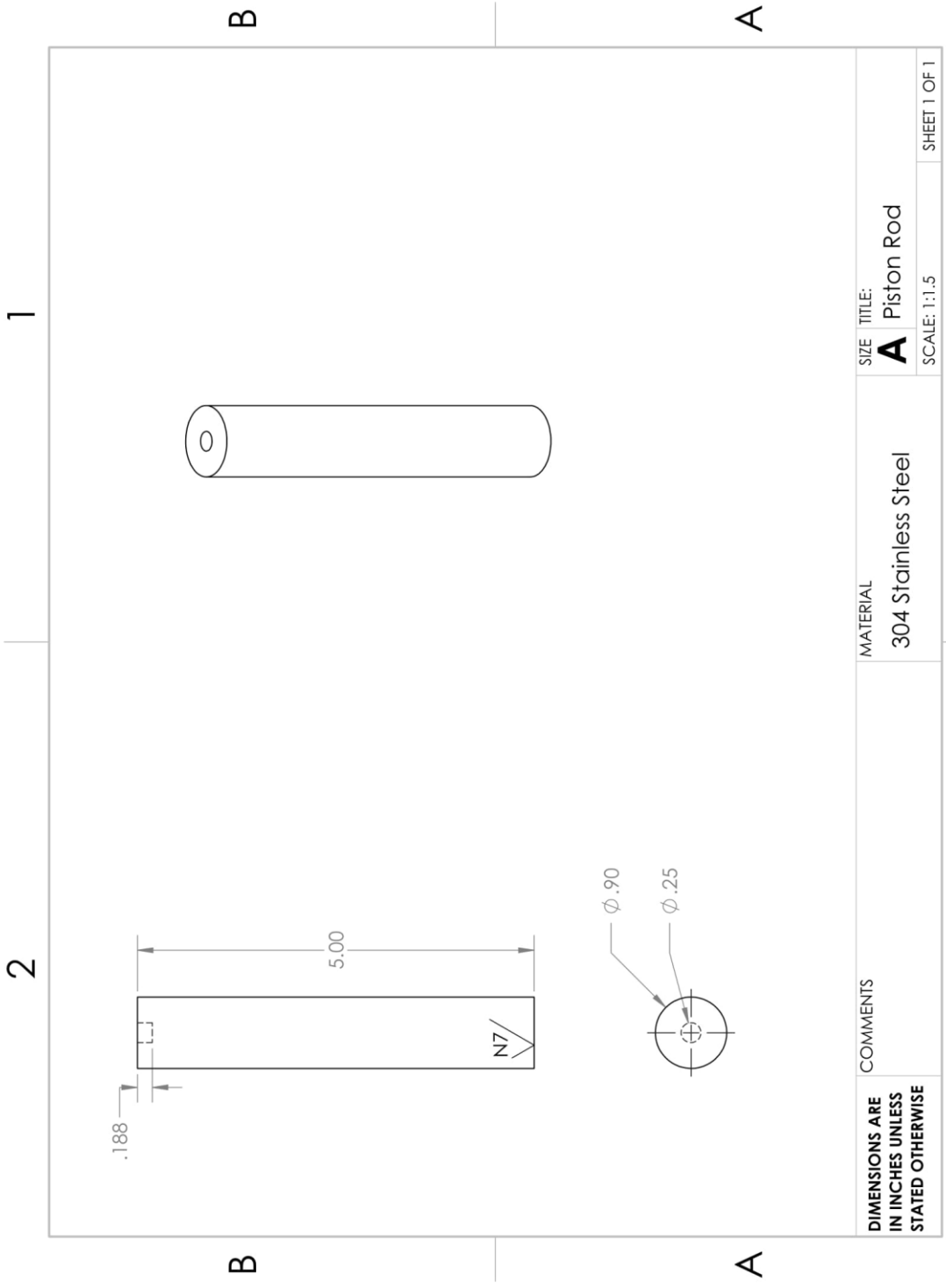
2

1



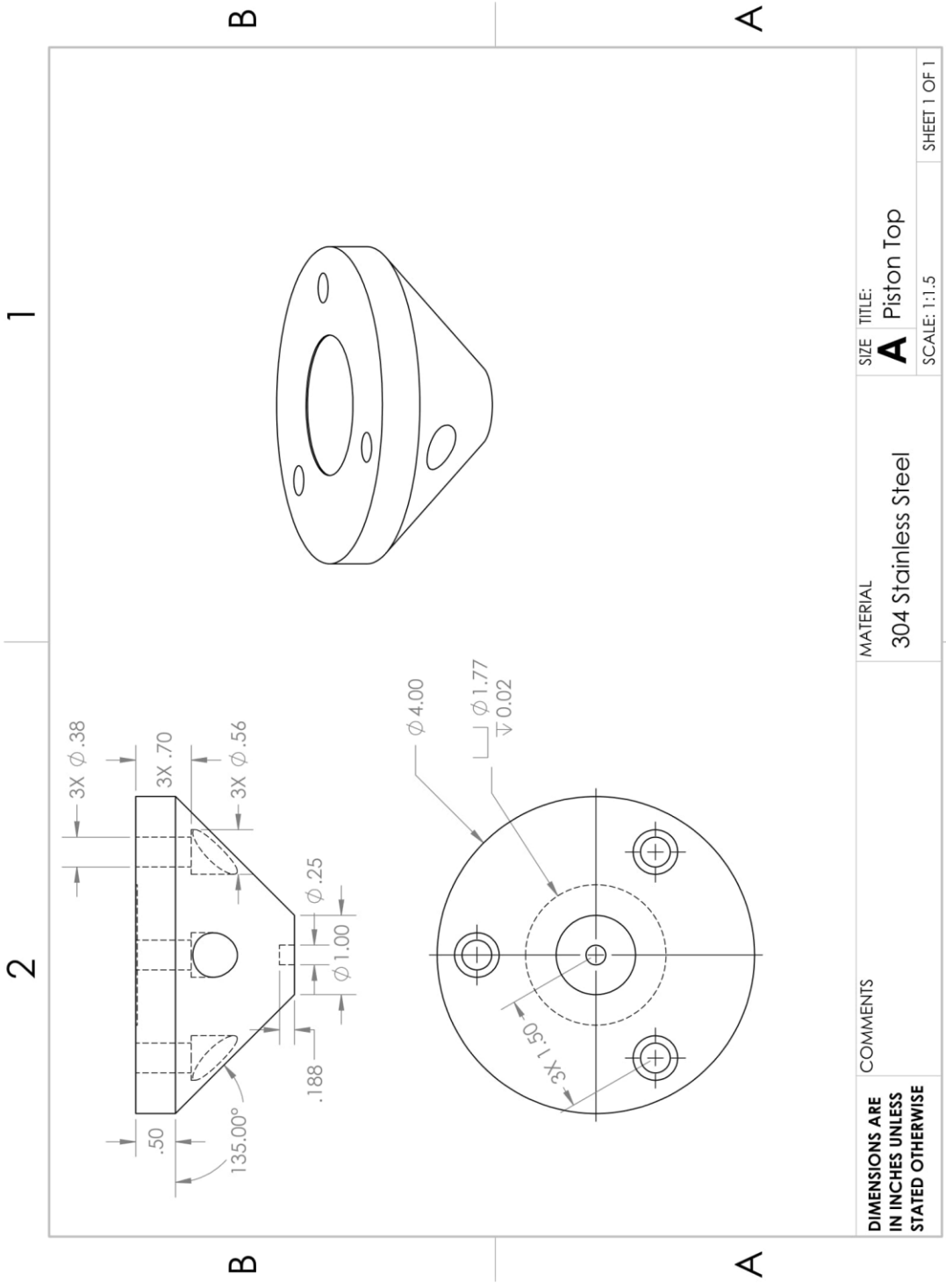
DIMENSIONS ARE IN INCHES UNLESS STATED OTHERWISE	COMMENTS	MATERIAL	SIZE	TITLE:	SHEET 1 OF 1
			304 Stainless Steel	A Lip 5	
			SCALE: 2:1		

SOLIDWORKS Educational Product. For Instructional Use Only.



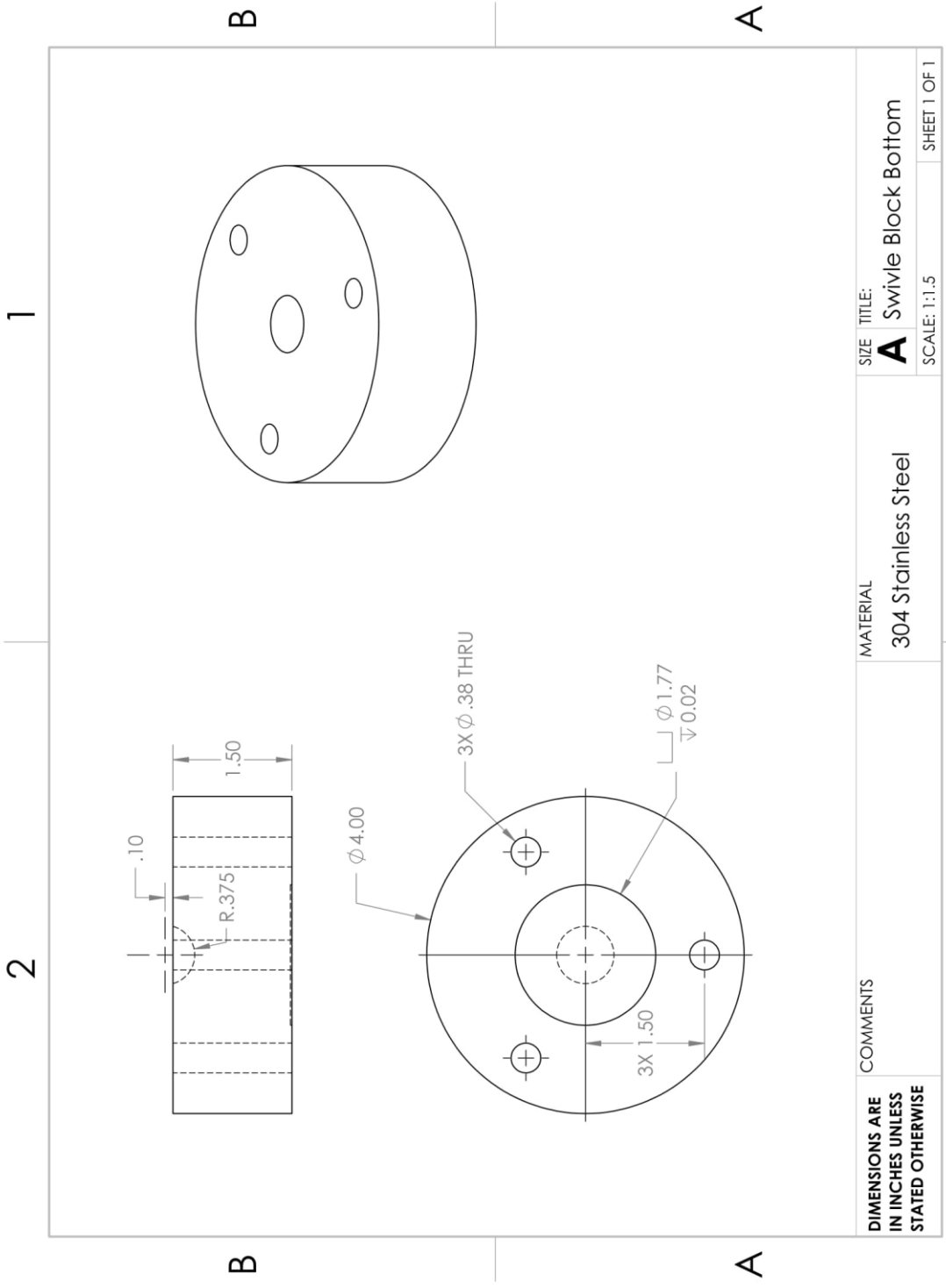
DIMENSIONS ARE IN INCHES UNLESS STATED OTHERWISE	COMMENTS	MATERIAL	SIZE	TITLE:	SHEET 1 OF 1
			304 Stainless Steel	A Piston Rod	
			SCALE: 1:1.5		

SOLIDWORKS Educational Product. For Instructional Use Only.



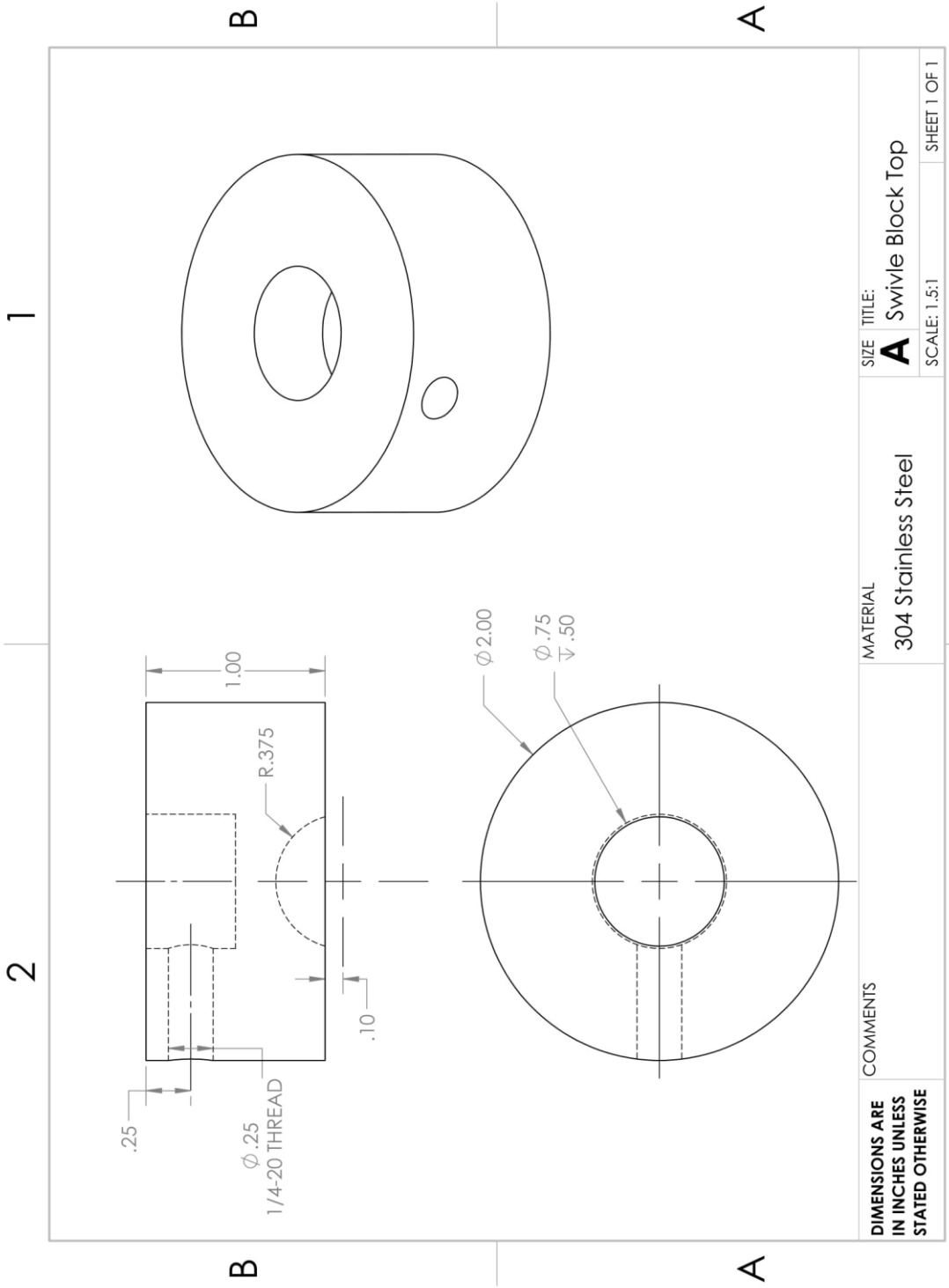
DIMENSIONS ARE IN INCHES UNLESS STATED OTHERWISE	COMMENTS	MATERIAL	SIZE	TITLE:	SHEET 1 OF 1
			304 Stainless Steel	A Piston Top	
			SCALE: 1:1.5		

SOLIDWORKS Educational Product. For Instructional Use Only.



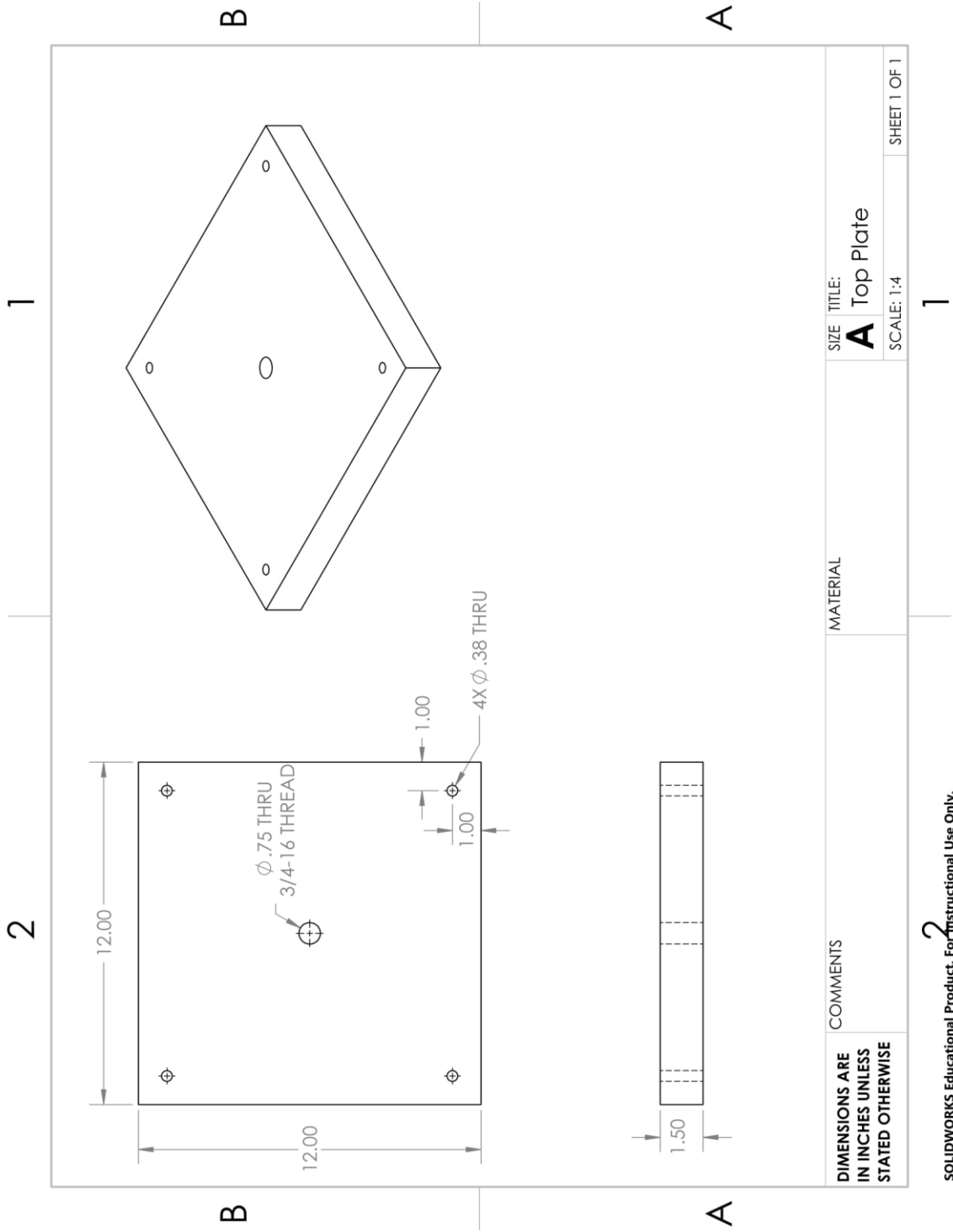
DIMENSIONS ARE IN INCHES UNLESS STATED OTHERWISE	COMMENTS	MATERIAL	SIZE	TITLE:
			304 Stainless Steel	A Swivle Block Bottom
			SCALE: 1:1.5	SHEET 1 OF 1

SOLIDWORKS Educational Product. For Instructional Use Only. 2 1



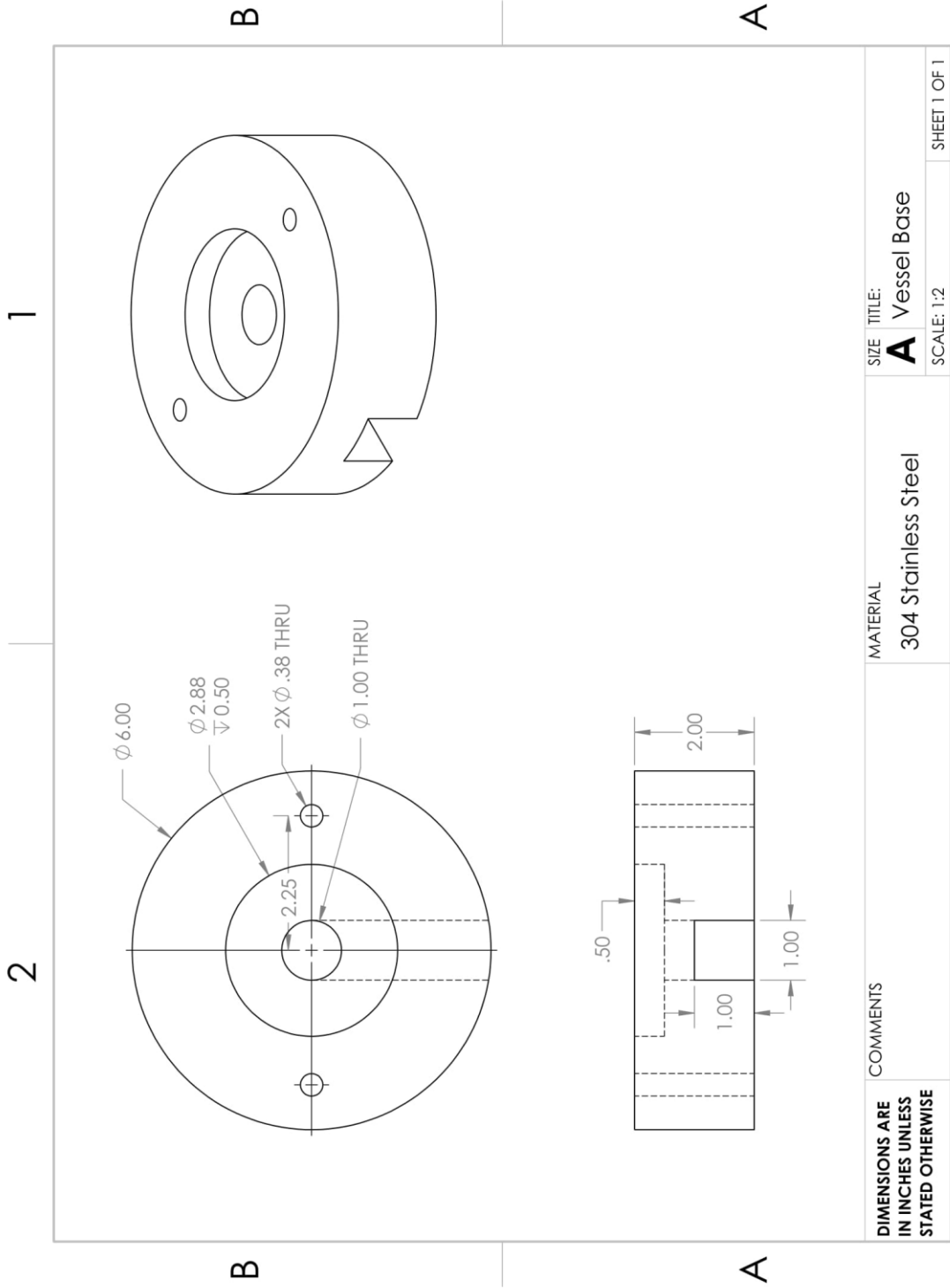
DIMENSIONS ARE IN INCHES UNLESS STATED OTHERWISE	COMMENTS	MATERIAL	SIZE	TITLE:
			304 Stainless Steel	A Swivle Block Top
			SCALE: 1.5:1	SHEET 1 OF 1

SOLIDWORKS Educational Product. For Instructional Use Only.



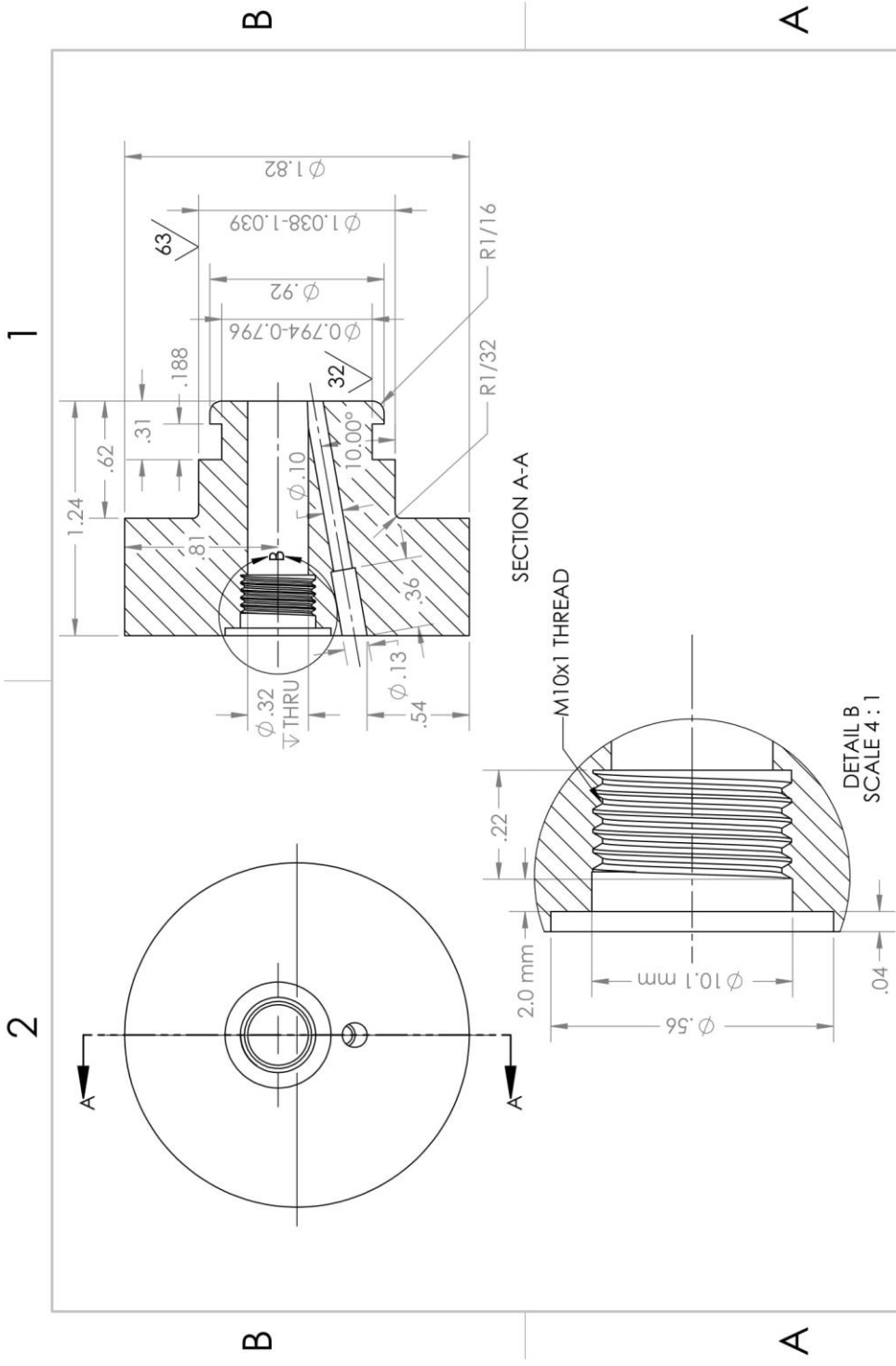
DIMENSIONS ARE IN INCHES UNLESS STATED OTHERWISE	COMMENTS	MATERIAL	SIZE	TITLE:
			A	Top Plate
			SCALE: 1:4	SHEET 1 OF 1

SOLIDWORKS Educational Product. For Instructional Use Only.



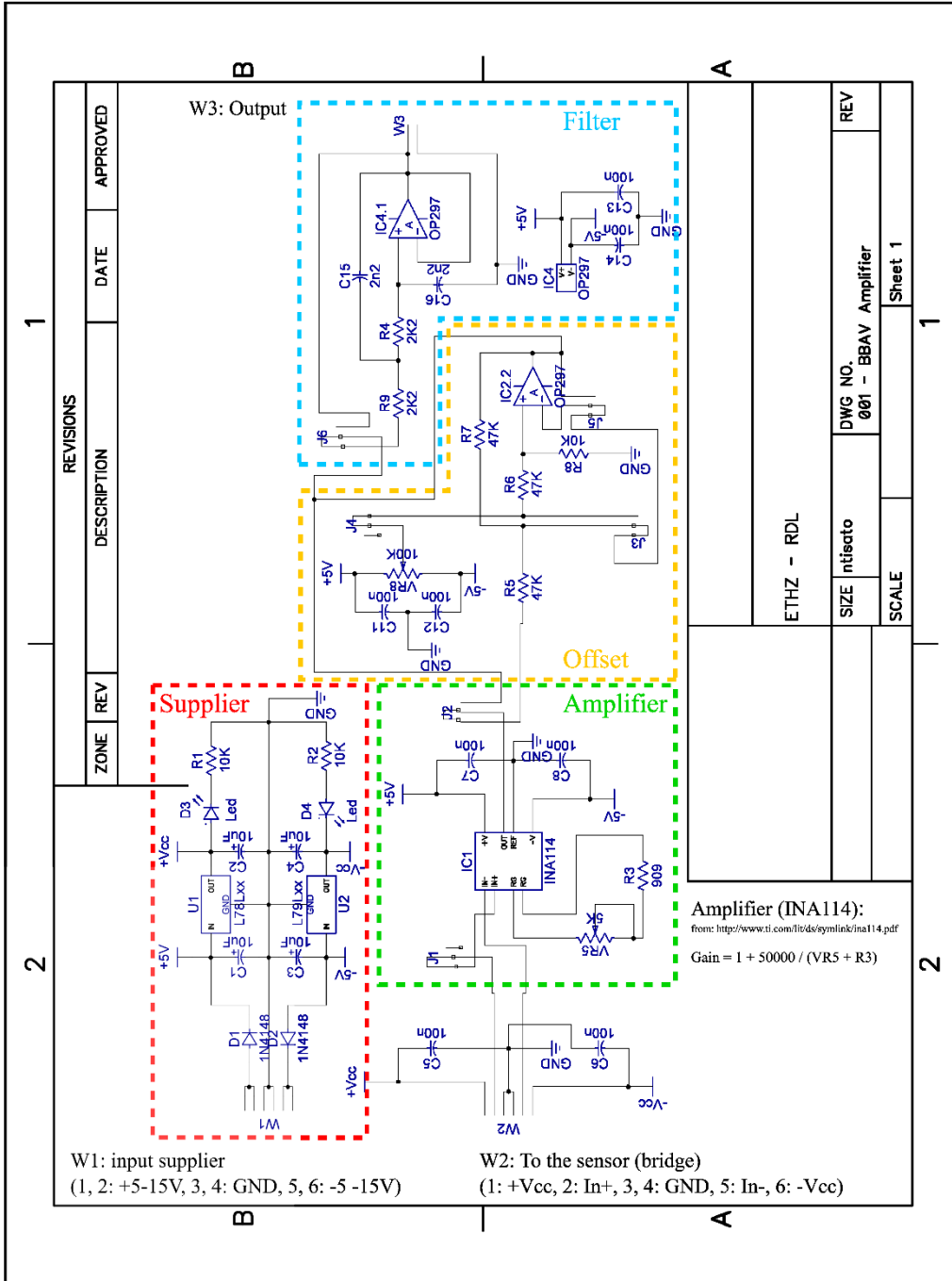
DIMENSIONS ARE IN INCHES UNLESS STATED OTHERWISE	COMMENTS	MATERIAL	SIZE	TITLE:	SHEET 1 OF 1
		304 Stainless Steel	A	Vessel Base	
			SCALE: 1:2		

SOLIDWORKS Educational Product. For Instructional Use Only.



DIMENSIONS ARE IN INCHES UNLESS STATED OTHERWISE	COMMENTS	MATERIAL	SIZE	TITLE:
		304 Stainless Steel	A	Vessel Cover
			SCALE: 1.5:1	SHEET 1 OF 1

SOLIDWORKS Educational Product. For Instructional Use Only.



References

- Barton, N. (2007). Rock quality, seismic velocity, attenuation and anisotropy. CRC press.
- Batzle, M. L., Han, D. H., & Hofmann, R. (2006). Fluid mobility and frequency-dependent seismic velocity—Direct measurements. *Geophysics*, 71(1), N1-N9.
- Batzle, M., & Wang, Z. (1992). Seismic properties of pore fluids. *Geophysics*, 57(11), 1396-1408.
- Behroozi, F., Smith, J., & Even, W. (2010). Stokes' dream: Measurement of fluid viscosity from the attenuation of capillary waves. *American Journal of Physics*, 78(11), 1165-1169.
- Biot, M. A. (1956a). Theory of propagation of elastic waves in a fluid-saturated porous solid. I. Low-frequency range. *The Journal of the acoustical Society of america*, 28(2), 168-178.
- Biot, M. A. (1956b). Theory of propagation of elastic waves in a fluid-saturated porous solid. II. Higher frequency range. *The Journal of the acoustical Society of america*, 28(2), 179-191.
- Birch, F., & Bancroft, D. (1938). Elasticity and internal friction in a long column of granite. *Bulletin of the Seismological Society of America*, 28(4), 243-254.
- Born, W. T. (1941). The attenuation constant of earth materials. *Geophysics*, 6(2), 132-148.
- Bradley, J. J., & Fort, A. N. (1966). SECTION 8: INTERNAL FRICTION IN ROCKS. *Geological Society of America Memoirs*, 97, 175-200.
- Bruckshaw, J. M., & Mahanta, P. C. (1961). The variation of the elastic constants of rocks with frequency. *Geophysical Prospecting*, 9, 65-76.
- Chapman, M., Liu, E., & Li, X. Y. (2006). The influence of fluid sensitive dispersion and attenuation on AVO analysis. *Geophysical Journal International*, 167(1), 89-105.
- Clark, V. A., Tittmann, B. R., & Spencer, T. W. (1980). Effect of volatiles on attenuation (Q^{-1}) and velocity in sedimentary rocks. *Journal of Geophysical Research: Solid Earth*, 85(B10), 5190-5198.
- Collier, L., Neuberg, J. W., Lensky, N., Lyakhovsky, V., & Navon, O. (2006). Attenuation in gas-charged magma. *Journal of volcanology and geothermal research*, 153(1-2), 21-36.
- Cooper, R. F. (2002). Seismic wave attenuation: Energy dissipation in viscoelastic crystalline solids. *Reviews in Mineralogy and Geochemistry*, 51(1), 253-290.
- Day, M. A. (1990). The no-slip condition of fluid dynamics. *Erkenntnis*, 33(3), 285-296.
- Doi, M., & Edwards, S. F. (1988). *The theory of polymer dynamics* (Vol. 73). oxford university press.

- Dukhin, A. S., & Goetz, P. J. (2009). Bulk viscosity and compressibility measurement using acoustic spectroscopy. *The Journal of chemical physics*, 130(12), 124519.
- Dunham, E. M., Harris, J. M., Zhang, J., Quan, Y., & Mace, K. (2017). Hydraulic fracture conductivity inferred from tube wave reflections. In SEG Technical Program Expanded Abstracts 2017 (pp. 947-952). Society of Exploration Geophysicists.
- Dvorkin, J., & Nur, A. (1993). Dynamic poroelasticity: A unified model with the squirt and the Biot mechanisms. *Geophysics*, 58(4), 524-533.
- Dymond, J. H., Isdale, J. D., & Glen, N. F. (1985). Density measurement at high pressure. *Fluid Phase Equilibria*, 20, 305-314.
- Eggers, F., & Kaatze, U. (1996). Broad-band ultrasonic measurement techniques for liquids. *Measurement Science and Technology*, 7(1), 1.
- Fisher, F. H., & Simmons, V. P. (1977). Sound absorption in sea water. *The Journal of the Acoustical Society of America*, 62(3), 558-564.
- Fridleifsson, I. B., Bertani, R., Huenges, E., Lund, J. W., Ragnarsson, A., & Rybach, L. (2008). The possible role and contribution of geothermal energy to the mitigation of climate change. In *IPCC scoping meeting on renewable energy sources, proceedings, Luebeck, Germany* (Vol. 20, No. 25, pp. 59-80). Citeseer.
- Gardner, G. H. F., Wyllie, M. R. J., & Droschak, D. (1964). Effects of pressure and fluid saturation on the attenuation of elastic waves in sands. *Journal of Petroleum Technology*, 16(02), 189-198.
- Gholizadeh, H., Burton, R., & Schoenau, G. (2011). Fluid bulk modulus: a literature survey. *International Journal of Fluid Power*, 12(3), 5-15.
- Gordon, R. B., & Davis, L. A. (1968). Velocity and attenuation of seismic waves in imperfectly elastic rock. *Journal of Geophysical Research*, 73(12), 3917-3935.
- Hamilton, E. L. (1972). Compressional-wave attenuation in marine sediments. *Geophysics*, 37(4), 620-646.
- Holocher, J., Peeters, F., Aeschbach-Hertig, W., Kinzelbach, W., & Kipfer, R. (2003). Kinetic model of gas bubble dissolution in groundwater and its implications for the dissolved gas composition. *Environmental Science & Technology*, 37(7), 1337-1343.
- Incropera, F. P., Lavine, A. S., Bergman, T. L., & DeWitt, D. P. (2007). *Fundamentals of heat and mass transfer*. Wiley.
- Johnston, D. H. (1981). Attenuation: a state-of-the-art summary. In *Seismic wave attenuation* (Vol. 2, pp. 123-139). Geophysical Reprint Series, Society of Exploration Geophysicists, Tulsa, OK.

- Johnston, D. H., Toksöz, M. N., & Timur, A. (1979). Attenuation of seismic waves in dry and saturated rocks: II. Mechanisms. *Geophysics*, 44(4), 691-711.
- Jones, T., & Nur, A. (1983). Velocity and attenuation in sandstone at elevated temperatures and pressures. *Geophysical Research Letters*, 10(2), 140-143.
- Karato, S. I., & Spetzler, H. A. (1990). Defect microdynamics in minerals and solid-state mechanisms of seismic wave attenuation and velocity dispersion in the mantle. *Reviews of Geophysics*, 28(4), 399-421.
- Kays, W. M., & Crawford, M. E. (1993). *Convective heat and mass transfert* (No. BOOK). McGraw-Hill.
- Kearey, P., Brooks, M., & Hill, I. (2013). *An introduction to geophysical exploration*. John Wiley & Sons.
- Kestin, J., Sokolov, M., & Wakeham, W. A. (1978). Viscosity of liquid water in the range– 8 C to 150 C. *Journal of Physical and Chemical Reference Data*, 7(3), 941-948.
- Klimentos, T. (1991). Geometric corrections in attenuation measurements. *Geophysical Prospecting*, 39(2), 193-218.
- Knopoff, L. (1964) “Q” Department of Physics and Institute of Geophysics and Planetary Physics University of California, Los Angeles. *Rev Geophys*, 2(4), 625-660.
- Landau, L. D., & Lifshitz, E. M. (1959). *Fluid Mechanics* Pergamon. *New York*, 61.
- Lakes, R. (2009). *Viscoelastic materials*. Cambridge University Press.
- Leibler, L., Rubinstein, M., & Colby, R. H. (1991). Dynamics of reversible networks. *Macromolecules*, 24(16), 4701-4707.
- Liebermann, L. N. (1948). The origin of sound absorption in water and in sea water. *The Journal of the Acoustical Society of America*, 20(6), 868-873.
- Litovitz, T. A., & Carnevale, E. H. (1955). Effect of pressure on sound propagation in water. *Journal of Applied Physics*, 26(7), 816-820.
- Madonna, C., & Tisato, N. (2013). A new seismic wave attenuation module to experimentally measure low-frequency attenuation in extensional mode. *Geophysical Prospecting*, 61(2), 302-314.
- Mason, W.P., Beshers, D.N., & Kuo, J.T., (1970). Internal friction in Westerly granite: Relation to dislocation theory: *Journal of Applied Physics*, 41(13), 5206-5209.
- Mavko, G., & Nur, A. (1975). Melt squirt in the asthenosphere. *Journal of Geophysical Research*, 80(11), 1444-1448.
- Mavko, G., Mukerji, T., & Dvorkin, J. (2009). *The rock physics handbook: Tools for seismic analysis of porous media*. Cambridge university press.

- McCleary, B. V., Clark, A. H., Dea, I. C., & Rees, D. A. (1985). The fine structures of carob and guar galactomannans. *Carbohydrate Research*, 139, 237-260.
- Mudgil, D., Barak, S., & Khatkar, B. S. (2014). Guar gum: processing, properties and food applications—a review. *Journal of food science and technology*, 51(3), 409-418.
- Murphy III, W. F. (1982). Effects of partial water saturation on attenuation in Massilon sandstone and Vycor porous glass. *The Journal of the Acoustical Society of America*, 71(6), 1458-1468.
- Murphy III, W. F., Winkler, K. W., & Kleinberg, R. L. (1986). Acoustic relaxation in sedimentary rocks: Dependence on grain contacts and fluid saturation. *Geophysics*, 51(3), 757-766.
- O'Connell, R. J., & Budiansky, B. (1977). Viscoelastic properties of fluid-saturated cracked solids. *Journal of Geophysical Research*, 82(36), 5719-5735.
- O'Connell, R. J., & Budiansky, B. (1978). Measures of dissipation in viscoelastic media. *Geophysical Research Letters*, 5(1), 5-8.
- Orban, F. (2011). Damping of materials and members in structures. In *Journal of Physics: Conference Series* (Vol. 268, No. 1, p. 012022). IOP Publishing.
- Osif, T. L. (1988). The effects of salt, gas, temperature, and pressure on the compressibility of water. *SPE reservoir Engineering*, 3(01), 175-181.
- Pandit, B. I., & Savage, J. C. (1973). An experimental test of Lomnitz's theory of internal friction in rocks. *Journal of Geophysical Research*, 78(26), 6097-6099.
- Peselnick, L., & Zietz, I. (1959). Internal friction of fine-grained limestones at ultrasonic frequencies. *Geophysics*, 24(2), 285-296.
- Pimienta, L., Fortin, J., & Guéguen, Y. (2015). Bulk modulus dispersion and attenuation in sandstones. *Geophysics*, 80(2), D111-D127.
- Pinkerton, J. M. M. (1947). A pulse method for the measurement of ultrasonic absorption in liquids: results for water. *Nature*, 160(4056), 128.
- Read, T. A. (1940). The internal friction of single metal crystals. *Physical Review*, 58(4), 371.
- Reynolds, O. (1883). XXIX. An experimental investigation of the circumstances which determine whether the motion of water shall be direct or sinuous, and of the law of resistance in parallel channels. *Philosophical Transactions of the Royal society of London*, (174), 935-982.
- Robinson, G., Ross-Murphy, S. B., & Morris, E. R. (1982). Viscosity-molecular weight relationships, intrinsic chain flexibility, and dynamic solution properties of guar galactomannan. *Carbohydrate Research*, 107(1), 17-32.

- Savage, J. C. (1969). Comments on paper by RB Gordon and LA Davis, 'Velocity and attenuation of seismic waves in imperfectly elastic rock'. *Journal of Geophysical Research*, 74(2), 726-728.
- Schlichting, H., & Gersten, K. (2016). *Boundary-layer theory*. Springer.
- Seeton, C. J. (2006). Viscosity-temperature correlation for liquids. In STLE/ASME 2006 International Joint Tribology Conference (pp. 131-142). American Society of Mechanical Engineers.
- Semenov, A. N., & Rubinstein, M. (1998). Thermoreversible gelation in solutions of associative polymers. 1. Statics. *Macromolecules*, 31(4), 1373-1385.
- Sheehy, M. J., & Halley, R. (1957). Measurement of the attenuation of low-frequency underwater sound. *The Journal of the Acoustical Society of America*, 29(4), 464-469.
- Slie, W. M., Donfor Jr, A. R., & Litovitz, T. A. (1966). Ultrasonic shear and longitudinal measurements in aqueous glycerol. *The Journal of Chemical Physics*, 44(10), 3712-3718.
- Smith Jr, L. H., Peeler, R. L., & Bernd, L. H. (1960). *Hydraulic Fluid Bulk Modulus—Its Effect on System Performance and Techniques for Physical Measurement*. NFPA Publication.(19 p.).
- Stokes, S. G. G. (1901). *Mathematical and physical papers*.
- Strohm, E. M., & Kolios, M. C. (2011). Sound velocity and attenuation measurements of perfluorocarbon liquids using photoacoustic methods. In *2011 IEEE International Ultrasonics Symposium* (pp. 2368-2371). IEEE.
- Subramaniyan, S., Quintal, B., Tisato, N., Saenger, E. H., & Madonna, C. (2014). An overview of laboratory apparatuses to measure seismic attenuation in reservoir rocks. *Geophysical Prospecting*, 62(6), 1211-1223.
- Thorp, W. H. (1965). Deep-ocean sound attenuation in the sub-and low-kilocycle-per-second region. *The Journal of the Acoustical Society of America*, 38(4), 648-654.
- Tisato, N., & Madonna, C. (2012). Attenuation at low seismic frequencies in partially saturated rocks: Measurements and description of a new apparatus. *Journal of Applied Geophysics*, 86, 44-53.
- Tisato, N., & Quintal, B. (2013). Measurements of seismic attenuation and transient fluid pressure in partially saturated Berea sandstone: evidence of fluid flow on the mesoscopic scale. *Geophysical Journal International*, 195(1), 342-351.
- Tisato, N., & Quintal, B. (2014). Laboratory measurements of seismic attenuation in sandstone: Strain versus fluid saturation effects. *Geophysics*, 79(5), WB9-WB14.

- Tisato, N., Quintal, B., Chapman, S., Podladchikov, Y., & Burg, J. P. (2015). Bubbles attenuate elastic waves at seismic frequencies: First experimental evidence. *Geophysical Research Letters*, 42(10), 3880-3887.
- Toksöz, M. N., Johnston, D. H., & Timur, A. (1979). Attenuation of seismic waves in dry and saturated rocks: I. Laboratory measurements. *Geophysics*, 44(4), 681-690.
- Toksoz, M. N., & Johnston, D. H. (1981). Seismic wave attenuation: Society of Exploration Geophysicists. Geophysics reprint series, (2).
- Tutuncu, A. N., Podio, A. L., Gregory, A. R., & Sharma, M. M. (1998). Nonlinear viscoelastic behavior of sedimentary rocks, Part I: Effect of frequency and strain amplitude. *Geophysics*, 63(1), 184-194.
- Walsh, J. B. (1966). Seismic wave attenuation in rock due to friction. *Journal of Geophysical Research*, 71(10), 2591-2599.
- Ward-Smith, J. (2012). *Mechanics of fluids*. CRC Press.
- Wientjes, R. H., Duits, M. H., Jongschaap, R. J., & Mellema, J. (2000). Linear rheology of guar gum solutions. *Macromolecules*, 33(26), 9594-9605.
- Winkler, K. W., & Nur, A. (1982). Seismic attenuation: Effects of pore fluids and frictional-sliding. *Geophysics*, 47(1), 1-15.
- Winkler, K., Nur, A., & Gladwin, M. (1979). Friction and seismic attenuation in rocks. *Nature*, 277(5697), 528.
- Wyllie, M. R. J., Gardner, G. H. F., & Gregory, A. R. (1962). Studies of elastic wave attenuation in porous media. *Geophysics*, 27(5), 569-589.
- Yunus, A. C., & Cimbala, J. M. (2006). Fluid mechanics fundamentals and applications. International Edition, McGraw Hill Publication, 185201.
- Yin, C. S., Batzle, M. L., & Smith, B. J. (1992). Effects of partial liquid/gas saturation on extensional wave attenuation in Berea sandstone. *Geophysical Research Letters*, 19(13), 1399-1402.
- Zener, C. (1938). Internal friction in solids II. General theory of thermoelastic internal friction. *Physical Review*, 53(1), 90.
- Zener, C. (1940). Internal friction in solids. *Proceedings of the Physical Society*, 52(1), 152.